UNIVERSITY OF OKLAHOMA

GRADUATE COLLEGE

CHARACTERIZATION AND DEVELOPMENT OF SEMICONDUCTOR CASCADE DEVICES

A DISSERTATION

SUBMITTED TO THE GRADUATE FACULTY

in partial fulfillment of the requirements for the

Degree of

DOCTOR OF PHILOSOPHY

By

SM SHAZZAD S RASSEL
Norman, Oklahoma
2018

CHARACTERIZATION AND DEVELOPMENT OF SEMICONDUCTOR CASCADE DEVICES

A DISSERTATION APPROVED FOR THE
SCHOOL OF ELECTRICAL AND COMPUTER ENGINEERING

BY

_____
Dr. Rui Q. Yang, Chair

_____
Dr. Matthew B. Johnson, Co-Chair

_____
Dr. Michael B. Santos

_____
Dr. Hjalti Sigmarsson

_____
Dr. Caleb Fulton

To
my late father, who is always inside me as my inspiration;
my mother who is counting days to see my face;
my father-in-law who will be the proudest person to see me as a graduate;
my mother-in-law who prays always for my success;
my beloved wife without whom I couldn't face all my difficulties, and
my sweetest daughter who asks me always "when will you graduate?"

Acknowledgements

I want to express my deepest gratitude to my Advisor *Dr. Rui. Q. Yang* for giving me the opportunity to work in his research group. I have learnt a lot about the complicated device-physics and quantum-mechanics by attending several of his theory and TA classes. He encouraged me always to ask questions in his classes, group meetings, and informal discussions to stimulate my research journey. He is very thorough and consistent in his work-ethics and principles, which always encouraged me to rethink and reevaluate my works before finalizing any document, enhancing my ability to work with details. He always helped me to nurture my theoretical knowledge about our research area by giving me all possible access to his resources. I will always appreciate all his critical feed-backs, patience, and motivation that he invested in my dissertation. I also sincerely express my gratitude to *Dr. Matthew B. Johnson* as my Co-advisor to give me the opportunity to work with him in the early stage of my Ph.D. program before leaving for *West Virginia University*. He invested his valuable time and energy in me that accelerated my knowledge in various areas, especially in the field of experimentation and instrumentation. The valuable discussions on various research topics with him will always be an inspiration to me. I appreciate that he always offered me help and new ideas from far to enable me to complete this dissertation successfully.

I am grateful to my committee members *Dr. Mike Santos, Dr. Hjalti Sigmarsson,* and *Dr. Caleb Fulton* for contributing in my dissertation committee and giving me feedback on my general exam and dissertation.

During my Ph.D. studies, I had the privilege to work closely with current and former students from this Quantum Device Laboratory group at OU. Many thanks go to

Dr. Hossein Lotfi to work with me closely in several projects at OU and for the hours of phone discussion from his work place at California to discuss various issues related to my research work. His depth of knowledge and caring mind inspired me to be his good friend beyond academia and I value him as an inspiration. Many thanks go to *Dr. Li Lu* for processing a lot of devices used in this dissertation and for teaching me processing and characterization. I want to thank our current group members *Mr. Jeremy Massengale*, *Mr. Wenxiang*, and *Mr. Yiyun* for their valuable discussions on various research topics and helpful comments on few of my chapters. I also want to thank our former group members *Dr. Robert T. Hinkey*, *Dr. Hao Ye* and *Dr. Lin Lei* for their valuable research contributions that were altogether a great inspiration to me. I also want to give special thanks to *Dr. Preston R. Larson* to teach me how to perform SEM imaging and FIB milling.

I want to thank the *National Research Council, Canada* for the MBE growth of some of the laser samples which became a major part of my dissertation and AFOSR *(Award Number: FA9550-15-1-0067)* and NSF *(IIP-1640576)* for supporting my research work. Some of the structures in this dissertation were grown in the GENxplor MBE system at OU, which was acquired with support from the NSF through Grant No. DMR-1229678.

Finally, I would like to express my deepest gratitude to my beloved wife, *Sadia Afrin*, to struggle with me as a friend in my difficult situations; my daughter, *Safa*, to excuse me for not having enough play-time with her; *my mother*, to give me mental support; my late *father* to be always with me as my inner strength; my *father-in-law* for his great guardianship and my *mother-in-law* for her prayers.

Table of Contents

List of Tables

List of Figures

Abstract

Interband cascade lasers (ICLs) are efficient source of mid-infrared light for many applications that require low power consumption and continuous wave (cw) operation at room temperature. In the last decade, remarkable progress has been made in developing ICLs on GaSb substrates, mainly in the 3 to 4μm wavelength region, but room temperature (RT) cw operation at the longer wavelength region beyond 6μm has not been achieved. Based on the characterization of earlier grown ICLs, InAs-based plasmon-waveguide ICLs were designed and fabricated to achieve improved performance near or beyond 6μm. These lasers were extensively characterized, investigated and analyzed in terms of various performance features and compared to other state-of-the-art lasers. One laser demonstrated a threshold current density (J_{th}) as low as 333A/cm^2 at 300K for emission at 6003nm. This J_{th} is the lowest ever reported for a mid-infrared semiconductor laser in this wavelength range. These ICLs lased at temperatures up to 293K in cw mode and up to 357K in pulsed mode. A narrow-ridge laser operated in cw at 293K with a threshold input power as low as 0.66W, and was able to generate 3mW/facet output power at 280K, without accounting for beam divergence loss. These results are very encouraging examples of efficient ICLs at long wavelengths with low power consumption.

To investigate the quality of the laser beam of these InAs-based ICLs, the far-field patterns were studied and analyzed for both broad-area and narrow-ridge geometries. In the growth direction, near diffraction-limited single-mode beams were obtained. As expected, multi-mode lasing was observed in the lateral direction because the stripe widths were much longer than the lasing wavelength. Also, as expected, these

multi-modes were found to be dependent on applied bias current. These far-field profiles were compared to simulations and reasonable agreement was obtained. Beam propagation factors were plotted against the laser stripe sizes and the values were found close to unity along the growth direction -indicating better beam quality, and below 18 along lateral direction -indicating room for improvement. This methodology can be applied to previously fabricated ICLs to better understand their beam optics.

In a related research project, single mode operation of ICLs was obtained by designing and fabricating a cleaved-coupled-cavity (CCC) laser. In our case, rather than cleaving to fabricate two cavities, we successfully demonstrated two ion-milling recipes, using a focused ion beam (FIB) to fabricate our CCC lasers. One recipe separated the two sections of CCC lasers electrically and the other recipe milled a narrow slot (*air-gap*) into the mesa. Based on the optical power from the fabricated cavities, the quality of the milled facet was found to be comparable to that of an as-cleaved facet. This CCC laser demonstrated a single mode operation at ~3109nm at room temperature with a reasonable side-mode-suppression-ratio (SMSR) of 24dB. A continuous tuning range of ~1.1nm and quasi-continuous tuning range of 10.3nm was obtained, which are substantially smaller than that for a state-of-the-art distributed feedback or Bragg reflector type laser; however, this result is encouraging considering its simple operation and low power consumption.

Additionally, the applications of the interband cascade devices were extended to high-speed operation. A multi-stage interband cascade infrared photodetector (ICIP) of 20μm×20μm size demonstrated a 1.3GHz operational bandwidth at RT, which is much higher than that for a single stage ICIP. This result clearly shows the advantage of using

the cascade architecture in ICIPs. Some important parameters, such as device capacitance, were extracted by fitting the experimental data. The bonding pad capacitance was identified as one of the major limiting factors towards obtaining high-speed operation. The bandwidths of different ICIPs were found dependent on their sizes, which showed that their performance was limited by external circuit parasitic, and not by their intrinsic carrier transit time. This indicates the possibility of further improvement. The quality of high-speed data transmission was investigated by establishing a one-meter free-space optical (FSO) link. Clear and open eye-diagrams along with a strong signal level were observed for multi-stage ICPs up to 50Mb/s (limit of the instrumentation), which indicates better transmission quality with the possibility to increase the link without need for a signal amplifier.

In the final research project, carrier transport mechanisms were investigated in interband (IB) and intersubband (ISB) based optoelectronic devices by estimating the reverse saturation current density (J_0) from corresponding current-voltage (I-V) plots and by developing a semi-empirical model that was able to relate J_0 to device resistances. Two distinct trend lines were observed; the line corresponding to IB-based devices stayed more than an order of magnitude below that of ISB-based devices when J_0 vs. ΔE (Energy separation) data were plotted for a large wavelength range. This plot has a significant meaning from a device performance perspective; it indicates the intrinsic advantages that interband cascade devices possess over quantum cascade devices in terms of carrier lifetime.

Chapter 1: Introduction

1.1 Infrared light

Infrared (IR) radiation is an electromagnetic radiation with a wavelength that spans from 700nm to 1mm which is very important for many signature applications. This region can be sub-divided into near-infrared (NIR, 0.7 to 1μm), short-wavelength-infrared (SWIR, 1 to 3μm), middle-wavelength-infrared (MWIR, 3 to 5μm), long-wavelength-infrared (LWIR, 5 to 14μm), very-long-wavelength-infrared (VLWIR, 14 to 30μm) and far-infrared (FIR, 30 to 100μm) region [1] as shown in Figure 1-1. All these regions have their own properties and unique signature applications. For example, the SWIR region is widely used for long distance communication especially in fiber optics at ~1.5μm wavelength. Other fields of application are related to agriculture, food-quality control, astronomy, material science etc. The most important region among them is the MWIR where the signature absorption lines of some important trace gases are located, including methane, ozone, and carbon dioxide. Other unique applications of this region include free-space optical communication, chemical gas-sensing, industrial leak detection, and medical diagnostics. LWIR is the region for thermal imaging, which can be used for military application such as night-vision and medical application such as bio-vision.

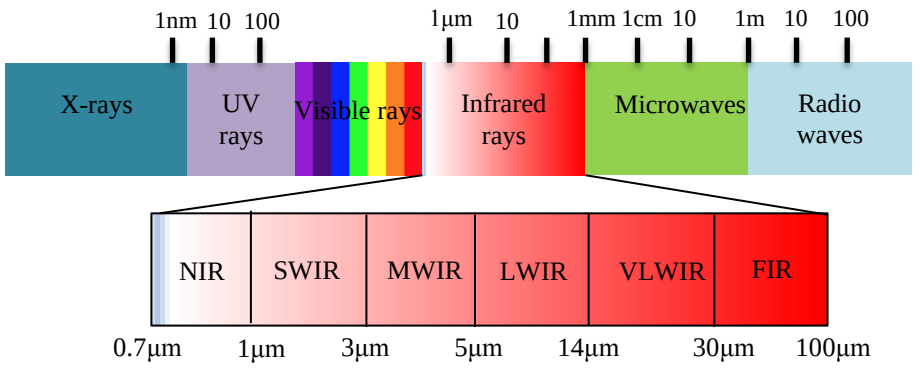

Figure 1-1: Electromagnetic spectrum with sub-categories in infrared region.

1.2 Motivation and background

The vast majority of gaseous chemical substances exhibit fundamental vibrational absorption bands in the mid-IR (2 to 30μm) spectral region, and the absorption of light in these fundamental bands provides a nearly universal means for their detection. As a result, this spectral region is often referred to as the *molecular-fingerprin*t region. Some common molecular bonds like *C-H*, *N-H*, *O-H*, *C-C*, *N-O*, *C=O*, and *C≡N* have their distinct absorption peaks in the mid-IR region so that molecules containing these bonds can be identified by their absorption spectrum. Some important molecules and their absorption peaks are shown in Figure 1-2.

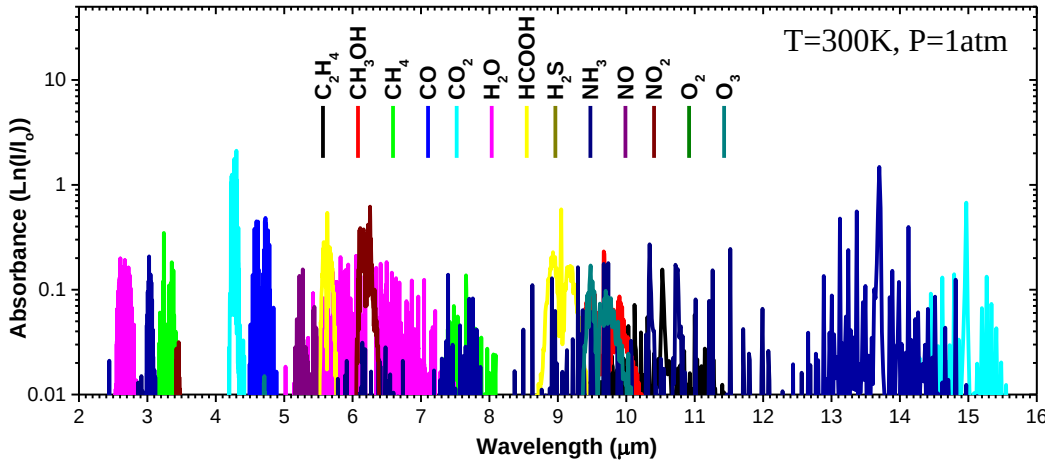

Figure 1-2: Absorbance of different molecules in MWIR and LWIR bands. HITRAN data [2], acquired from *http://www.spectraplot.com*.

Furthermore, the sensitivity of the detectors operating in the mid-IR region is typically several orders of magnitude higher than in the near-IR region. For example, Table 1-1 contains data comparing the different detection sensitivities for some common gases between the near- and mid-IR regions.

Table 1-1: Comparison of gas sensitivities between the mid-IR and near-IR regions [3].

Molecule	Detection limit			
	MWIR-LWIR		NIR-SWIR	
	ppb[1]	Wavelength (μm)	ppb	Wavelength (μm)
H_2O	2.0	5.94	60	1.38
CO_2	0.13	4.23	4000	1.55
CO	0.75	4.60	3000	1.55
NO_2	3.0	6.14	6000	0.68
CH_4	1.7	3.26	600	1.65
HCl	0.83	3.40	20	1.21
NH_3	0.80	10.30	1000	1.50

Detectors operating in the mid-IR region are used to detect toxic gases and greenhouse gases like CO_2, CH_4, NO_2, and CH_4, and thus can monitor the environment. They are also able to detect leaks and cracks in pipe lines by using thermal imaging techniques in the LWIR region. In the field of noninvasive medical diagnostics, infrared

[1] Part per billion

lasers can penetrate a few centimeters deep under the skin to sense cancer causing cells by detecting specific chemical changes. Also, they are used to identify the location of lymphatic tumors and can even be used to destroy them. In the field of defense, infrared countermeasures (IRCM) devices are used to jam an incoming heat-seeking missile by confusing its infrared tracking or guidance system, so that it fails to hit its target. The lasers operating in this region are also widely used to indirectly detect bulk explosives by imaging the characteristic shapes of the explosive charge, detonators and wires or by directly detecting the chemical composition or dielectric properties of the explosive material. Mid-IR lasers can penetrate the earth's atmosphere through two infrared atmospheric windows (3-5μm and 8-14μm) without encountering water or carbon dioxide absorption, as shown in Figure 1-3.

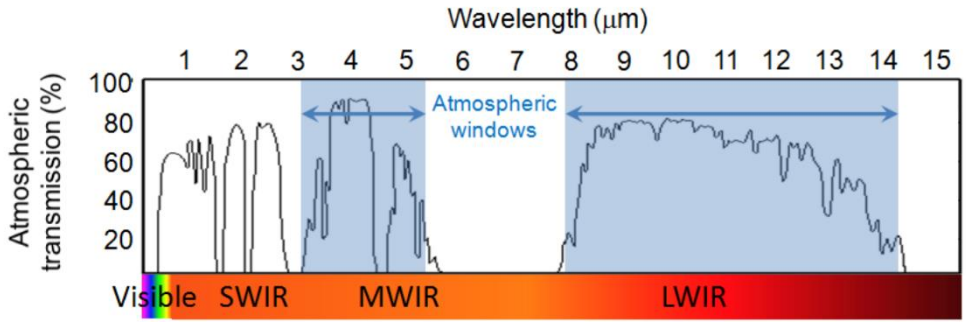

Figure 1-3: Windows of transparency through the atmosphere include infrared regions of the electromagnetic spectrum [4].

In these two windows, the atmosphere is relatively transparent compared to near infrared wavelengths. This facilitates the transmission of mid-IR free-space communication (FSO) signals which are especially important for military transmissions (aircraft to aircraft, satellite to ground, etc.) and telecommunications.

The first demonstration of semiconductor lasers in the mid-IR spectral region was in 1963 from an InAs *p-n* junction at 3.1μm operated in pulsed mode at cryogenic

temperatures [5]. In the 1980's, lead-salt based materials were extensively investigated because they could cover a wide range of mid-IR spectrum (4-30μm) [6]. However, they exhibited low output power, cryogenic operational temperature, and poor material quality. Substantial progress was made in the 1990's when molecular beam epitaxy (MBE) was used for the growth of double heterostructures and quantum-well lasers. The most impressive results were obtained by engineering the band structure of quantum well lasers based on III-V materials [7, 8] as compared to IV-VI and II-VI based materials [9-13]. After 2000, three mid-IR sources (type-I quantum well lasers, quantum cascade lasers, and interband cascade lasers) based on III-V material systems were demonstrated with continuous wave (cw) room temperature operation especially in 2-6μm spectral region [14-20] and extended to 25μm at cryogenic temperature [21].

Among these three mid-IR sources, interband cascade lasers (ICLs) benefit from: type-II broken gap alignment to suppress non-radiative Auger loss, interband transition with long carrier lifetime without fast phonon scattering, and cascade process to recycle the injected carrier, and thus reduce the threshold current density. These benefits resulted in the demonstration of high temperature operation while consuming small input power compared to the other mid-IR sources. In the last decade, remarkable progress has been made in developing ICLs on GaSb substrates, mainly in the 3-4μm region [15, 22-28] and extended their room temperature operation to 5.6μm [29]. Unfortunately, GaSb-based ICLs suffer from poor heat dissipation, when designed to operate at longer wavelengths, due to the low thermal conductive InAs/AlSb-based superlattice structure used as the cladding for the laser waveguide. This poor thermal dissipation issue becomes severe when thicker superlattice cladding layers are used for

longer wavelength ICLs (a design requirement). As a result, these GaSb-based ICLs have high threshold current density in longer wavelengths [29]. To circumvent this limiting issue, a plasmon-waveguide design approach on InAs substrates, initially used in QCLs [30, 31], has been introduced. This approach has two advantages: (1) the heat dissipation is improved by replacing the low thermal conductive superlattice structure with high thermally conductive InAs in the cladding region, and (2) the light confinement is enhanced in the active region because of the larger refractive index contrast between the active and the cladding regions. Based on this approach and the characterization results from our previous lasers, several plasmon-waveguide ICLs grown on InAs substrates were designed to lase in the 4.6 to 6.5μm spectral region. These lasers are expected to perform better because the initial surface defect densities are found comparatively smaller than our previous lasers which indicate better material growth quality. The objective of this research (discussed further in Chapter 3) is to extensively characterize these lasers followed by analyzing their performance, comparing the results with the state-of-the-art values, identifying their strengths and weaknesses and finally making recommendations for future improvement. These recommendations and future directions will be beneficial in designing efficient ICLs for even longer wavelength region with the capability of demonstrating low threshold current density and higher operating temperature operation.

Laser output beams with single longitudinal mode and narrow line-widths are very important for many applications, especially in spectroscopy and laser-matter interactions, which require high selectivity and sensitivity. In the field of free space optical (FSO) communication between earth and space, the output beams from the mid-

IR lasers can propagate through the two atmospheric windows (see Figure 1-3) without much attenuation. So, it is important to study and measure the laser beam quality for evaluating their performance, especially for long distance propagation. Our previous studies on laser beam optics from plasmon waveguide ICLs were carried out at the temperature of 80K [32], which is less significant for practical applications; hence, it is important to extend these studies to room temperature operation. Considering the better performance of the recent plasmon waveguide ICLs (InAs based) at longer wavelength region, the study of their beam optics is important (this is further discussed in Chapter 4). The objective of this work is to measure the beam quality both in the growth and lateral directions at 300K and analyze their beam optics and compare it to our previous (low temperature) results and to state-of-the-art values. The outcome of this study will be useful to understand the laser beam optics better and can even be applied to our previous lasers.

Conventional lasers typically generate multimode lasing emission that is not suitable for many high sensitivity applications, especially in the detection of trace gases. There are many different techniques available to obtain single mode lasing emission (see Chapter 5); however, most of them required complicated design, additional fabrication and equipment, which increase their operational complexity. The concept of two-section cleaved-coupled-cavity (CCC) laser (proposed in 1980s [33-35] for generating single mode lasing emission is reconsidered and applied to interband cascade lasers as an alternative way to overcome some of the limitations associated with the contemporary techniques. Here, a focused ion beam (FIB) is used to fabricate a CCC laser by electrically separating an ICL into two dissimilar sections along with a narrow

air-slot milled on top of its mesa. The objective of this research was to fabricate the CCC lasers by using a FIB to generate a single longitudinal emission with good side-mode-suppression ratio. Another objective was to obtain a suitable FIB milling recipes to mill ~4-6μm thick gold layer and III-V epitaxial layers during the fabrication process. The single mode emission spectra from this CCC laser will extend the applications of ICLs (especially in the field of high sensitivity and selectivity applications) and the FIB recipes can be applied to investigate defects in III-V semiconductor materials (especially, defects located deep within the semiconductor epilayers).

High-speed optoelectronic devices are very promising in the mid-IR region due to the presence of two transparent atmospheric windows covering 3-5μm and 8-14μm spectral regions. The presence of these atmospheric windows needs high bandwidth lasers and detectors for free space optical communication from space to earth. In addition, some specific applications, such as heterodyne detection, require devices capable of high speed operation. The availability of both ICLs and interband cascade infrared photodetectors (ICIPs) in the mid-IR region will able to meet this demand because of their room temperature operation, high performance characteristics, and low power consumption. The main objective of this research (further discussed in Chapter 6) is to extend the functionality of the interband cascade (IC) family to high frequencies by investigating the high-speed performance of single-stage and multi-stage ICIPs. Another objective was to set up a free space optical link (1m long) to qualitatively measure its data transmission performance in terms of eye-diagrams. The results obtained in this research will be beneficial for understanding the carrier transport

mechanism in the frequency domain along with the possibility of establishing high speed FSO links.

The investigation of the carrier transport mechanisms between two major mid-IR semiconductor technologies based on interband and intersubband transition, which share the same concept of recycling carriers through cascading individual stages, will be interesting and illuminating if their fundamental key differences can be viewed from a different perspective. IC devices are based on interband transition (IB), which is relatively a slow process with carrier lifetime in the order of ~ns. On the other hand, quantum cascade (QC) devices are based on intersubband (ISB) transition, which is intrinsically a very fast process due to the fast phonon scattering with carrier lifetime in the order of ~ps. As a result, QC devices inherently suffer from much higher dark current compared to IC devices. The objective of this research (see Chapter 7) is to extract reverse saturation currents density from both IB based optoelectronic devices by fitting a modified photovoltaic cell equation and ISB devices by developing a semi-empirical model. These data are then compared by putting them into a single framework for a wide wavelength range to see if the fundamental carrier lifetime differences inherent to these devices are reflected. Another objective is to explore the direct consequence of the reverse saturation current density on device performance such as specific detectivity and open circuit voltage. This research is a different perspective of viewing the fundamental differences between two major semiconductor technologies in the mid-IR spectral region.

1.3 State-of-the-art mid-IR sources

■ Interband Cascade Laser (ICL)

The ICL is a low power consuming mid-IR light source that utilizes the advantage of the type-II band alignment of the InAs/GaSb material system. The concept was first proposed by Dr. Rui Q. Yang in 1994 [36]. The first experimental realization was reported in 1997 [37] and the ICL operated only at cryogenic temperatures [38, 39]. The gradual improvement in both design and growth technique as well as device fabrication advanced the performance of the ICL and increased the operating temperature to 250-286 K [40-42]. The design improvement included the optimization of the injector layer thickness, incorporation of "W" structure in the active region, and doping optimization.

One notable milestone in the development of ICLs was achieved in the Jet Propulsion Laboratory in the year 2005. Their 12 stage Distributed Feedback (DFB) ICL was able to lase in a single mode at room temperature with a 630A/cm^2 threshold current density. This laser was included later in the Tunable Laser Spectrometer (TLS) on the NASA Curiosity Rover which landed on Mars on August 6, 2012 to explore the Martian environment and look for evidence of life on Mars [43].

The room temperature (RT) threshold-input-power density of recent ICLs is as low as 0.35kW/cm^2 [24], which validates the superiority of the ICL as an energy-efficient mid-IR light source for practical applications. This low power consumption has been extended to the longer wavelength spectrum beyond 4.2μm by the NRL group, who demonstrated cw operation at temperatures up to 60°C and 45°C at wavelengths of 4.9 and 5.7μm, respectively [29].

At wavelengths near or beyond 6μm, ICLs based on a GaSb substrate were operated at temperatures up to 350K in pulsed mode. Their threshold current densities at room temperature were close to or higher than 500A/cm^2 (*e.g.* 660A/cm^2 at 6μm [44]), so they could not lase in continuous wave (cw) mode at room temperature. Recently, InAs-based ICLs are able to lase in pulsed mode at high temperatures (>350K) with emission wavelengths beyond 6μm and with significantly reduced threshold current density at room temperature (<400A/cm^2) [16]. As of today, the longest lasing wavelength achieved by an ICL is 11μm, operating at cryogenic temperature [14].

Since 2007, Dr. Yang's group in collaboration with Dr. Matthew B. Johnson (now at West Virginia University) and Dr. Michael B. Santos from the Physics and Astronomy department has been working on the research and development of IC-based lasers, detectors and photovoltaics; which include material growth, fabrication and characterization.

- **Quantum Cascade Laser (QCL)**

The quantum cascade laser is another mid-IR laser source that has been intensively investigated during the past 20 years. The first QCL was grown by molecular beam epitaxy at Bell Labs by Federico Capasso's group and lased at 4.2μm wavelength [45]. The QCL is based on intersubband transitions that can cover the entire mid-IR to THz region. The development of Mid-IR QCLs in the last few years [17, 18] has made it possible to reach remarkable performances with emitted powers in the 1-5W range [46]. The wall-plug efficiency, namely the ratio between extracted optical power and injected power in a laser device, has reached values as high as 27% in pulsed mode and 21% in cw mode [46]. More than 5W of cw output power at RT has been

achieved by employing advanced active region engineering in the InGaAs/AlnGsAs/InP material system [47]. On the other extreme of the Mid-IR spectrum, close to the phonon absorption band, Sb-based heterostructures have been successfully employed to improve the performance of long-wavelength Mid-IR QCL lasers operating at a wavelength of 17μm or longer [48]. Recently, QCL emission at 24.4μm and at 240K has been demonstrated by using the InGaAs/AlInAs material system [21].

- **Type-I quantum well laser**

Besides the cascade structures where the expected lasing wavelength can be engineered by changing the thickness of the quantum well, one possible way to cover the short wavelength range of the mid-IR spectrum is to use narrow-bandgap material with a type-I band alignment. These lasers are mainly based on a GaSb substrate and can operate in continuous wave mode at room temperature in the spectral range from 1.9 to 3.5μm [19]. In these spectral region, the state-of-the-art GaSb-based type-I QW diode lasers can produce above 1W of cw output power at room temperature with 360mW at 3μm, 160mW at 3.2μm (both at 17^{o}C). They maintain cw room temperature operation up to 3.44μm [49-51]. Recently, a cascade pumping scheme increased the output power up to 1.96W for a GaSb based diode lasers near 2μm [20].

However, these mid-IR diode lasers suffer from temperature sensitivity of both threshold current and external quantum efficiency above a 3μm lasing wavelength due to free carrier absorption and Auger recombination as well as lack of appropriate material combination. Furthermore, carrier leakage and thermal population in the active region result in undesirable high threshold current and low output power.

1.4 Dissertation outline

In Chapter 2 of this dissertation, the fundamentals of ICLs are discussed. This chapter starts with focusing on the material system of ICLs. The band diagram of these materials is shown with some common material properties tabulated for better understanding. Then the device structure of the ICL along with the operating principles are illustrated and briefly discussed. A schematic of a processed narrow-ridge laser is shown along with (plasmon waveguide) their brief processing steps. The main focus of this chapter is a discussion of the key figures-of-merit of different characterization techniques used in the subsequent chapters.

In Chapter 3, the performance of InAs based ICLs operating at 4.3 to 6μm wavelength range are discussed. After discussing the device structure, growth and fabrication, the result of characterization are discussed and analyzed. The figures-of-merit are based on threshold current density, maximum operating temperature, output power, voltage efficiencies, quantum efficiency, and wall plug efficiency. The results are discussed and compared to the state-of-the-art values.

After discussing the regular performance of the ICL in Chapter 3, the far-field patterns of some high performance lasers are discussed in Chapter 4. The experimental setup and device characterization of the far-field pattern are discussed. The far-field pattern both in the growth and vertical directions of the lasers are obtained. The shape of the far-field is compared to the pure Gaussian beam in terms of M^2 value along with other figures-of-merit.

Chapter 5 describes the single mode operation of an ICL by using a two-section cleaved-coupled-cavity laser (CCC). Narrow slots were made by focused ion beam

(FIB) milling to separate the laser into two FP cavities. The single mode laser is obtained with a sufficient side mode suppression ratio and low continuous tuning range.

In Chapter 6, the high-speed operation of interband cascade photodetectors (ICIP) is discussed. This chapter mostly focused on the experimental setup for high frequency operations, as there are challenges in eliminating the experimental noise sources to retrieve a clean spectrum, especially when the laser frequency approached the gigahertz range. After optimizing the setup, the high frequency bandwidth of the ICIP is obtained and then compared to the simulated result. In addition, a one-meter free space optical link is established and its quality of transmission is evaluated in terms of eye-diagrams.

Finally, in Chapter 7, the carrier transport in interband and intersubband structures is discussed. By developing a semi-empirical model, the reverse saturation current is extracted and plotted in a single platform that portrayed a common key feature of cascade devices.

Chapter 2: Fundamental of interband cascade laser

2.1 Introduction

There are different types of lasers that can operate in the mid-IR region such as the quantum cascade laser (QCL), interband cascade laser (ICL), and type-I quantum well laser. Among them, the ICL exhibits low threshold current density and low input power. In this chapter, the fundamental device physics, material system, structure, growth, processing, fabrication and characterization techniques of ICLs will be briefly discussed.

2.2 Material properties

Latticed-matched semiconductor compounds for engineering IC related devices are obtained by combining group-III elements, such as Al, Ga, and In, with group-V elements such as N, P, As, and Sb, which gives 12 possible binary compounds. Among these combinations, the most important compounds are GaAs, GaN, GaP, GaSb, InAs, InSb, and InP. For fabricating the ICL, InAs, GaSb, and AlSb are the materials of choice for some of their unique properties. These three compounds crystalize in a zinc blende lattice structure. Moreover, they can form a type-II quantum-well alignment (see Figure 2-1 (a)) which is crucial for the underlying physics necessary for the ICL. These three materials have nearly-equal lattice constant (~6.1Å), as shown in the Figure 2-1 (b), and band-gaps in the range from 0.3 to 1.6eV. The similarities in structural properties enable them to be used as epitaxial layers to form type-II quantum wells and superlattices.

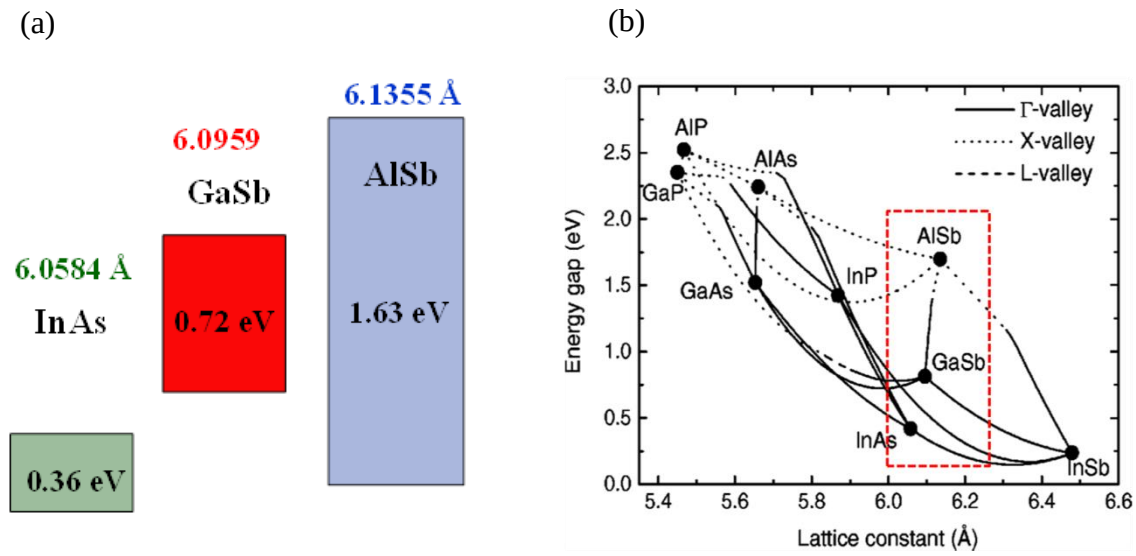

Figure 2-1: (a) Type-II band-gaps and alignments, (b) Materials highlighted are from the 6.1Å family [52].

Some properties of these three semiconductor materials from 6.1Å family are listed in Table 2-1.

Table 2-1: Common properties of III-V semiconductor materials from the 6.1Å family.

Properties	**InAs**	**GaSb**	**AlSb**
Bandgap [eV]	0.354	0.726	1.58
Nature of Bandgap	Direct	Direct	Indirect
Crystal Structure	Zinc Blende	Zinc Blende	Zinc Blende
Lattice Constant [Å]	6.06	6.10	6.14
Molar mass [g/mol]	189.74	191.48	148.74
Density [g/cm^3]	5.67	5.61	4.26
Melting Point [^{o}C]	942	712	1060
Thermal Conductivity [W/cm*k]	0.27	0.32	0.59
Thermal Exp. Coeff. [$\times 10^{-6}$K^{-1}]	5.37	7.75	2.55
Refractive index	3.51	3.73	3.3

2.3 ICL fundamentals

ICLs are a type of infrared laser diode that can produce coherent radiation over a large part of the mid-IR region. They are fabricated from epitaxially-grown semiconductor heterostructures composed of layers of indium arsenide (InAs), gallium

antimonide (GaSb), aluminum antimonide (AlSb) and related alloys. Among these materials, InAs and AlSb are used in the cladding region and injection region. The conduction band edge of InAs is below the valence band edge of GaSb, and AlSb has a very large conduction band offset with InAs. These two properties allow the formation of a type-II band alignment that makes ICLs possible. Also, the negative InAs alignment to gold makes it easy to form an ohmic contact instead of a Schottky contact, which allows it to be suitable as a cap layer.

The band diagram of one cascade stage of a typical ICL with a "W" type active region is shown in Figure 2-2. In this structure, the active region is sandwiched between the electron and hole injection region. Under forward bias, the electrons are injected from the injection region ① of the preceding cascade stage to the active region ② into the electron level E_e. Since the electrons at this level are blocked by the bandgap region of GaInSb layer, and there is a hole level into the valence band of this layer, the electrons will relax down diagonally to the hole state by emitting a photon. The value of the coupling between these electron-states and the hole-states are designed to make this transition happen. These electrons in the E_h state then cross the thin AlSb layer and enter into the neighboring GaInSb and GaSb layers③. They then tunnel and scatter into the conduction band of the next injection region ④ and are ready for recycling by the next cascade stage⑤. The strong spatial interband coupling in type-II quantum well facilitates this tunneling.

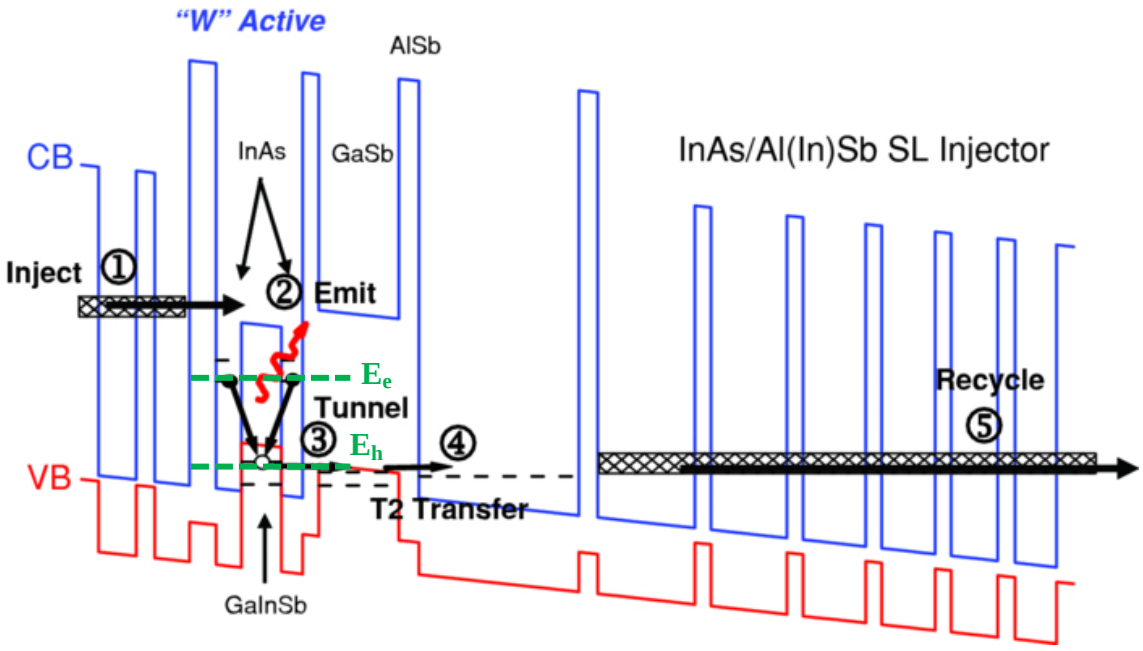

Figure 2-2: The operation of an ICL is described by steps 1 to 5 [23].

The injection region is designed to form a conduction miniband as shown in Figure 2-2 at an operating electrical field. The QWs in this region are strongly coupled that provide a smooth transport path for the electrons to get recycled by the adjacent cascade stages. This cascade stage leads to sequential photon emission with quantum efficiency higher than the conventional unity. The lasing wavelength of an ICL can be determined by the energy separation between the electron-state E_e and the hole-state E_h by adjusting the thickness of the constituent quantum wells. Furthermore, the Auger recombination losses can be suppressed by band-structure engineering. Thus, ICLs can have lower threshold current and efficient performance than many other types of lasers.

For the laser to sustain oscillation, the gain in the laser medium must be greater than the total loss of the cavity. The cavity loss includes internal loss α_i and mirror lossα_m. The internal loss arises from waveguide light scattering and free carrier absorption and mirror loss arises from the Fresnel reflection of the cleaved facet of the

laser. To calculate this threshold gain, we combine all the sources of loss into one lumped loss coefficient (α). The schematic of a resonating cavity is shown in Figure 2-3.

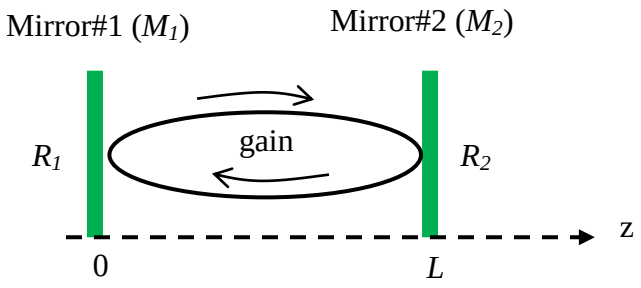

Figure 2-3: Schematic of a resonating cavity.

To explain the operation of a resonating cavity, consider that the cavity is made of mirrors M_1 and M_2 with reflectances R_1 and R_2 and spaced by distance L as shown in Figure 2-3. A beam of irradiance I_o starting at M_1 on reaching M_2 has become $I_1 = I_o e^{(g-\alpha)\mathrm{L}}$ where g and α are gain and loss coefficient respectively. On reflection from M_2 and travelling in return through the medium and undergoing reflection at M_1, the irradiance becomes $I_2 = I_o R_1 R_2 e^{2(g-\alpha)\mathrm{L}}$. The round-trip gain G is defined as:

$$G = \frac{I_2}{I_o} = R_1 R_2 e^{2(g-\alpha)\mathrm{L}} \quad (1)$$

The threshold condition for laser oscillation is $G=1$, that gives

$$R_1 R_2 e^{2(g_{th}-\alpha)\mathrm{L}}=1 \quad (2)$$

where g_{th} is the threshold gain coefficient and can be re-written as:

$$g_{th} = \alpha_i + \frac{1}{2L} ln \frac{1}{R_1 R_2} \quad (3)$$

The first term in the above equation is the internal loss of the cavity and second term is the loss due to the mirror reflectivity.

2.4 Challenges in ICL

An ICL is made from a complex structure with a couple of thousand constituent semiconductor layers composed of III-V materials. Careful design, growth, thermal management, and other related parameter optimization are required for high temperature operation and low threshold condition. Some of these challenges are discussed briefly in the sections below.

- **Growth by molecular beam epitaxy (MBE)**

ICL structures are grown on an InAs or GaSb substrate with more than 2,000 constituent semiconductor layers. Some of these layers are even a fraction of an atomic monolayer thickness. The growth of this complicated structure involves movement of several shutters in the MBE chamber with careful calibration and optimization of growth temperature and fluxes of source materials. As a result, it is indeed a challenging task for the MBE-grower to achieve a high-quality uniform strain-balanced structure. In addition, these optimizations and calibrations are machine dependent and repeated growth and feedback process is required to obtain a good recipe.

- **Carrier rebalancing**

In early ICL design, an InAs quantum well in the electron injector was doped moderately with Si to $4\times10^{17}cm^{-3}$. As a result of this low doping, the internally generated carrier densities (namely holes) significantly exceeded the doping densities (electrons) resulting in the need for excess voltage to achieve threshold condition. This design has been modified based on the concept of *"carrier rebalancing"* introduced by the *Naval Research Lab* [24]. They found that most of the internally generated electrons and holes reside in quasi-equilibrium in their respective injectors due to the presence of

an opposing internal field which is approximately ~$4k_BT$ higher than that in the active region. So, they overcome this misalignment by heavily n-doping the injector region. This concept has been adopted by ICL community to enhance device performance.

- **Thermal management**

Thermal management is very critical for ICL operation. The active region of the laser generates most of the heat that needs to be transported away efficiently to achieve high temperature operation. In regular ICL design, a superlattice structure was used in the cladding region due to the flexibility in design. However, the thermal conductivity of an InAs/AlSb superlattice structure is ~0.03W/cm.K [53] which is almost order of magnitude lower than the thermal conductivity of bulk InAs (0.27W/cm.K) and GaSb (0.32W/cm.K) materials. This low thermal conductivity limits the laser's ability to achieve high temperature and large output power which leads to reliability concerns by introducing local strain and thermal stress. In the cw current mode, the laser generates a high amount of heat that must be removed efficiently to maintain population inversion. To expedite the heat removal process, often a thick layer of gold in the range of 3 to 6μm is deposited by a low cost electroplating technique on top of the narrow-ridge lasers. The heat removal process can be further improved by mounting the laser in such a way that the top mesa of the laser will be in contact with the heat-sink. This process of mounting the laser is called "epi-down" mounting. In this mounting technique, the heat removal becomes faster and efficient because the active region is located closer to the heat-sink.

- **Waveguide design**

The superlattice cladding layer has a refractive index of ~3.37. This is slightly smaller than the refractive index of the cascade region, which is in the range of 3.43 to 3.47. As a result, the waveguide design requires a thicker SL cladding layer to confine light in the active region, which is detrimental in terms of heat transport. The superlattice cladding layer can be made thinner but this will result in a substantial leaking of the optical wave into the substrate. The optical loss and the heat transport have a detrimental impact on the performance of ICLs for longer wavelengths where a thicker cladding layer is a design requirement. This problem can be circumvented by using a plasmon waveguide approach which was used in the early QCL design for long wavelengths [54-57]. In this design, the refractive index of the InAs layer can be modulated by adjusting the doping level and can be reduced to even below ~3. It results in a sharp refractive index contrast between the core and cladding layers, and consequently better optical confinement factor. In addition, the use of a plasmon waveguide is more favorable for an ICL because of its sensitivity to transverse electric (TE) polarization, in contrast to the QCL which is only sensitive to transverse magnetic (TM) polarization. However, the high doping concentration in this plasmon waveguide will increase the free carrier absorption. So, often a trade-off is made to improve device performance. Further waveguide design modification can be made by introducing an intermediate cladding layer between an outer cladding and a separate confinement layer (SCL) [58] to tightly confine the light into the active region.

- **Electron injection region**

The electron injection region is one of the most important regions. It facilitates the carrier transport from one stage to the next stage and holds most of the input voltage. Essentially, the miniband of this injection region should align properly with the active subband of the next stage. Otherwise, excessive bias would be required to overcome this potential misalignment. The length of the injector region is also important. In our recent ICL design especially for longer wavelengths, the electron injector was shortened by one quantum well from 5 to 4.

- **Top metal contact**

The optical loss associated with mode leakage from the top metal layer is significantly less in TE polarized ICLs than TM polarized QCLs. This metallic mode leakage can be further reduced by inserting a dielectric insulating layer such as SiO_2 underneath the metal layer. Typically, these insulating materials have weak absorption in the mid-IR region and they become transparent to the incident light of interest. The refractive index of SiO_2 is 1.4, which is much lower than the refractive index of the active region which is in the range of ~3.43-3.47. This large refractive index contrast can improve the mode confinement factor and essentially can act as a top optical cladding layer. So, the top metallic contact could be rather advantageous if properly designed. In addition, this strip type metallic contact on top of the mesa can be made as small as 2-3μm to further reduce the optical loss to a minimum value.

- **Long wavelength ICLs**

There are many design challenges involved in long wavelength infrared lasers compared to short wavelength lasers. In long wavelength ICLs, the bandgap of the

active region should be smaller to accommodate a longer lasing spectrum. As a result, the conduction band gets easily populated at high temperature, which introduces free carrier absorption loss. The coefficient of this free-carrier absorption in doped semiconductors is roughly proportional to λ^2, which translates into larger optical waveguide losses. Furthermore, thicker quantum wells are necessary in long wavelength lasers to reduce the electron-hole wave function overlap. As a result, the differential gain is affected, and more cascade stages are necessary. To maintain the lasing, more injection is necessary which in turn increases the free carrier absorption. Finally, the non-radiative Auger decay rate increases for longer wavelength because it is proportional to n^3 (# of carriers). This decay mechanism can significantly reduce carrier lifetime. All the design requirements mentioned above pose significant challenges to obtain a low threshold current density and high output power in the long-wavelength spectral region.

- **Mechanical stress**

ICLs are comprised of thousands of layers made from different III-V materials, along with insulating layers and a thick electroplated gold layer on top. The insulating layer has a thickness in the range of 300 to 400nm and electroplated gold is in the range of 4 to 6μm. The insulating layers along with epi-gold layer have different thermal expansion coefficients and Young's moduli which can introduce different types of mechanical stress at different operating temperatures and conditions. In an unpublished work from our group, we found that a 470nm SiO_2 insulating layer can exert a tensile stress of 850MPa (-ve) and 350nm of Si_3N_4 can exert a 730MPa (+ve) compressive stress. Hence, a combination of these two layers is necessary to effectively reduce their

opposite stresses. These mechanical and thermal stresses are made worse by temperature cycles and often cause cracks and delamination in the mesa structure. Furthermore, the stressed in the insulating layers along with top gold layers can easily pop-off during ball bonding process.

- **Other issues**

The output power comes out from the two facets of the lasers, but the power coming out from the rear facet is wasted. To increase the reflectivity of this facet, often a high reflective (HR) metal on insulator combination such as Al_2O_3/Ti/Au or dielectrics such as Al_2O_3/Si are used [59]. In typical ICLs, the cleaved facet has a low reflectivity of ~30%, which can be increased by coating by $\lambda/4$ dielectric multilayers. However, the long wavelength ICLs limit the practicality and reflectivity of dielectric coatings, as the coating thickness scales with the wavelength. Another purpose of these coatings is to protect the facet from long term degradation. The design and deposition of these reflecting materials are another challenge for ICLs.

2.5 Device processing and fabrication

After growing the laser structure by molecular beam epitaxy (MBE), the lasers are processed into broad-area and narrow-ridge geometries as shown in Figure 2-4 below.

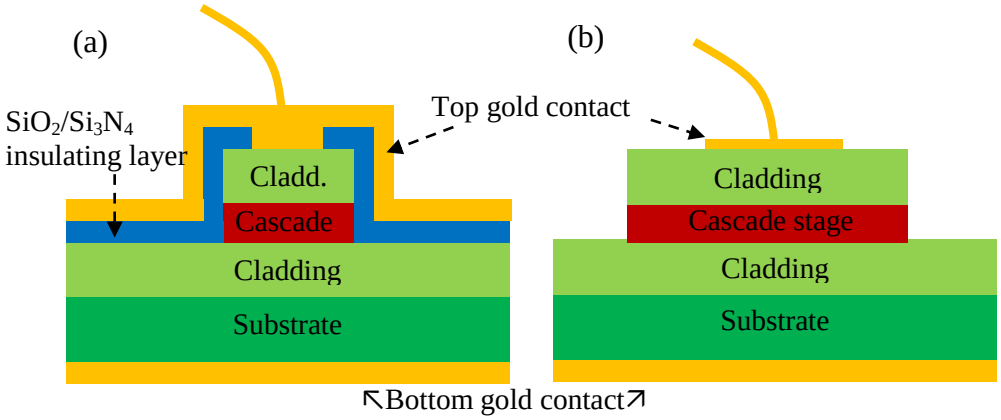

Figure 2-4: The schematic of a processed ICL in a (a) narrow-ridge and (b) broad-area geometries. The layer dimensions are not to scale.

The typical processing steps include: (a) standard cleaning, (b) mesa etching, (c) insulating layer deposition, (d) contact opening, (e) top contact deposition, (f) lapping, (g) bottom contact deposition, and (h) mounting and wire bonding. After cleaning and standard contact photolithography, wet-chemical etching is used to form a mesa structure by etching deep down below the active region. Then, ~200nm silicon nitride followed by ~200nm of silicon dioxide is sputter deposited as an insulating layer. This step is followed by reactive ion etching (RIE) to open a window on top of the mesa. This window is opened to deposit 30/300nm of Ti/Au layer by a sputtering technique as top metal contact. For a narrow-ridge laser, a ~4-6μm layer of electroplated gold was deposited on top of this sputter deposited gold for better thermal dissipation as shown in Figure 2-4 (a). After lapping down to ~150μm, the bottom gold contact was deposited by the same sputter technique. Next, the sample was cleaved to form laser bars with cavities that are ~0.5 to 3mm long (both facets left uncoated). Finally, these bars were indium-mounted onto a copper heat-sink and bonded by using gold wires. The device was then ready for characterization.

2.6 Laser characterization

After the device is processed, it is mounted on the cold finger of the cryostat for characterization. Some typical characterization techniques used in this dissertation are described briefly in the sections below. As mentioned in the earlier section, an ICL structure was usually processed as a broad-area laser followed by a narrow-ridge laser to extract parameters such as threshold current density, maximum operating temperature, thermal resistance, slope efficiency, quantum efficiency, wall-plug efficiency, and voltage efficiency. The theory formalism and parameter extraction of these figures-of-merit are very similar to that of a diode laser and can be found in standard laser textbooks [60]. The following section will discuss some of these parameters in brief.

■ Laser spectrum

The laser spectrum is the measurement of the emission frequency of the laser. When properly aligned, the laser will start lasing at a slightly higher threshold current. The emission wavelength of lasing is defined as the wavelength at which the intensity of the laser emission is at the maximum value. The laser spectrum gives an approximate estimation about the threshold current and voltage. Also, by inspecting the laser spectrum we can identify the maximum operating temperature of the laser.

■ Light-current-voltage (L-I-V) characteristic

The L-I-V is one of the most important properties of a semiconductor laser. This curve can be obtained by measuring the output power and voltage as a function of bias current. The threshold current, output power, slope efficiency, series resistance, and

electrical-to-optical power conversion efficiency can be obtained from this L-I-V curve. A schematic of a typical L-I-V curve is shown in Figure 2-5.

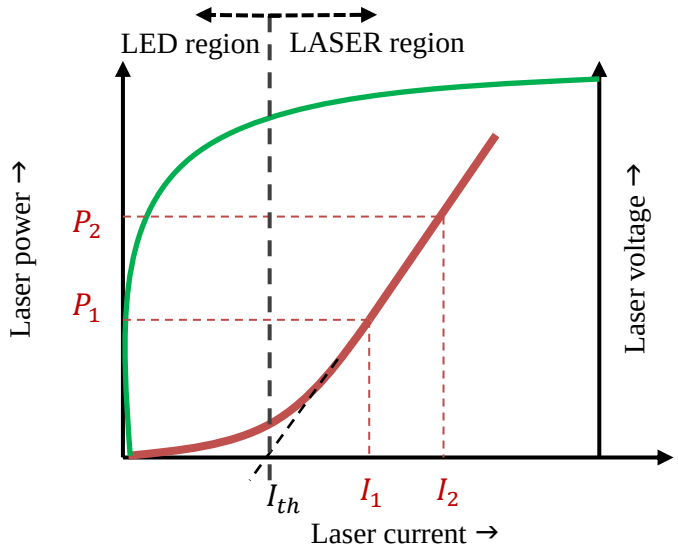

Figure 2-5: A typical L-I-V curve of an arbitrary laser.

■ Threshold current

The threshold current is defined as the minimum current required to achieve lasing action. Before achieving a threshold current condition, the laser emits spontaneous emission. When the applied current equals the threshold current, the gain of the active medium become equal to the sum of all loss such as internal loss and mirror scattering loss. When the injection current is above the threshold value, the laser power increases much faster, and the device starts lasing. This threshold current (I_{th}) can be estimated from the L-I-V plot as shown in Figure 2-5.

■ Slope efficiency

The laser efficiency in converting electrical power to optical power is determined by the slope of the L-I curve. It can be obtained by using the double point method as shown in Figure 2-5 and the following equation:

$$\eta_s = \frac{dP}{dI} = \frac{P_2 - P_1}{I_2 - I_1} \tag{4}$$

where P_1 and P_2 are the output power of the laser at the forward current of I_1 and I_2, respectively.

- **Internal quantum efficiency**

The Internal quantum efficiency is the fraction of injected electrons converted into photons, or equivalently the ratio of the radiative recombination rate to the total recombination rate. In other words, it can be defined as the number of emitted photons inside the cavity per electron by the following equation:

$$\eta_i = \frac{\#\ of\ emitted\ photons\ from\ active\ region}{\#\ of\ injected\ electrons} = \frac{P_{int}/_{h\upsilon}}{I/_e} \tag{5}$$

where P_{int} is the optical power emitted from the active region and I is the injected current. The internal quantum efficiency can be obtained by determining the external quantum efficiency of a series of lasers with varying cavity lengths. They can be related by the following equation.

$$\eta_{ext}^{-1} = \eta_{int}^{-1} + \eta_{int}^{-1} \frac{\alpha_i}{\frac{1}{2L \ln\left(\frac{1}{R_1 R_2}\right)}} \tag{6}$$

Plotting the inverse of the measured external quantum efficiency as a function of the cavity length leads to a straight line. The slope of this line gives the value of internal loss and the inverse of the intercept gives the internal quantum efficiency. It is widely accepted that the internal quantum efficiency is independent of the laser cavity length or carrier injection current.

- **External quantum efficiency (or differential quantum efficiency)**

The external quantum efficiency is a very useful parameter from which the internal quantum efficiency and, in turn, the internal loss can be determined. External quantum efficiency is defined as the number of received photons per electron above threshold. In other word, it is defined as number of photons emitted per electron-hole pair recombination above threshold. So, external quantum efficiency can be written as:

$$\eta_d = \frac{\#\ of\ emitted\ photons}{\#\ of\ injected\ electrons}$$

$$\eta_d = \frac{P_o/_{h\upsilon}}{I/_e} = \frac{dP}{dI}\frac{q}{h\upsilon} = \eta_s \frac{q}{h\upsilon} \tag{7}$$

$$\eta_d = \eta_i \frac{\alpha_m}{\alpha_m + \alpha_i}$$

where η_i is the internal quantum efficiency, α_m and α_i are the mirror loss and internal loss, respectively. The external quantum efficiency is smaller than the internal quantum efficiency for a typical laser. This reflects the presence of losses in the laser cavity. Not all photons generate inside a laser cavity contribute to the output of the laser.

- **Wall-plug efficiency or overall power conversion efficiency**

The wall-plug efficiency of a laser system is its total electrical-to-optical power efficiency, i.e., the ratio of optical output power to consumed electrical input power. The wall-plug efficiency is defined as:

$$\eta_p = \frac{P_{op}}{I_{op}\, V_{op}} 100\% \tag{8}$$

where, P_{op} is the output power at the operating current, I_{op} is the operating current, and V_{op} is the operating voltage. This wall plug efficiency can be obtained from the L-I-V curve.

■ Series resistance

The series resistance of a laser is the sum of the bulk electrical resistance and the contact resistance. A higher series resistance of the laser generates heat when a higher bias current is applied. As a result, the overall wall-plug efficiency is degraded. This series resistance can be calculated form the L-I-V curve when the forward bias current is much higher than the threshold current.

■ Threshold current dependence with temperature

Semiconductor laser performance is temperature sensitive. This sensitivity of the laser is based on the intrinsic losses at high temperature. When the temperature of the laser is raised, the intrinsic loss increases and therefore the internal efficiency decreases. In addition, other losses such as carrier leakage and Augur recombination scale up with temperature. The increase of the laser current threshold can be described by an empirical relation:

$$I_{th} = I_o e^{\frac{T}{T_o}} \tag{9}$$

where, T_o is the characteristic temperature of the laser. The higher the characteristic temperature, the better the thermal performance of the laser.

■ Thermal resistance

The thermal resistance of a laser is a measure of the quality of heat transport inside the laser structure, as well as the whole package the including indium solder and plated copper heat sink. In cw mode operation, the high cw current through the laser creates an excessive amount of heat inside the thin active core region. The generated heat is then transported through the substrate at the back to the heat sink. The efficiency of the heat transportation depends on the presence of thermal resistance of the

semiconductor materials. One of the techniques to measure the thermal resistance is to apply very short pulsed current with a low duty cycle (less than 1%) and then compare the threshold current to that at the cw temperature. Due to this pulsed current, joule heating is negligibly small and the thermal resistance of the laser is estimated by the following equation:

$$R_{thermal} = \frac{\Delta T}{V_{th} J_{th}} \ [K \ cm^2/kW] \tag{10}$$

where ΔT is the temperature difference, V_{th} is the threshold voltage and J_{th} threshold current density. An illustrative plot is shown in Figure 2-6 to explain how the thermal resistance is estimated.

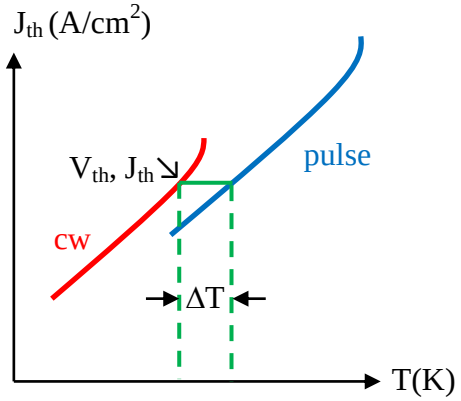

Figure 2-6: An illustrative J_{th} vs. T plot to explain the calculation of thermal resistance of any laser.

■ Voltage efficiency

Another important parameter of laser characterization is voltage efficiency. It tells about the unwanted voltage drops across the device and hence can be defined as:

$$V_{efficiency} = \frac{N_c * 1.24/\lambda}{V_{th}} \tag{11}$$

where N_c is the number of cascade stage, λ is the lasing wavelength in μm and V_{th} is threshold voltage. According to the design, the sum of the voltage drops across the cascade stages, the numerator of Equation (11), should appear as the threshold voltage of the laser if there is no parasitic voltage drops across the structure. However, some parasitic voltage drops occur due to the ohmic series resistance of the substrate and the superlattice cladding, and a non-ohmic part that may be associated with various band discontinuities in the structure. In addition, the voltage may drop in the contact.

2.6.1 Near-field

The near-field of a laser beam is located at a distance smaller than the Rayleigh length. For semiconductor lasers, this distance is very small, in the range of a few microns and is located close to the laser facet. As a result, a microscope and complex setup is often necessary to characterize the near-field beam profile. In our experiment, we mainly focused on a far-field measurement. However, the near-field beam profile is calculated using standard slab waveguide theory by our previous group member and details can be found in his dissertation [61].

2.6.2 Far-field

The far-field is defined as the distance located more than the Rayleigh length away from the laser. There is an angular spread of the laser beam both along growth and parallel directions of the laser structure. The amount of spreading depends on the vertical and lateral guiding mechanisms, refractive index contrast between the core and cladding, waveguide design, bias current, heat generation etc. The far-field profile can be estimated by Fourier transforming the near-field. The far-field pattern is characterized for both the growth and lateral directions. Usually a detector sensitive to

the laser's wavelength was placed in front of the laser and then rotated along the growth and vertical directions. Along the growth direction, the far-field pattern has a single lobe in its output. But a multimode output is very common along the lateral direction based on the size of the laser. There are many figures-of-merit for characterizing the far-field pattern of a laser. One important parameter is to compare the field pattern to a pure Gaussian beam by using the beam quality factor (M^2). Other important parameters include the brightness of the laser, the size of the laser spot, and the beam parameter product.

2.6.3 High frequency measurement

The most important parameter in the high frequency measurement is the 3-dB bandwidth of the laser that measures the speed of operation. In this high frequency experiment, a special device fabrication and mask design is necessary to minimize the parasitic capacitance and resistance (*i.e.* the *RC* time constant) to achieve the maximum bandwidth. The main sources that limit high speed operation are the bonding pad capacitance, contact resistance, device series resistance and inductance of the bonding wire. In addition, if is challenging to eliminate the unwanted interference coming from elsewhere inside the device. For a free space optical communication link, the quality of data transmission can be measured in terms of an "eye-diagram." This eye diagram is the output measured by an oscilloscope when the input is a pseudo-random bit sequence. The openness of the eye diagram is a good measure of the link quality.

2.6.4 Cleaved-couple-cavity laser (CCC)

Among the many different techniques for generating single mode lasing, the CCC laser is the easiest and least complex. The main figure-of-merit of a single mode

laser is the side mode suppression ratio (SMSR). In an ideal laser, the main spectral peak of a laser contains all the power produced by the device. But in reality, the laser signal includes side peaks, also called side modes, that contain some power. The SMSR is defined as the amplitude difference between the main longitudinal mode and the largest side mode in decibels. The tuning range of the laser can be continuous or quasi-continuous. The range of continuous tuning is a mode-hop free lasing spectrum. This is very useful in sensing and spectroscopic applications, where very high resolution is needed. Quasi-continuous tuning counts the mode-hops in its spectral output and can be useful in low resolution applications.

2.7 Conclusion

The ICL has the potential to be used in various fields of application that require low power consumption and room temperature operation in the mid-IR region. The laser structures can be grown on GaSb substrate for operation at short wavelengths and on InAs substrate for long wavelength operation. The common ICL characterization techniques include output power, maximum operating temperature, voltage efficiency, slope efficiency, and wall-plug efficiency. Besides these regular figures-of-merit, the far-field pattern identifies its beam quality both in the growth and lateral directions. The 3-dB bandwidth measures the speed of high-frequency operation and the eye diagram indicates the quality of the FSO link. Finally, a high side mode suppression ratio is needed for a lab-on-a-chip single mode operation of an ICL. All these features of the ICL will be discussed in the following chapters with experimental demonstration.

Chapter 3: InAs based interband cascade laser

3.1 Introduction

The interband cascade laser (ICL) is a type of laser diode that can produce coherent radiation to cover the mid-IR spectral region by utilizing the type-II quantum well and relatively long upper-level recombination lifetime of a conventional diode laser. It takes the advantage of connecting the active regions in a cascade fashion to generate multiple photons and ensure uniform carrier injection. As a result, an ICL has a very low input power consumption at room temperature, which makes it useful for many applications in the mid-IR region.

In this regard, we have designed, grown and characterized several ICLs by using a plasmon waveguide approach on an InAs substrate and investigated their performance in the 4.6~6μm wavelength region. Initially, two lasers were designed. Based on their performance, three more lasers were designed. Among them, one laser was able to lase beyond 6μm wavelength at room temperature with a significantly reduced threshold current density. This is the first time an ICL is demonstrated at room temperature above a 6μm wavelength in cw mode.

3.2 Background and motivation

The mid-IR region of the electromagnetic spectrum is very important for its unique applications in the fields of defense, free-space optical communication, industrial leak detection, medical diagnostics and especially chemical gas-sensing. The ICL and quantum cascade laser (QCL) are two major semiconductor technologies in this region. The ICL was first proposed at a conference in 1994 [62] by Dr. Rui Q.

Yang, the same year when the QCL was initially demonstrated [45]. From a historical perspective, the emergence of the ICL evolved from the early pursuit of intersubband lasing and research on interband tunneling in type-II quantum well systems [63-67], which has been mentioned on several occasions [68-70].

However, despite the favorable results projected by theoretical calculations and arguments [71, 72] and the fact that these lasers appeared at about the same time, the amount of effort expended in the development of ICLs has been very limited when compared with QCLs. Consequently, many aspects of ICLs have been unexplored or remained in the early phase. This is partially attributed to the less mature Sb-based III-V material system and related device fabrication procedure, as well as limited resources for the growth of Sb-based materials compared to more mature InP- and GaAs-based material systems and the widely available resources for them.

In the last decade, remarkable progress in developing ICLs on GaSb substrates has been achieved mainly in the 3-4μm wavelength regions [15, 22-28]. Low threshold current density (e.g. ~100A/cm^2 at 3.6μm) and low power consumption (<0.1W) at room temperature [15] have led to growing applications especially in chemical sensing. By using type-I quantum well (QW) active regions, ICLs have extended their emission wavelengths down to 2μm with enhanced device performance [73]. On the longer wavelength side, by employing a plasmon waveguide design approach on InAs substrates, which was initially used in QCLs [30, 31], ICLs have been demonstrated at wavelengths beyond 6μm and up to 11μm [14, 44, 74-76]. Recently, efforts have been made to improve GaSb-based ICLs at wavelengths approaching and beyond 6μm (pulsed mode) [77, 78]. At wavelengths near or beyond 6μm, these reported ICLs were

operated at temperatures below 350K in pulsed mode and with threshold current densities at room temperature that were higher than 500A/cm^2, so they could not lase in continuous wave (cw) mode at room temperature.

The *University of Oklahoma* has been achieving longer wavelength ICLs beyond 6μm with room temperature operation in cw mode on InAs substrate by adopting plasmon waveguide approach on an InAs substrate and optimizing related design parameters [58, 79, 80]. This work is the continuation of that effort with the achievement of room temperature cw operation with a low threshold above 6μm.

3.3 Device structure and material growth

The cascade region of an ICL is composed of the active region, electron injector and hole injector as shown in Figure 3-1. This active region in the cascade stages are composed of asymmetric AlSb/InAs/GaInSb/InAs/AlSb coupled quantum wells (QWs) which have a band edge similar to a "W" shape. The thickness of these quantum wells can be adjusted to tailor the lasing wavelength. The electron injector is composed of InAs/AlSb quantum wells and the central two InAs QWs were doped with Si to 2.6×10^{18}cm^{-3}. Compared to ICLs near 4.6μm [58], the number of QWs in the electron injector is reduced from 5 to 4 for the longer lasing wavelength and the doping concentration is also adjusted. The hole injector is composed of GaSb/AlSb quantum wells to prevent the electrons from flowing from the active region to the injector region. In the ICL structure, InAs has the smallest lattice constant and strain balance was achieved by using AlAs interfaces in the electron/hole injection regions. During the growth, antimony soaks were also used to ensure proper strain balancing of the AlAs/AlSb/InAs superlattice layer. The calculated band-edge diagram (based on a two-

band model) [67, 81] is shown in Figure 3-1 with a detailed layer sequence for one cascade stage of a representative 15 stage laser.

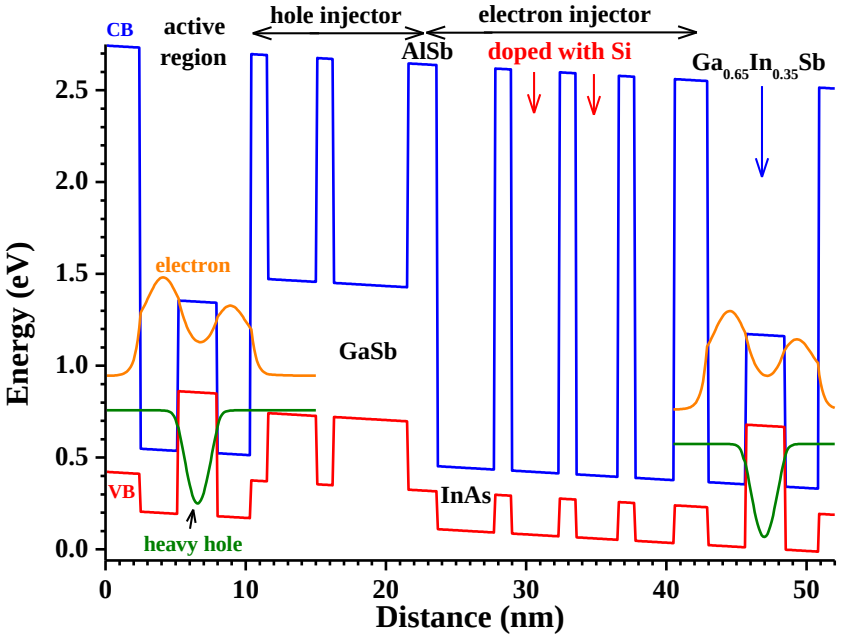

Figure 3-1: Calculated band-edge diagram of one cascade stage and the layer sequence of a representative 6μm laser.

Instead of discussing all the laser structures, a representative 6μm ICL structure is discussed. This representative laser was designed based on an improved waveguide configuration [58] with two 0.65μm thick undoped InAs separate confinement layers (SCLs), two 1.3μm thick InAs/AlSb/AlAs superlattice (SL) intermediate cladding layers, and highly doped n^+-InAs (1.1×10^{19} cm^{-3}) outer cladding layers, which have been proven to enhance optical confinement and reduce the optical loss for InAs-based ICLs near 4.6μm compared to the early design [58]. Some of the design dimensions and doping levels of recent NRC lasers are given in Table 3-1.

Table 3-1: Design parameters and doping levels of recent NRC lasers from Canada.

Wafer	Stage	Design λ (μm)	SCL (μm)	Top plasmon doping (cm^{-3})	Doping in Injection (cm^{-3})
V1183	10	~4.6	0.43	1.2×10^{19}	1.8×10^{18}
V1184	15	~6.5	0.65	8.3×10^{18}	1.8×10^{18}
V1189	10	~4.6	0.43	1.5×10^{19}	2.8×10^{18}
V1191	10	~4.6	0.43	1.5×10^{19}	3.9×10^{18}
V1192	15	~6.5	0.65	1.1×10^{19}	2.6×10^{18}

In comparison to GaSb-based ICL [15, 77, 78], where GaSb is used for SCLs, the optical confinement factor for an InAs-based ICLs would be reduced if the same number of cascade stages is used because the refractive index of InAs (~3.49) is substantially smaller than that of GaSb (~3.73). Hence, more cascade stages are desirable for InAs-based ICLs to achieve a comparable optical confinement factor. Nevertheless, the thermal dissipation can be improved, and the growth of an InAs-based ICL is easier because of the significantly reduced thickness of the SL cladding layer and the absence of mixed group-V InAsSb layers. Also, the carrier transport can be more efficient and smooth in an InAs-based ICL without using an n-type GaSb layer (that has a significantly higher conduction band-edge in contrast to InAs), possibly resulting in an improved voltage efficiency.

The ICLs investigated in this dissertation were grown on a 5cm diameter, 500μm thick S-doped n-type InAs (100) epi-ready substrate by using a custom V90 MBE machine at the National Research Council (NRC), Canada. The laser wafer was then processed into deep-etched broad-area (BA) (150 and 100μm wide) mesa stripe lasers and narrow-ridge (NR) (nominally 10-, 12-, 15-, and 20-μm wide) lasers by contact photolithography and wet chemical etching. The top mesa was opened by using phosphoric acid based wet chemical etching down to bottom separate confinement

layer. After wet etching, ~300-400nm of insulating layers comprised of Si_3N_4 followed by SiO_2 (~50% each layer) were deposited by using a sputtering technique for the narrow-ridge laser. This insulating layer was etched by SF_6 based reactive ion etching (RIE) technique to open a window on top of the mesa for contact metal deposition. After opening the window, a 30/300nm Ti/Au metal layer was deposited as a top contact layer by using sputtering technique. A 3 to 6μm thickness of gold was electroplated on top of the narrow-ridge devices. The wafers were then mechanically polished down to ~150μm, followed by a 30/300nm Ti/Au bottom contact layer deposition. A schematic and SEM image of a processed narrow-ridge laser is shown in Figure 3-2.

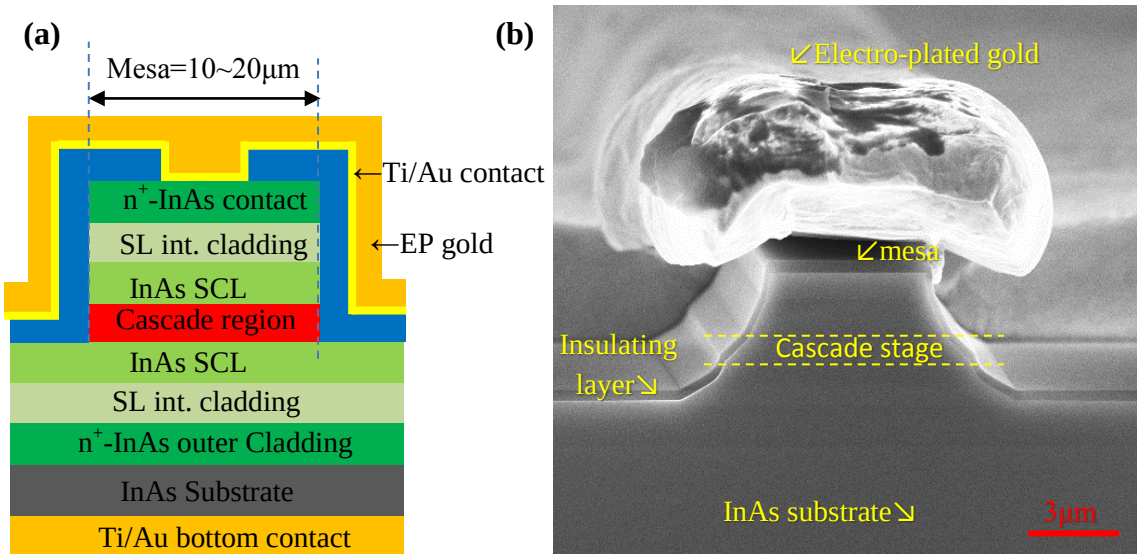

Figure 3-2: A processed narrow-ridge ICL (wafer name V1192) with (a) schematic (not to scale) and (b) Scanning Electron Microscopy image.

The processed wafers were then cleaved into 2mm long laser bars and the facets were left uncoated. These laser bars were mounted on a gold coated copper heat-sink using indium solder with the epilayer side up. This bar was placed on the cold-finger of

the cryostat for characterization. In pulsed measurements, the applied current pulse width was 1μs at a repetition rate of 5KHz. When the applied current was larger (e.g., >6A), the pulse width was reduced to 150ns to avoid possible Joule heating.

3.4 Results and discussion

In the first phase, two laser structures were grown by NRC, Canada on n-type InAs based substrates. One of these lasers had 10 cascade stages (V1183) and the other had 15 stages (V1184). These two laser structures were based on a type-II band alignment with the injector region doped with silicon at a level $1.1\times10^{18}cm^{-3}$ to $1.8\times10^{18}cm^{-3}$ for 10 stages and 15 stages with a designed lasing wavelength of 4.6μm and 6.5μm, respectively.

■ Broad-area laser performance

Broad-area lasers were processed into two regular mesa sizes of 100 and 150μm. The L-I-V characteristic curve of both V1183 and V1184 lasers are shown in Figure 3-3.

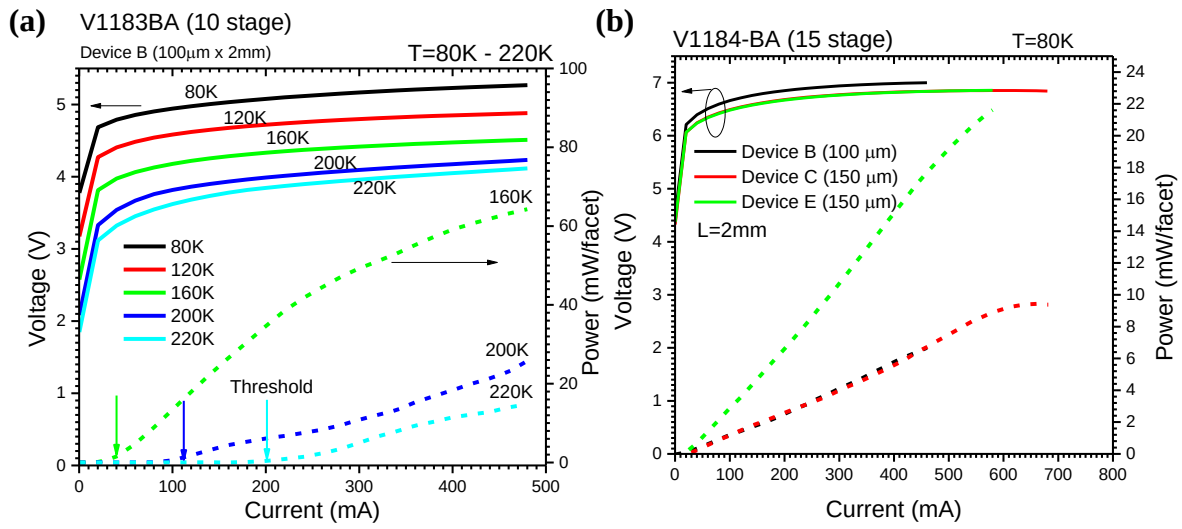

Figure 3-3: Current-voltage-light (L-I-V) characteristics of broad-area lasers from (a) V1183 wafer of dimension 100μm×2mm (b) V1184 wafer of width 100μm and 150μm (2mm long).

The output power from V1183 laser was ~189mW/facet (B, 100μm×2mm) after correcting for a 10% CaF_2 window loss. The values of this output power could be larger if the beam divergence loss is taken into account (30-40%). The slope efficiency was extracted as 0.47W/A (per facet) by linear fitting the I-L plot, and implies an external quantum efficiency as 2.86. The output power from V1184 laser was a very low value of ~24mW/facet even after correcting for the CaF_2 window loss (~10%), indicating a very poor external quantum efficiency (<0.12).

The pulsed L-I-V data were collected by using a LN cooled external InSb detector and the photocurrent generated from this detector was measured as shown in Figure 3-4.

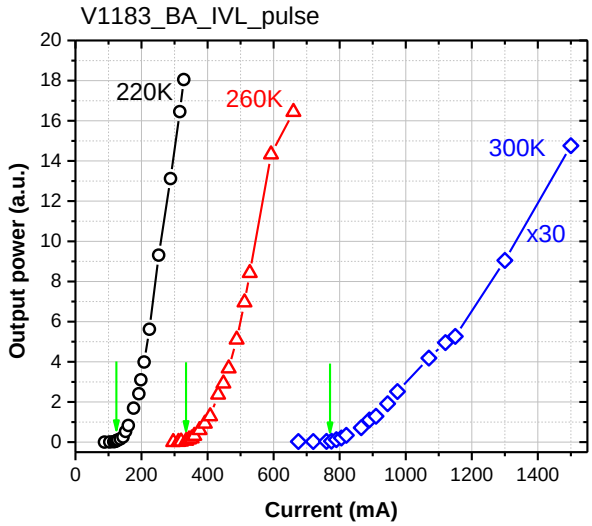

Figure 3-4: Pulsed L-I-V of a broad-area laser from wafer V1183 (10 stages).

This output photocurrent in pulsed mode is related to the output power coming from the laser. The pulse width of 1μs with a 0.5% duty cycle (5KHz) was applied to the laser from a AVTECH pulse generator. Note that the laser generates excessive heat in cw mode in the active region which limits the laser performance at higher operating temperature. Hence, a low duty cycle with short current pulse was typically applied to the laser to keep the heat generation in the active region to a minimum.

CW and pulsed spectra were taken for both of these lasers, as shown in Figure 3-5 and Figure 3-6. For the pulsed spectra measurement, a double modulation technique was used (this technique is helpful when the laser signal is very weak). In all calculations hence forth, the connecting wire resistances (~0.5Ω) were corrected for voltages in pulsed mode.

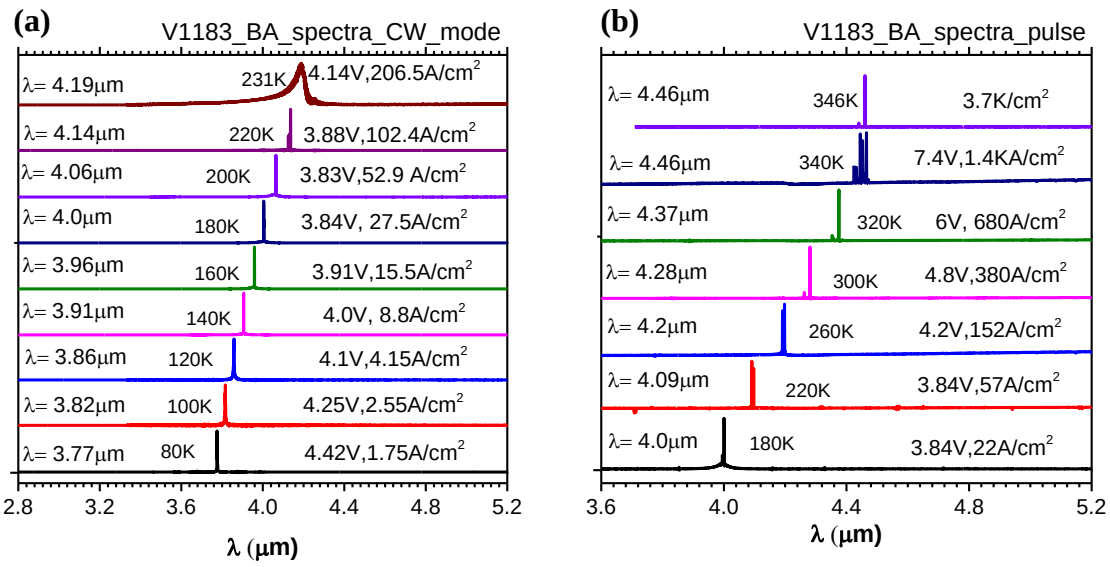

Figure 3-5: Broad-area laser spectra from the wafer V1183 (B, 100μm×2mm) in (a) cw mode and (b) pulsed mode.

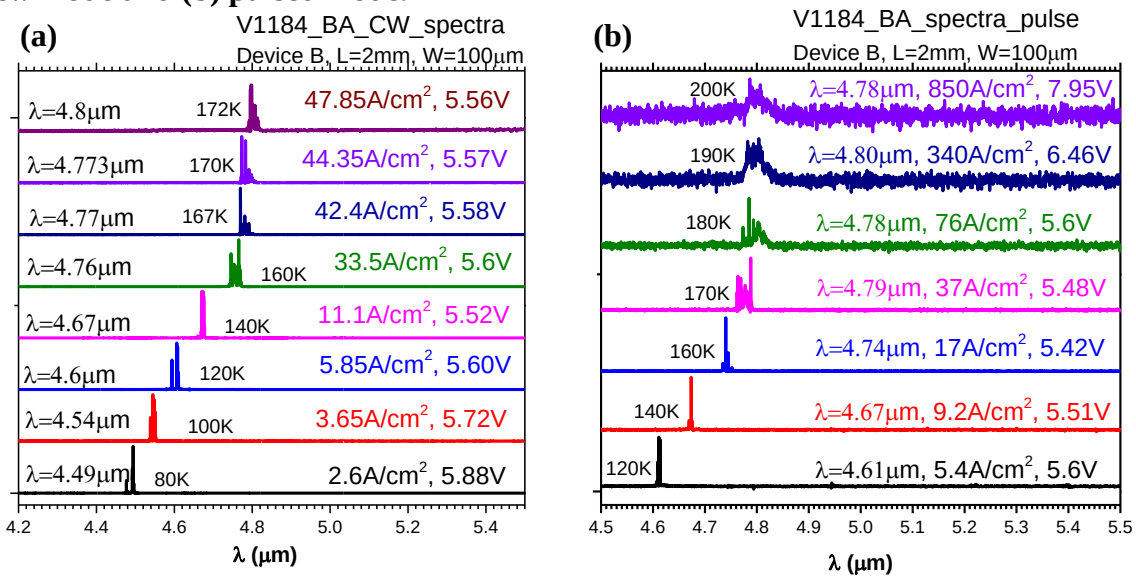

Figure 3-6: Broad-area laser spectra from the wafer V1184 (B, 100μm×2mm) in (a) cw mode and (b) pulsed mode.

One laser from wafer V1183 (B, 100μm) was able to lase at cw current mode at a heat-sink temperature up to 231K at a 4.19μm lasing wavelength. The threshold current density was found to be 206.5A/cm^2 with a threshold voltage of 4.14V. At 80K, the V1183 broad-area laser lased at a 3.7μm wavelength with a 1.75A/cm^2 threshold

current density (V_{th}= 4.42V). The threshold current density in pulse mode was 380A/cm^2 at 300K at 4.28μm wavelength.

The performance of the devices from 15 stage wafer V1184 was unstable and inferior. At the liquid nitrogen (LN) temperature, the 15 stage V1184 broad-area laser lased at a longer lasing wavelength of 4.49μm with a threshold current density and voltage of 2.6A/cm^2 and 5.88V, respectively. The highest cw operating temperature from this inferior wafer was 172K at 4.8μm with a 47.8A/cm^2 threshold current density and a 5.56V threshold voltage. In pulsed mode, the maximum operating temperature was 200K with a 850A/cm^2 threshold current density.

These two lasers demonstrated less than a 75% voltage efficiency (70% for V1184, and 74% for V1183 at 80K) which is much less than for our previous wafers of similar design. They exhibited a voltage efficiency of ~96% at 80K near 5.3μm lasing wavelength [82]. The access voltage needed for lasing may have dropped somewhere inside the structure. This may be related to carrier lifetime in the upper lasing state, non-radiative recombination or the existence of a leakage channel.

The lasing wavelength of these lasers shifted with temperature as seen in Figure 3-7. For V1183, the lasing wavelength red shifted at the rate of 2.78nm/K in cw mode and 2.77nm/K in pulsed mode. The lasing wavelength red shifted at the rate of 3.37nm/K in cw mode and 2.13nm/K in pulsed mode for the V1184 laser. There is a blue-shift of the lasing wavelength above 190K near the maximum operating temperature in the V1184 device which results from band filling effects when the maximum operating temperature is approached.

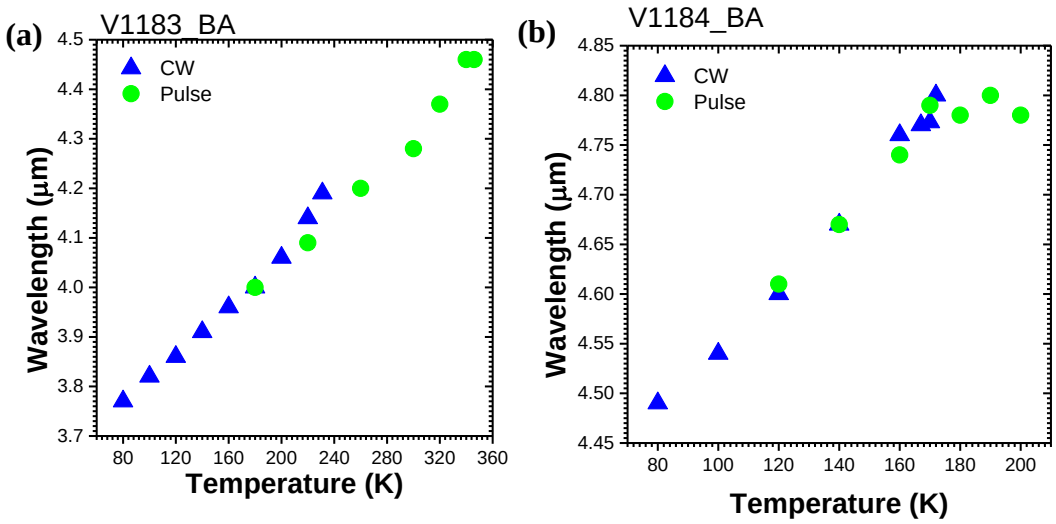

Figure 3-7: Temperature dependence of lasing wavelengths of lasers from the wafer (a) V1183 and (b) V1184.

The threshold current as a function of temperature of any laser is described by the following empirical relation:

$$J_{th} = J_o exp(\frac{T}{T_o}) \qquad (12)$$

where, T_o is called the characteristic temperature. T_o is an important parameter to measure the quality of the laser. It relates the sensitivity of the laser threshold current with temperature. The higher the characteristic temperature, the smaller the laser threshold current sensitive to temperature change. T_o can be extracted by fitting the J_{th} vs. T plot of Figure 3-8 by equation (12). The fitting was carried out by using *Origin-Lab* software and the characteristic temperature was estimated as ~31K for V1183 (120-220K range) in cw mode as shown in Figure 3-8 and ~43K (180-300K range) in pulsed mode for broad-area lasers. The fitting didn't converge for the V1184 laser due to the scattered data. The estimated T_0 value for V1183 laser is much lower than the state-of-the-art characteristic temperature (60K) in the neighborhood of 300K for GaSb based

ICLs in the 3-4μm wavelength region [15]. The lower T_o is another indication of the inferior performance of these lasers.

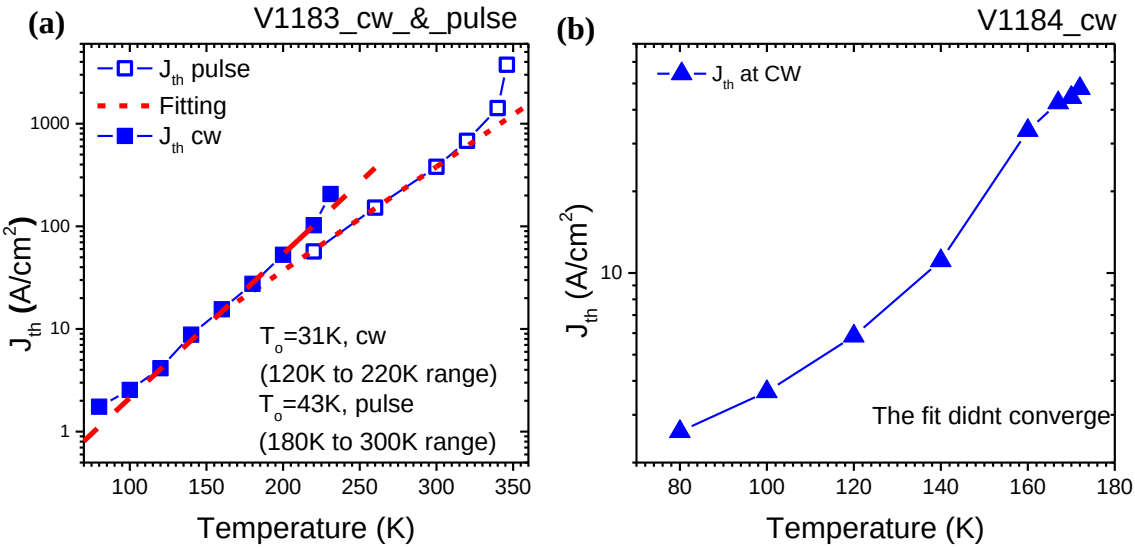

Figure 3-8: Characteristic temperature (T_o) of (a) the V1183 wafer at cw and pulsed modes and (b) J_{th} vs. T for the V1184 wafer where the fitting did not converge.

The thermal resistance of a laser is a measure of the quality of heat transport inside the laser structure as well the whole package including indium solder, and heat-sink. The thermal resistance of a broad-area laser (~100μm×2mm) from the wafer V1183 near maximum cw operating temperature (231K) was estimated as ~49.8K cm^2/kW. The thermal resistance of the wafer V1184 (broad-area lasers) was found to be ~46K cm^2/kW in the vicinity of 160K and presumably it would increase with temperature and would affect the laser performance. The state-of-the-art value of thermal resistance of a broad-area laser was not found in the literature in this wavelength region to compare with our experimental result.

The wall-plug efficiency is a measure of a semiconductor laser's power conversion efficiency. It tells us how much optical power is generated for a given input electrical power. The wall-plug efficiency was calculated from equation (13):

$$\eta_{wall\ plug} = \frac{2L}{VI} \tag{13}$$

where, L is the light output power per facet, and V and I are the voltage and current, respectively. The multiplying factor "2" in the above equation accounts for the two facets of the laser bar. The maximum wall-plug efficiency was ~10.78% for V1183 as shown in Figure 3-9. This wall-plug efficiency at 80K was smaller than the wall-plug efficiency of ~21% (at 80K) from our previous InAs based laser grown at OU which lased at 4.67μm [82]. The wall-plug efficiency of V1184 was found very small (~0.46%), which indicated poor power conversion efficiency and the possible existence of a leakage channel. Both of the wall-plug efficiencies were corrected by taking into account the 10% cryostat CaF_2 window loss. However, these values could be much higher if the beam divergence loss (30%~43%) is taken into account.

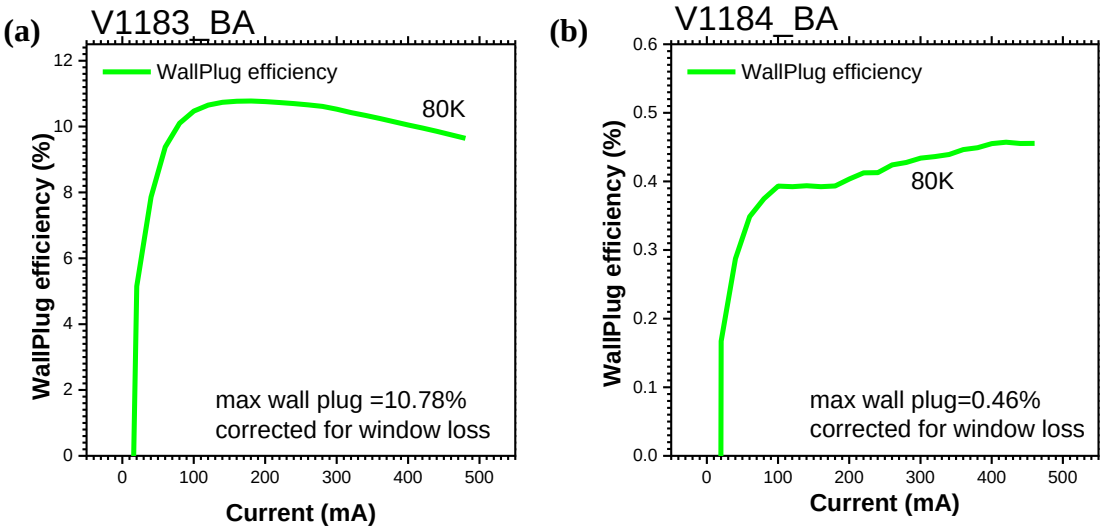

Figure 3-9: Wall-plug efficiency of a representative laser from the wafer (a) V1183 and (b) V1184.

The performance of the V1184 laser was unexpectedly inferior in terms of high temperature performance and threshold current density. To investigate this issue, we wanted to estimate the doping concentration of this laser to compare with the design value. In this regard, the doping concentration was estimated by using a *reflection measurement* of the laser wafer and the result is shown in Figure 3-10. The details of the *reflection measurement* can be found in [83]. The plasma frequency of the V1183 wafer was 1171cm^{-1}, which corresponds to a doping concentration of 1.26×10^{19}cm^{-3} (design value was 1.20×10^{19}cm^{-3}). There were two dips seen in the reflection measurement of V1184 that corresponds to 4.8×10^{18}cm^{-3} and 9.6×10^{18}cm^{-3} doping concentration (design 8.3×10^{18}cm^{-3}). It is worth mentioning that the reflection measurement could not determine the individual layer doping but rather estimates an overall gross doping concentration. We have found that the doping concentration of V1183 is reasonably close to the design value but the estimated doping concentration of V1184 has some discrepancy with the design value. In addition, we have seen two dips that correspond to two different doping concentrations.

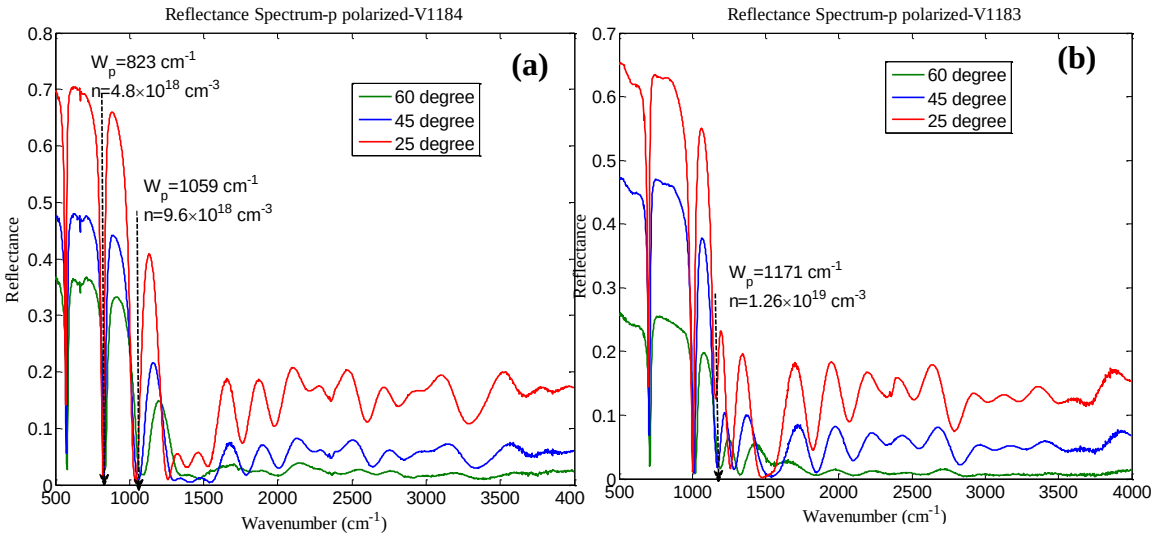

Figure 3-10: Reflection measurement of (a) V1183 and (b) 1184 laser.

■ Narrow-ridge laser performance

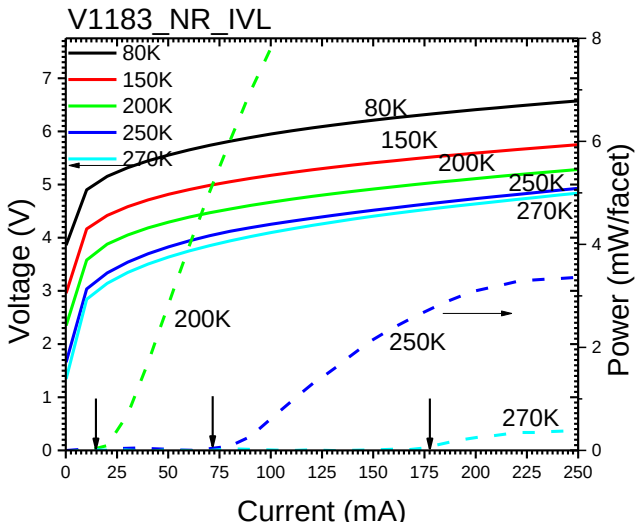

Figure 3-11: L-I-V from a narrow-ridge laser made from the wafer V1183.

The L-I-V characteristic of a narrow-ridge laser from the wafer V1183 is shown in Figure 3-11. The joule heating of this laser was substantial above 270K as reflected by the thermal rollover in the L-I-V plot of Figure 3-11. The thermal resistance was estimated as 8.85K cm^2/kW for a 9μm×2mm laser from the wafer V1183 which is similar than our previous InAs based lasers near 4.6μm [58]. The data from the wafer V1184 was not available because it was not processed into narrow-ridge devices due to the inferior performance as a broad-area laser.

The lasing spectra in both cw and pulsed mode are shown in Figure 3-12. The pulsed lasing spectra shown in this figure were obtained by applying a 1μs pulse with a 5KHz repetition rate. In cw mode, a narrow-ridge laser from the wafer V1183 operated at up to 284K with a 4.28μm lasing wavelength and a threshold current density of ~689A/cm^2. This laser lased up to 339K at a 4.27μm wavelength and a threshold current density of 3.53KA/cm^2 in pulsed mode as shown in Figure 3-12.

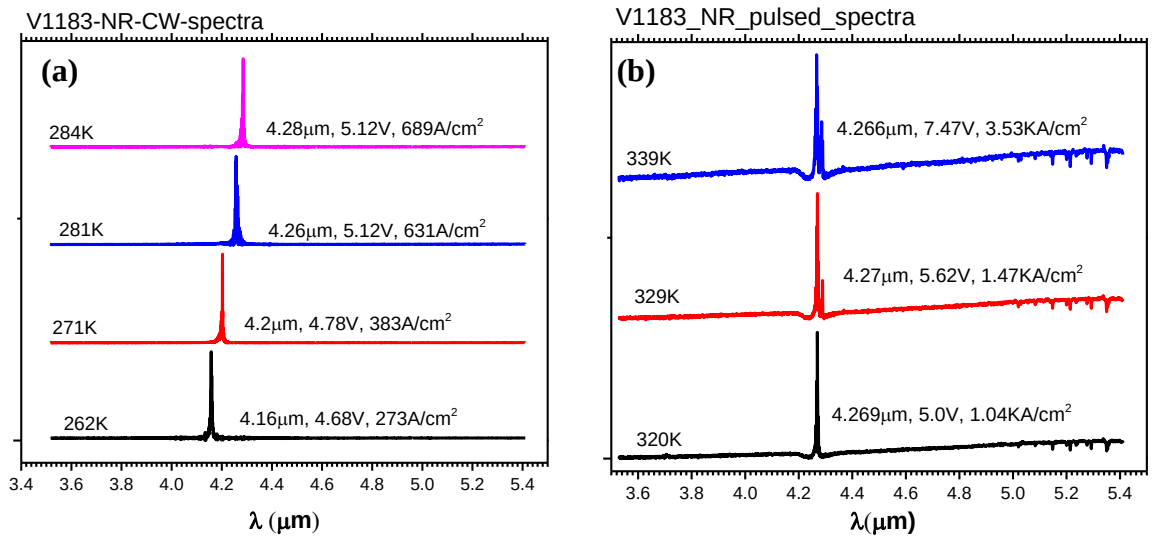

Figure 3-12: Lasing spectra of a narrow-ridge laser from V1183 in (a) cw and (b) pulsed modes.

The electroplated gold on top of the narrow-ridge laser was deposited from a degraded gold plating solution. The quality of the electroplated gold was inferior in terms of heat transfer as well as mechanical stress management. As a result of this inferior gold, the top layer along with the insulating layer and part of the substrate peeled-off during bonding and testing. This peeling off is visible in the SEM images shown in Figure 3-13. This figure indicates that the corners of the laser bar are peeled off and the thickness of the plated gold is not uniform.

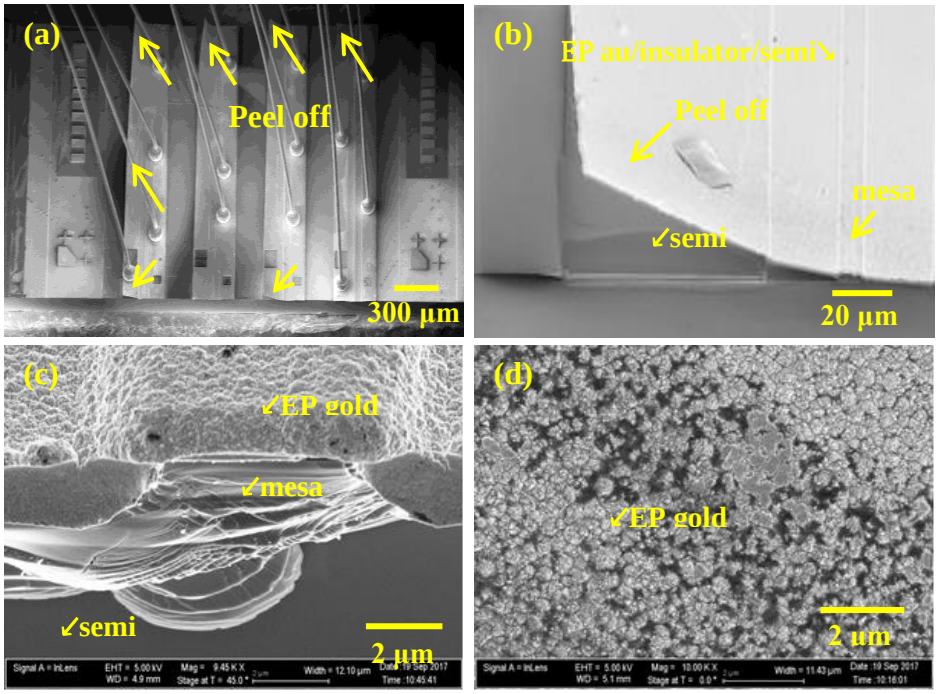

Figure 3-13: Scanning electron microscopy of a narrow-ridge laser from the wafer V1183. (a) peeling-off the gold layer, (b) peeling-off the corner of a laser, (c) mesa of a laser, and (d) textured gold layer.

In the second phase, three lasers were grown on an InAs substrate by the NRC, Canada. Two of these lasers have 10 cascade stages and are designed to lase near 4.6µm. The other laser has 15 stages and was designed to lase at a longer wavelength of 6.5µm, as will be described in a later section. The structures of the 10 stage lasers (V1189 and V1191) are the same except the doping concentration. The active region of is doped with silicon dopant at $2.8\times10^{18}cm^{-3}$ for V1189 and with $3.9\times10^{18}cm^{-3}$ for V1191 (~28% difference). It will be interesting to see the performance difference of these two lasers due to this doping difference.

■ Broad-area laser performance

The L-I-V characteristic curves from these two wafers are shown in Figure 3-14. V1189 exhibited a cw power of ~185mW/facet and V1191 exhibited ~200 mW/facet

from a 100μm laser (2mm long) at LN temperature. The value of the power was corrected for the 10% CaF_2 window loss. This value could be higher if the beam divergence loss is taken into account.

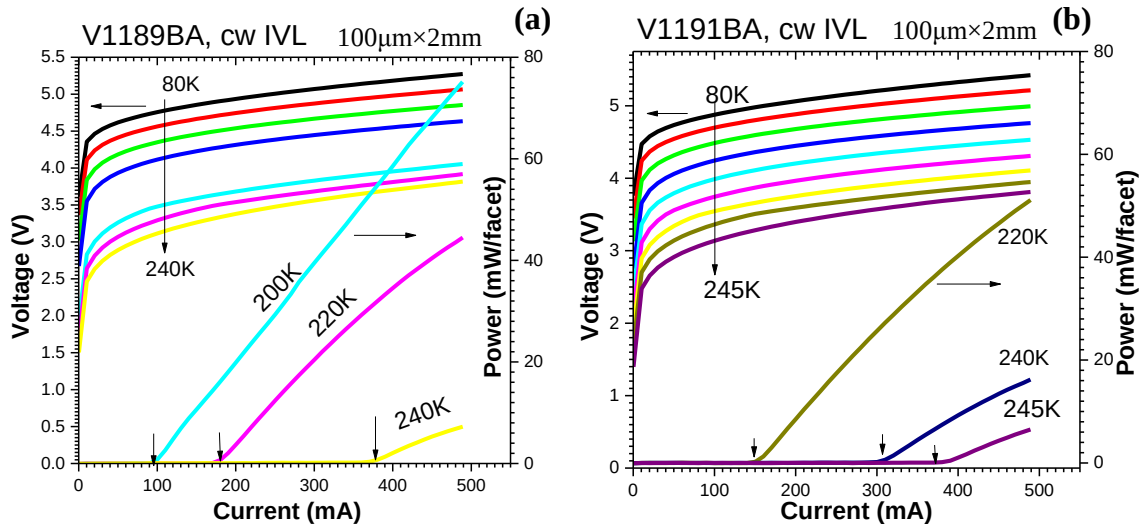

Figure 3-14: L-I-V characteristic of a broad-area laser from the (a) V1189 and (b) V1191 wafers. For both cases the cryostat window loss was corrected.

The slope efficiencies of these lasers were extracted from the cw L-I-V plot by linear fitting for both broad-area and narrow-ridge lasers and plotted in Figure 3-15. This figure shows that V1191, which has higher doping in the active region, exhibited ~10% steeper slope efficiency than V1189 for all operating temperatures. For example, V1191 exhibited a slope efficiency of 0.44W/A/facet, which corresponds to an external quantum efficiency (EQE) of 2.8. Similarly, V1189 has a slope efficiency of 0.40W/A/facet that corresponds to an EQE of 2.6. To investigate if there was any unwanted voltage drop across the device, we plotted voltage efficiencies from both broad-area and narrow-ridge lasers in Figure 3-15 (b). It is evident from this figure that V1191 has a better voltage efficiency than V1189 at higher temperatures that possibly resulted in higher output power and slope efficiency.

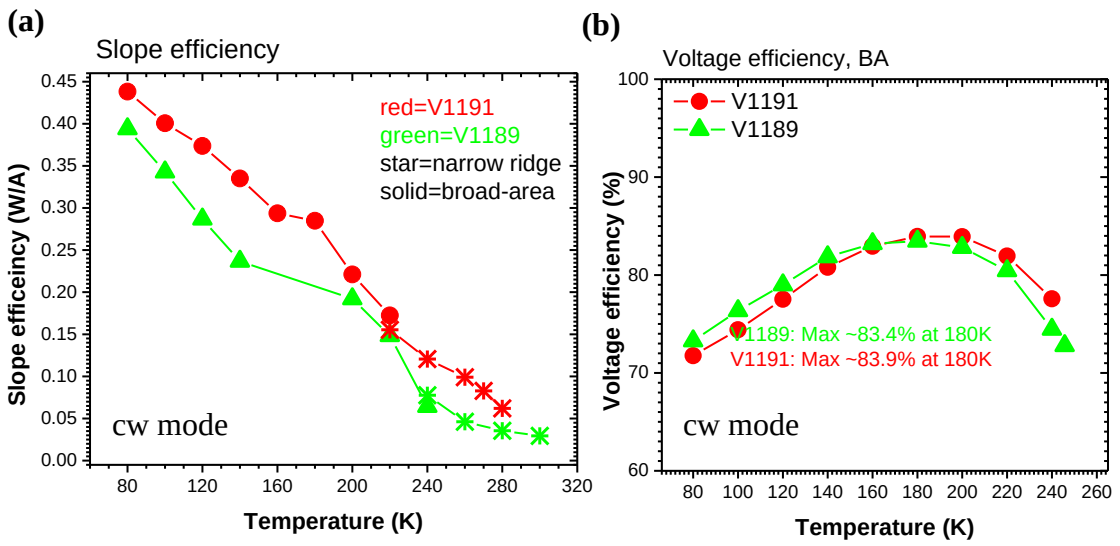

Figure 3-15: (a) Slope efficiency and (b) Voltage efficiency of two 10 stage lasers in cw mode.

Based on the slope efficiency shown in Figure 3-15 (a), we can comment that V1191, which has higher doping in active region, possibly can generate at least 10% (slope efficiency difference) more power than the lower doped V1189. In fact, V1191 generated ~7.5% more power than V1189 at 80K in cw mode according to the I-L plots.

The pulsed L-I-V characteristic plots are shown in Figure 3-16. A mid-IR sensitive MCT detector was placed in front of the laser and the change of the voltage based on the incident pulse power was recorded and plotted. It is evident from this plot that the lasers can generate power in pulsed mode at high temperature. A *conversion factor* can be determined to estimate this laser's power in pulsed mode.

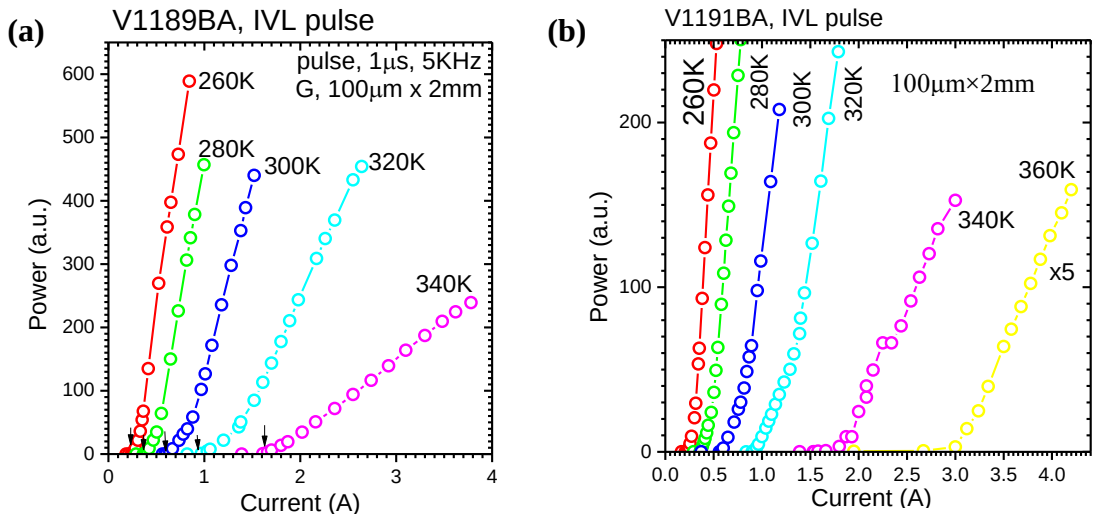

Figure 3-16: Relative pulse power of wafer (a) V1189 and (b) V1191.

The cw and pulse spectra of V1189 and V1191 broad-area lasers are shown in Figure 3-17 and Figure 3-18, respectively. The maximum cw operating temperature was obtained from a broad-area laser from the V1191 wafer which has higher doping concentration. One 100μm×2mm laser from this wafer lased up to 249K at a 4.52μm wavelength. The threshold current density was 288A/cm^2 with threshold voltage of 3.85V at this temperature. On the other hand, the maximum operating temperature of 243.5K at 4.58μm was obtained from a same size 100μm×2mm laser from V1189 with J_{th} of 229.4A/cm^2 and V_{th} of 3.72V.

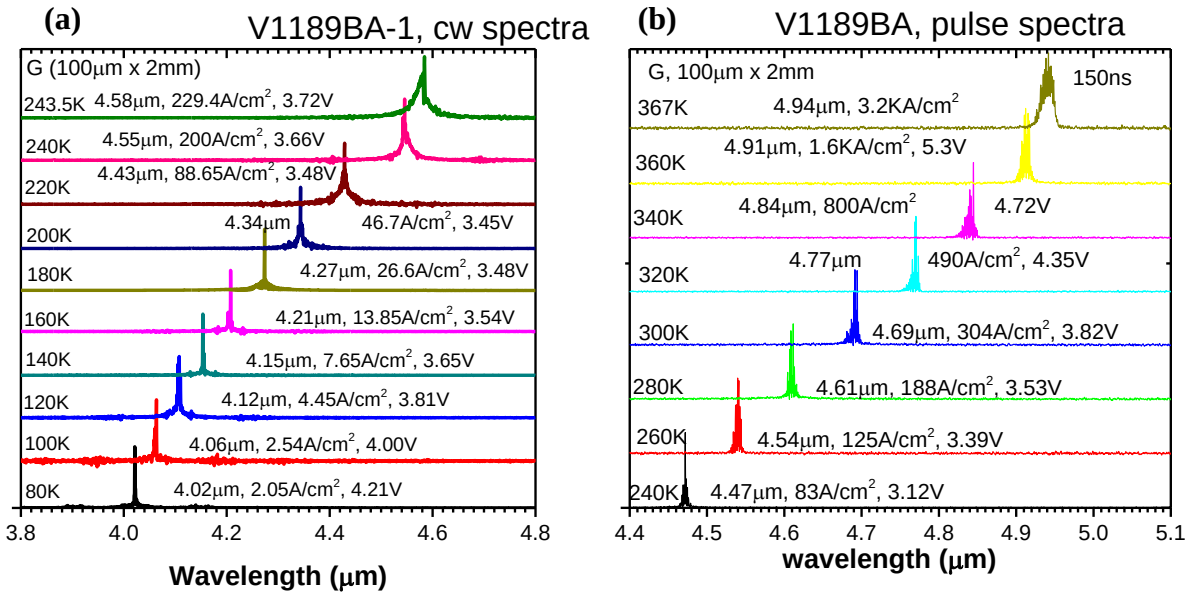

Figure 3-17: Broad-area laser spectra of V1189 in (a) cw and (b) pulsed modes.

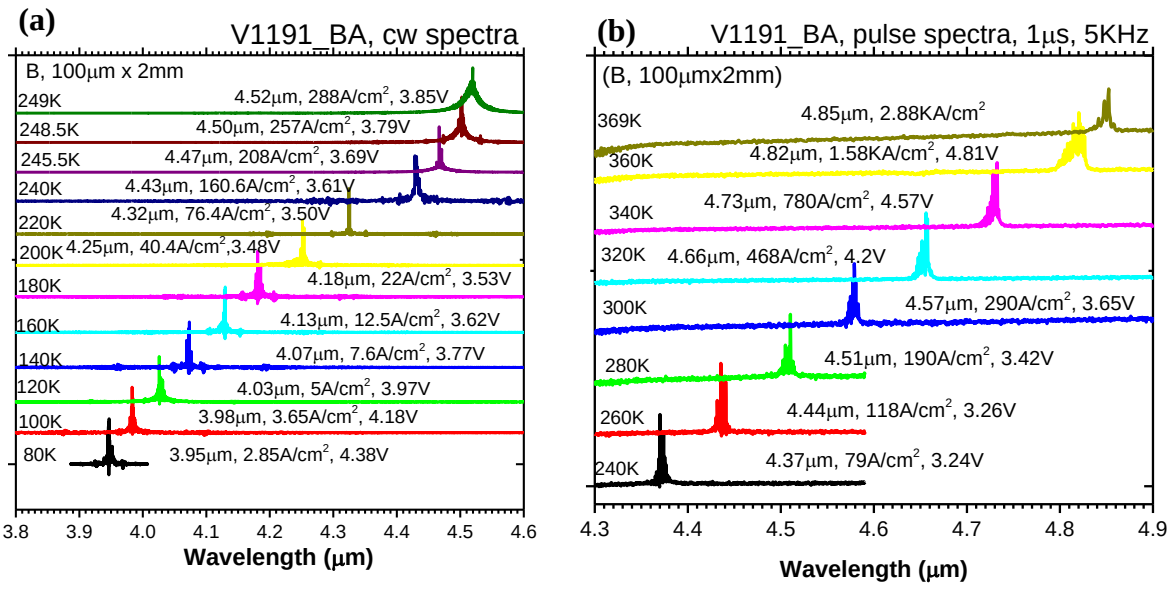

Figure 3-18: Broad-area laser spectra from the wafer V1191 in (a) cw and (b) pulsed mode.

In pulsed operation, broad-area (BA) lasers made from V1191 operated at a slightly higher maximum temperature of 369K than the BA lasers made from V1189 which operated at maximum of 367K. To eliminate the heating effect, at maximum

temperature, only 150ns of current pulse at 5KHz was applied. At 300K, the threshold current density was 304A/cm^2 near 4.69μm for V1189 and 290A/cm^2 near 4.57μm for V1191 which are less than 5% different. This value of threshold current density is ~20% higher than the state-of-the-art InAs lasers near 4.6μm [58].

The temperature dependence of the threshold current density and threshold voltage is plotted in Figure 3-19 for both devices. This figure shows that the threshold current density of broad-area lasers from these two wafers is comparable. However, at low temperature, the lasers from V1189 exhibited a lower threshold current density and higher voltage efficiency (see Figure 3-15 (b)).

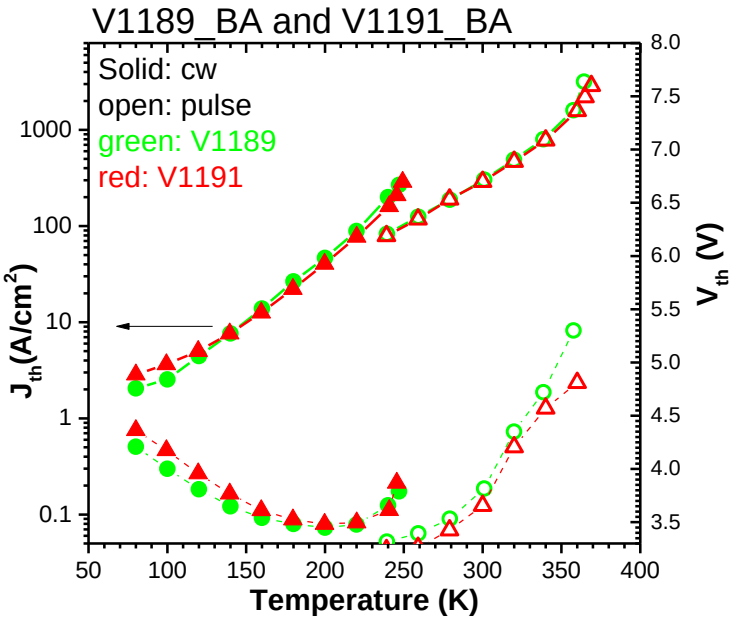

Figure 3-19: Threshold current density vs. heat-sink temperature of lasers from V1189 and V1191 (size, 100μm×2mm).

From this J_{th} vs. T plot, the characteristic temperature (T_o) can be extracted by fitting the equation (12). The fitting result of the characteristic temperature is shown in Figure 3-20. Both in cw and pulsed modes, it is evident from this figure that V1191 has a slightly better characteristic temperature compared to V1189. In the neighborhood of

300K, the characteristic temperature is ~44K for V1189 and ~44.69K for V1191, which are slightly lower than the state-of-the-art value of 46~57K at 4.6μm for InAs based ICLs [58] .

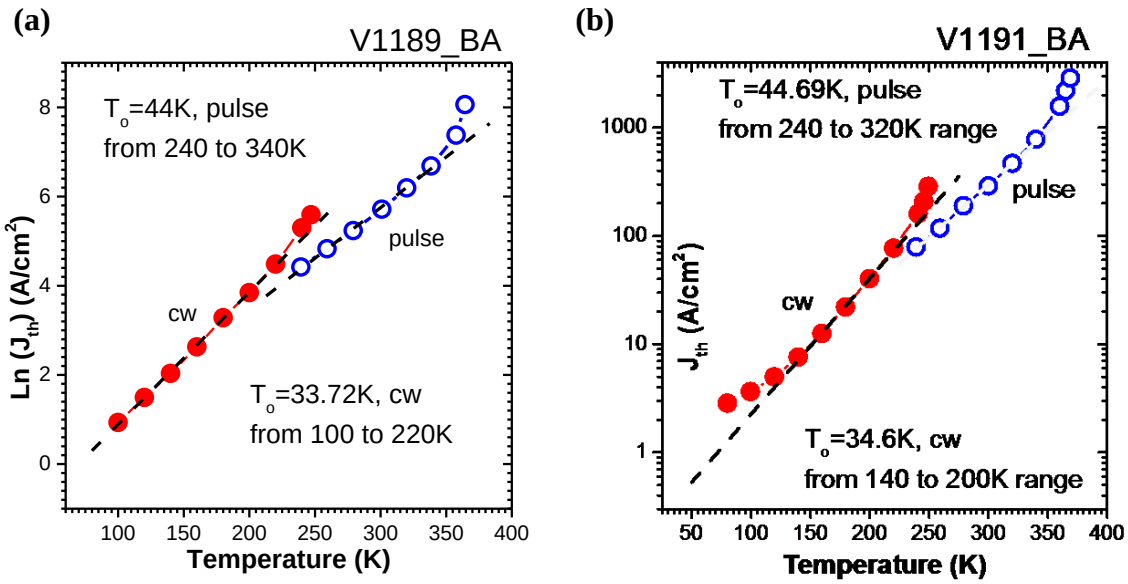

Figure 3-20: Characteristic temperature of lasers from (a) V1189 and (b) V1191.

The wall-plug efficiency was calculated for both lasers by using equation (13) at 80K and is shown in Figure 3-21. This efficiency was corrected for a 10% CaF_2 window loss without accounting the beam divergence loss. The maximum wall-plug efficiency obtained for V1191 and V1189 are 16.9% and 15.6%, respectively which are lower than the value of ~21% from a previous 5.3μm InAs based laser from our group [82].

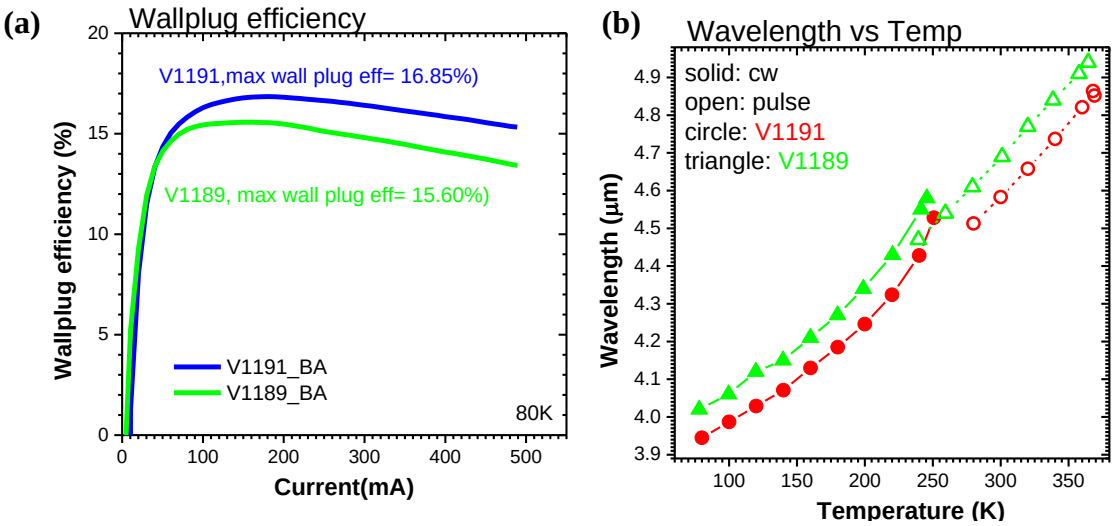

Figure 3-21: (a) Wall-plug efficiency at 80K and (b) change of wavelength with temperature of the lasers from V1189 and V1191 wafers.

The wavelength vs. temperature is plotted in Figure 3-21 (b) for both V1189 and V119 lasers. The lasing wavelength of V1189 was slightly longer than the lasing wavelength of V1191 although they were designed to lase at the same wavelength. This is attributed to MBE growth variation and non-uniform material quality. For V1189, the wavelength changes at a rate of 3.34nm/K in cw mode and 4.27nm/K in pulsed mode. This rate is 3.45nm/K in cw mode and 3.80nm/K in pulsed mode for the V1191 laser.

■ Narrow-ridge laser performance

To overcome the excessive heat generation issue of broad-area lasers, narrow-ridge lasers were fabricated in different sizes of nominally 10-, 12-, 15- and 20-μm (real size 7-, 9-, -12 and -17-μm by SEM). In addition, ~4μm of electroplated gold was deposited on top of the mesa to facilitate the heat removal process from the active region. The L-I-V characteristics of two representative lasers of size 9μm×2mm and 9μm×1.5mm are shown in Figure 3-22 at several heat-sink temperatures from V1189 and V1191 wafers, respectively. The joule heating in these lasers was substantial at

higher temperature as reflected by the thermal rollover, especially in Figure 3-22 (a) at 300K. Nevertheless, the output power of these lasers exceeded 2mW/facet without accounting for beam divergence loss near room temperature. The input power at threshold at 300K (cw) was 0.64W for V1189 and 0.57W for V1191, which are comparatively higher than the state-of-the-art GaSb ICLs in the 3-4μm wavelength region [15] and InAs based ICLs in 4.6μm wavelength of similar size [58].

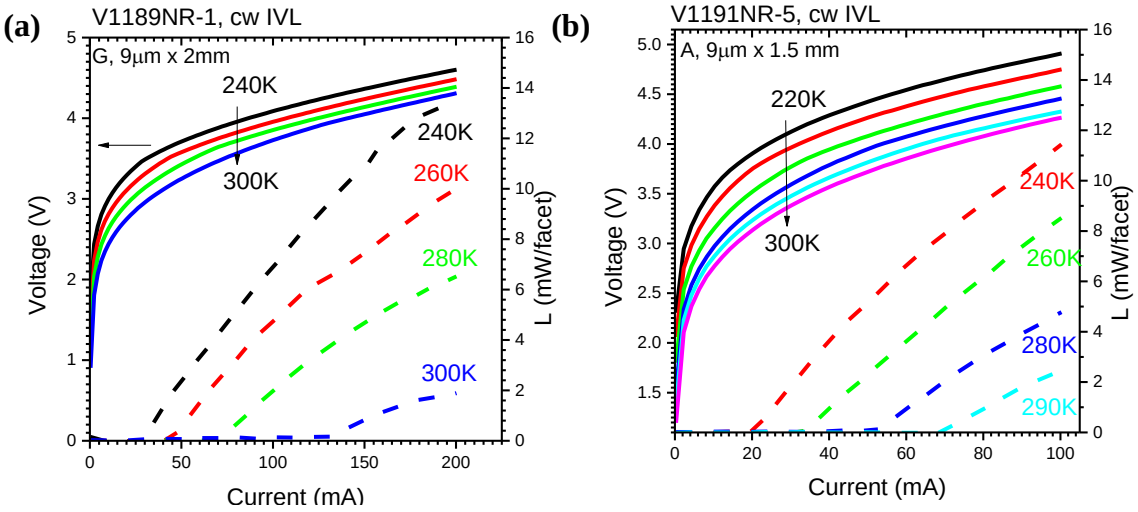

Figure 3-22: L-I-V characteristic of lasers from (a) V1189 and (b) V1191 wafers.

As mentioned, narrow-ridge lasers were designed to lase at higher temperature by better conducting heat from the active region through the ~4-6μm thick electroplated gold layer deposited on top of the mesa. This time a new gold plated solution was used. The lasing spectra of V1189 and V1191 lasers in both cw and pulsed modes are shown in Figure 3-23 and Figure 3-24, respectively.

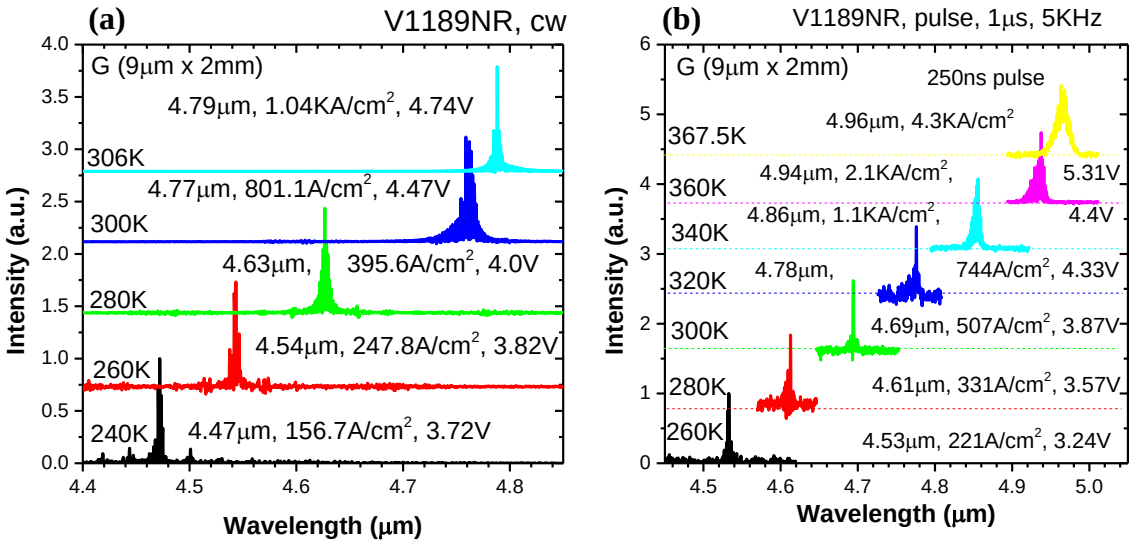

Figure 3-23: Lasing spectra of a narrow-ridge laser from the wafer V1189 in (a) cw and (b) pulsed mode.

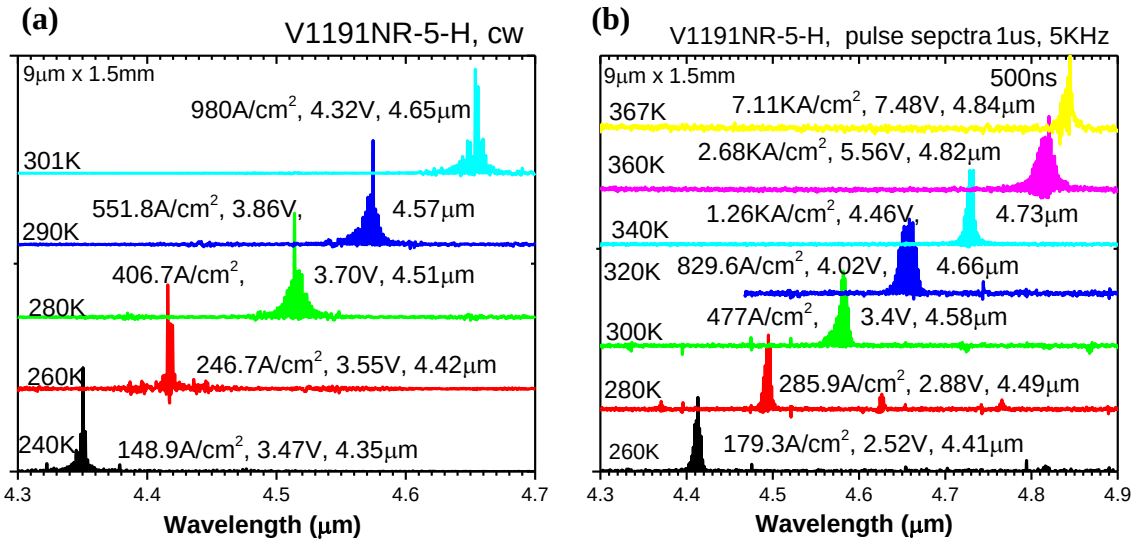

Figure 3-24: Lasing spectra of a narrow-ridge laser from the wafer V1191 in (a) cw and (b) pulsed modes.

One 9μm×2mm laser from the V1189 wafer lased at a 4.79μm wavelength at 306K in cw mode. The same laser lased at a 4.96μm wavelength at 367.5K in pulsed mode. The laser from the V1191 wafer (9μm×1.5mm) lased at a 4.65μm wavelength at 301K in cw mode and 4.84μm at 367K in pulsed mode. In 300K pulsed mode, V1189

had a threshold current density of 507A/cm^2 which is slightly higher (~6%) than the threshold current density of 477A/cm^2 for the V1191 laser (see Figure 3-24).

The threshold current density and corresponding voltage of narrow-ridge lasers from the V1189 and V1191 wafers are plotted in Figure 3-25 for comparison purpose. In part (b) of this figure, the corresponding voltage efficiency for both cw and pulse modes was calculated by using $V_{efficiency} = (N * \frac{1.24}{\lambda})/V_{th}$, where N is the number of stage, λ is the lasing wavelength in μm and V_{th} is the threshold voltage.

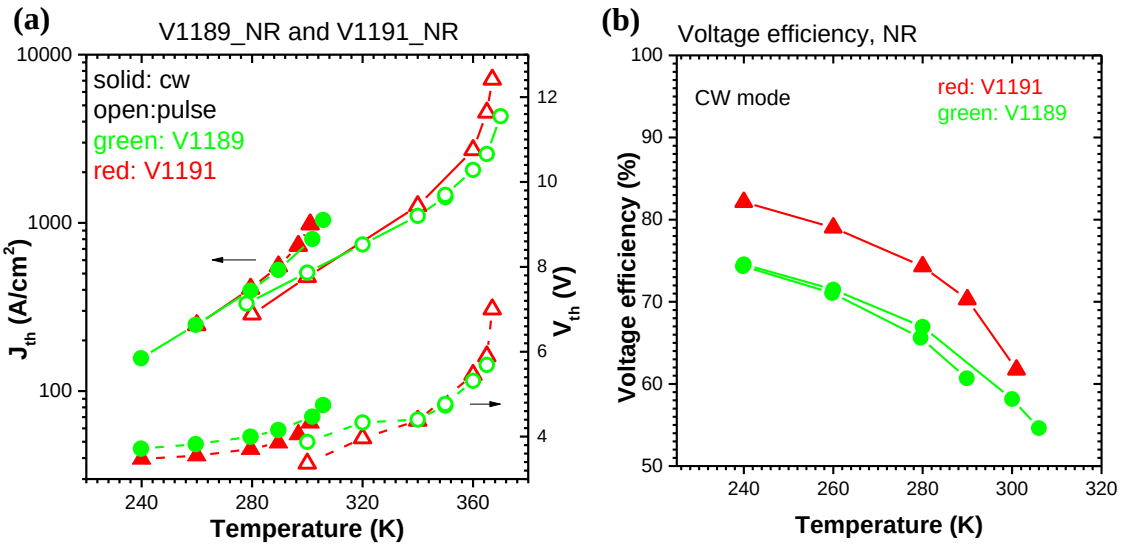

Figure 3-25: Comparison of the (a) current density vs. temperature and (b) voltage efficiency vs. temperature of a representative narrow-ridge laser.

It is evident from Figure 3-25 (a) that the threshold current density of the narrow-ridge laser from V1189 is lower than that of the V1191 lasers both in cw and pulsed mode. However, the lasers from V1191 exhibited a much better voltage efficiency as seen in Figure 3-25 (b). Actually the cw operation of V1191 was affected by its relatively higher thermal resistance. For example, the thermal resistance is in the range of 5.27~6.2K cm^2/kW for a 9μm laser from the V1189 wafer in the neighborhood

of 300K. The same size lasers exhibited a thermal resistance in the range of 6.6~10.5K cm^2/kW from V1191 wafer near the same temperature. The value of the specific thermal resistance is similar to values from our previous 4.6μm lasers of the same size, which was in the range of 6.5-11K cm^2/kW [58]. So we can comment that the maximum cw operation of V1191 was hampered by its higher thermal resistance because the maximum attainable operating temperature and output power are inversely proportional to the thermal resistance. These thermal properties can be improved by mounting the laser epi-side down.

To view all the properties of broad-area and narrow-ridge lasers, we plotted the threshold current density and voltage with respect to heat-sink temperature in Figure 3-26 for comparison. The pulsed threshold current density of a 9μm narrow-ridge laser (2 mm long) at 300K is 21% to 67% higher than their corresponding BA laser for the V1189 lasers. For the similar size laser (9μm×1.5mm) from the V1191 wafer, this difference is ~64%, which indicates the presence of significant current leakage from the sidewalls due to imperfect passivation.

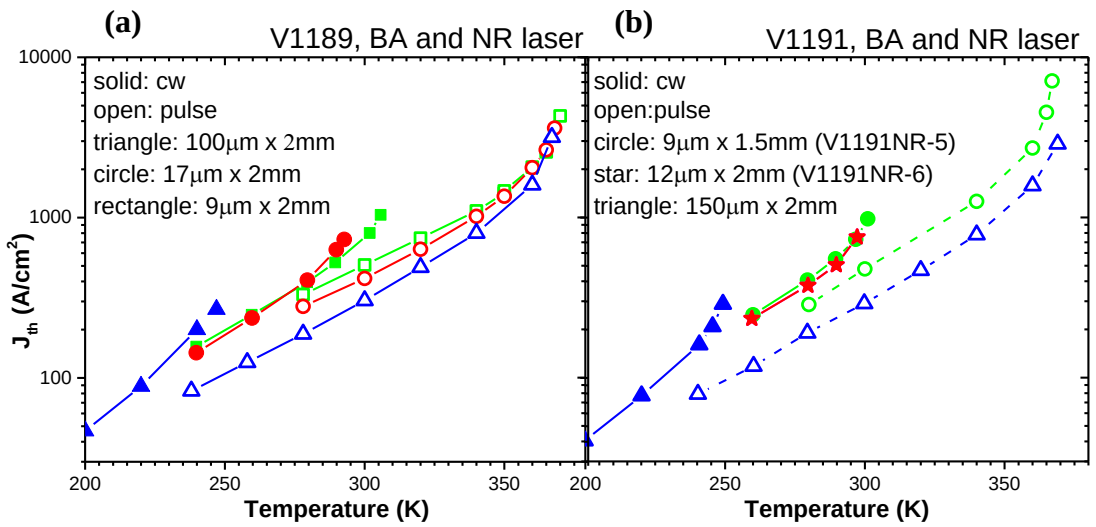

Figure 3-26: Threshold current density vs. heat-sink temperature of lasers from the wafer (a) V1189 and (b) V1191.

It was mentioned in previous sections that ICLs have been demonstrated beyond 6μm and up to 11μm by employing the plasmon waveguide design approach. However, room temperature operation in cw mode was not achieved in this range. In this regard, an ICL was designed using plasmon waveguide approach to lase above 6μm wavelength. The device structure was described as a representative laser in section 3.3 and the calculated band-edge diagram of one cascade stage and the layer sequence was shown in Figure 3-1.

Using the mentioned structure and layer sequence, a one-dimensional (1D) waveguide model based on the transfer matrix method was adopted to estimate the waveguide loss. The calculated optical mode profile and the refractive index profile along the growth direction of this 6μm laser are shown in Figure 3-27. The estimated internal loss due to free-carrier absorption is $\sim 6.6 cm^{-1}$. In this calculation, the values of the refractive indexes were collected from the values used by different groups and optical handbooks; however, the uncertainty in the results should be reasonably small.

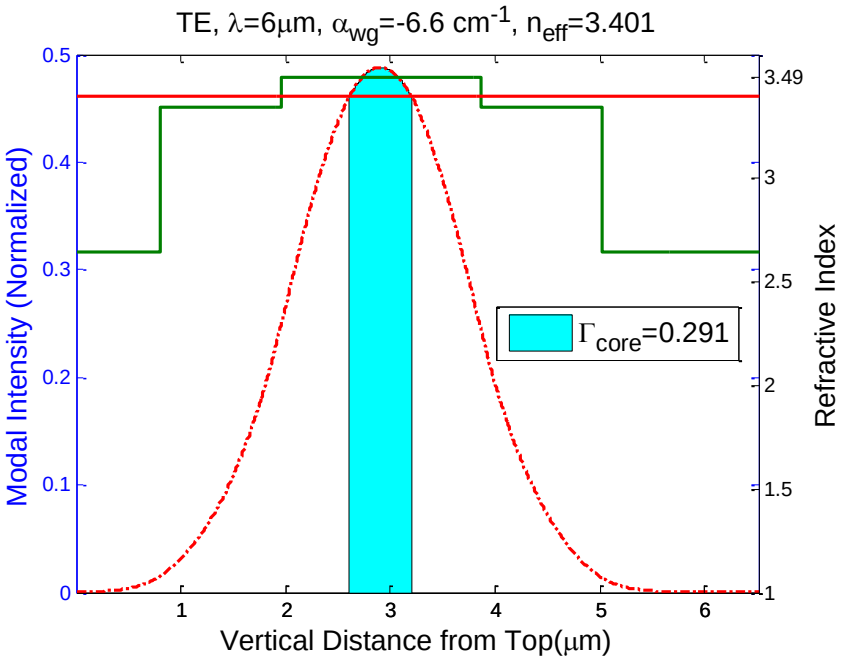

Figure 3-27: Optical mode and refractive index profiles along the growth direction of an InAs-based ICL with a plasmon cladding layer.

In the cw mode of operation, the broad-area laser lased up to 236K at a 5.8μm wavelength with a 194.3A/cm^2 threshold current density as shown in Figure 3-28 (a).

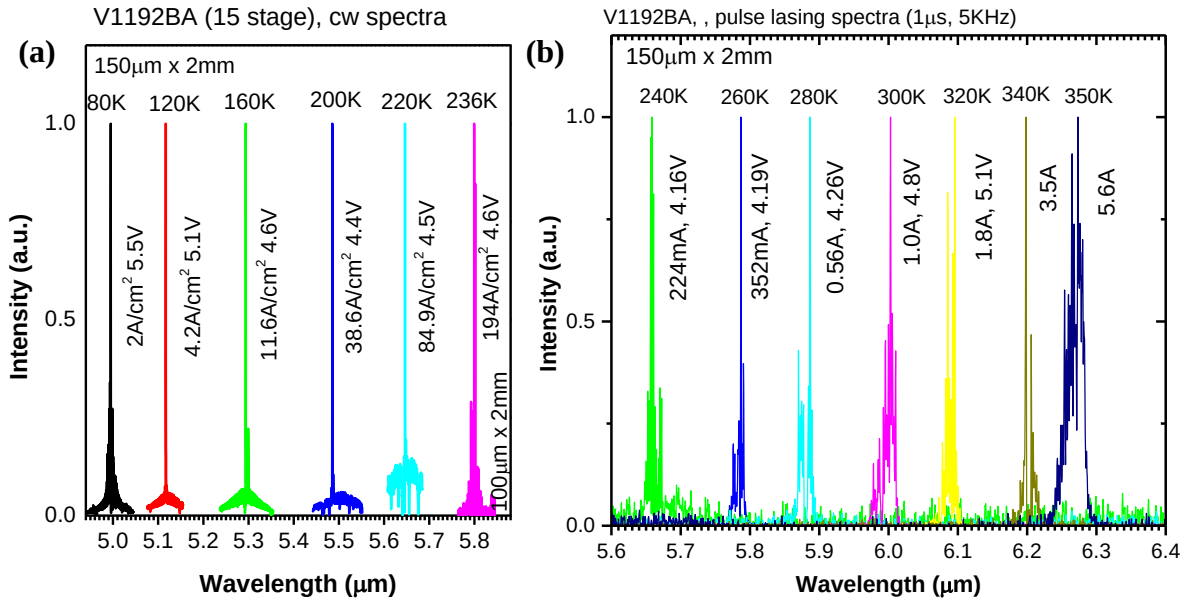

Figure 3-28: Near threshold lasing spectra of a representative 150μm wide broad-area laser at various temperatures in (a) cw and (b) pulsed modes.

In pulsed operation, BA devices made from this ICL wafer exhibited an emission wavelength above 6μm at 300K (Figure 3-28) with substantially lower threshold current densities compared to previously reported ICLs at similar wavelengths. For example, a 150μm wide device had a 300K (pulsed mode) threshold current density J_{th} of 333A/cm^2 at 6003nm with a threshold voltage of 4.8V. This corresponds to a threshold input power density of 1.6kW/cm^2 at 300K, the lowest ever reported among mid infrared semiconductor lasers at similar wavelengths. Compared to a state-of-the-art seven-stage GaSb-based ICL at 6μm with a threshold current density of 660A/cm^2 and threshold voltage of 3.41V [77, 84], J_{th} of this InAs-based ICL is reduced by about 50% with a higher voltage efficiency (64.6% versus 42.4%), and its threshold input power density is also lowered by 29% (1.6 versus 2.25kW/cm^2). This BA device lased in cw mode at temperatures up to ~230K and in pulsed mode at temperatures up to 350K (limited by the maximum available current) with the lasing wavelength red shifted from 5477nm at 200 K to 6273nm at 350K as shown in Figure 3-28. As shown in the inset to Figure 3-29, another 100μm wide device lased at temperatures up to 357K near 6.28μm, the highest operating temperature reported for electrically pumped interband lasers at this wavelength. In Figure 3-29, threshold current densities for several representative devices are plotted as a function of the heat-sink temperature. The characteristic temperature, T_0 (~38K in the neighborhood of 300K), is somewhat lower than that of state-of-the-art GaSb-based ICLs in the 3- to 4-

μm wavelength region [15].

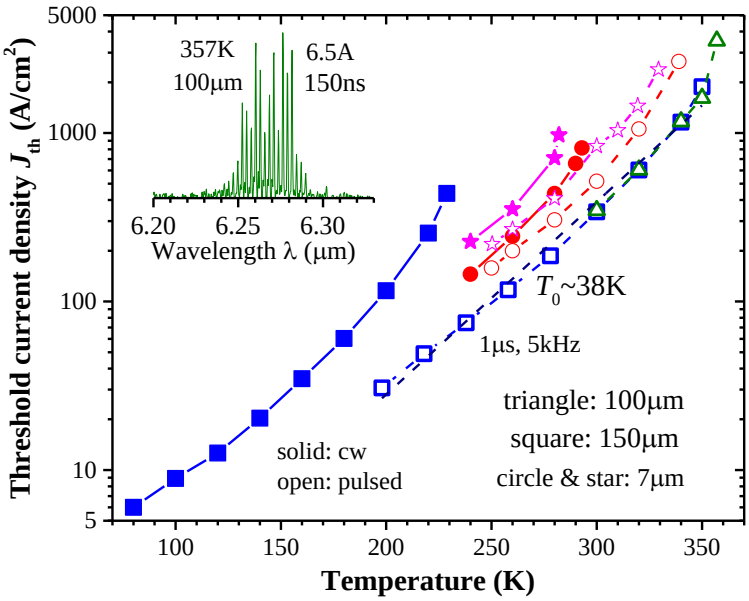

Figure 3-29: Threshold current density, J_{th} vs. heat-sink temperature, T, for both broad-area (BA) and narrow-ridge (NR) lasers. The inset is the pulsed lasing spectrum for a 100μm wide device at 357K.

NR devices with a top layer of ~4μm electroplated gold were able to lase in cw mode at higher temperatures than BA devices, as indicated in Figure 3-29. Due to isotropic etching with a wet chemical solution, the actual widths of the devices were narrower than defined by the mask set. For example, the nominal 10μm wide ridge device is actually about 7μm wide in the cascade region, as seen in SEM images (images not included here). Their threshold current densities were generally higher than corresponding values for BA lasers, as shown in Figure 3-29. Also, the threshold current densities of the NR lasers vary substantially from device to device as shown by the two 7μm wide NR devices in Figure 3-29, indicating large non-uniformities in device fabrication with the rough side wall surfaces due to wet etching. For example, at

300K, the pulsed threshold current density in 7μm wide NR devices was about 52% to 145% higher than that in a BA laser at the same cavity length. The difference is substantially higher than the ~34% difference reported for ICLs in the 3 to 4μm wavelength region [23] This suggests a somewhat significant current leakage from the sidewalls due to imperfect passivation, which implies further room to achieve better performance by reducing this surface leakage. Nevertheless, a 7μm wide NR device lased in cw mode at temperatures up to 293K at 6.01μm as shown in Figure 3-30. The detected output power exceeded 3mW/facet at 280K without accounting for beam divergence loss. The Joule heating in the laser was substantial at 293K, indicated by the thermal rollover in Figure 3-30. The input power at threshold was about 0.66W at 293K, which is higher than the state-of-the-art GaSb ICLs in the 3 to 4μm wavelength region [15] but this is still encouraging considering that the lasing was at a significantly longer wavelength. The cw operation of these NR ICLs was affected by their relatively high leakage current and a finite thermal resistance. By comparing threshold current densities in cw and pulsed modes, the specific thermal resistance for the 7μm wide ridge lasers was deduced to be in the range 4.4 to 4.6K cm^2/kW, which limited the maximum allowed cw threshold current density to below 1kA/cm^2, as shown in Figure 3-29. This suggests there is still room for improving thermal dissipation of these InAs-based ICLs even without employing epilayer down mounting.

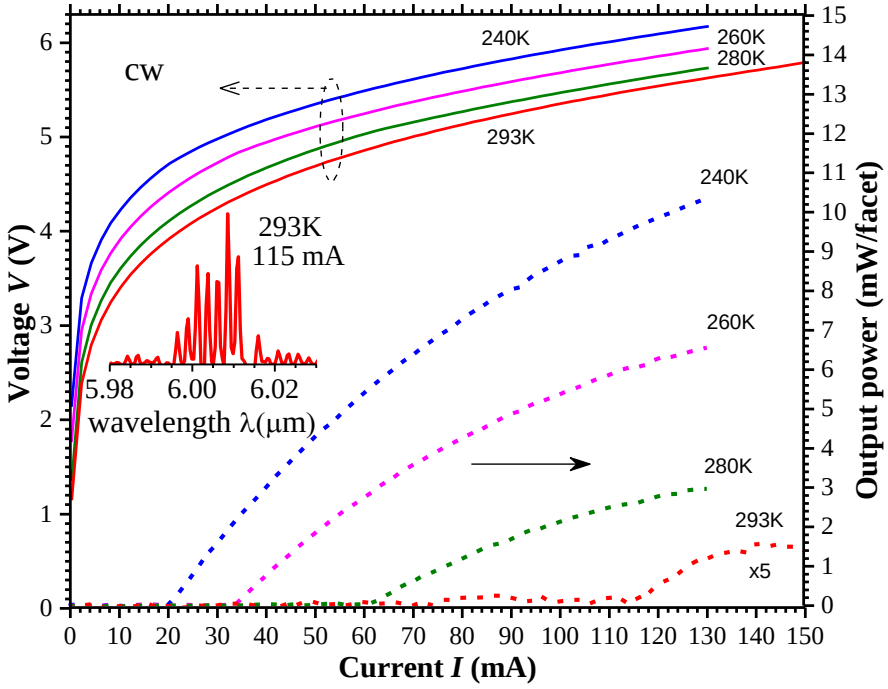

Figure 3-30: Current-voltage-light characteristics for a 7μm-wide, 2mm-long device in cw operation. The inset is the cw lasing spectrum at 293K.

The detail summary of the result of NRC lasers is given in Table 3-2.

Table 3-2: Performance summary of NRC lasers.

	V1183	**V1184**	**V1189**	**V1191**	**V1192**
Max operation, cw	284K @4.28μm	172K @4.80μm	306K @4.79μm	301K @4.65μm	293K @6.00μm
Max operation, pulse	346K @4.46μm	200K @4.78μm	367.5K @4.96μm	369K @4.85μm	357K @6.28μm
Lasing λ, 80K, cw	3.77μm	4.49μm	4.02μm	3.95μm	5.00μm
Lasing λ, 300K, pulse	4.28μm	4.78μm (200K)	4.69μm	4.57μm	6.01μm
Jth, 300K, pulse	380A/cm^2	850A/cm^2 (200K)	304A/cm^2	290A/cm^2	333A/cm^2
Power, 80K, cw	189mW/facet 100μm ×2mm	22mW/facet 150μm ×2mm	185mW/facet 100μm ×2mm	200mW/facet 100μm ×2mm	192mW/facet 150μm ×2mm
Voltage eff., 80K, cw	74.5%	70.36%	73.3%	72%	67.6%
Wall-plug eff., Max, cw	10.78%	0.46%	15.6%	16.85%	12.85%
Slope eff., 80K	0.47 W/A/facet	0.015 W/A/facet	0.40 W/A/facet	0.44 W/A/facet	0.46 W/A/facet
Characteristic temperature	~21.7K	-	~44K near 300K	~44.7K near 300K	~38K near 300K

3.5 Conclusion

In summary, InAs-based ICLs were demonstrated at emission wavelength beyond 6μm with a record low threshold current densities at 300K in pulsed mode. In addition, cw room temperature operation was obtained with a low input power consumption of 0.66W at the threshold. The thermal resistance of this laser was better than that of a GaSb based laser which indicates the advantage of using an InAs based substrate. However, the lasers near 4.6μm wavelength demonstrated higher thermal resistance which indicates room to improve thermal dissipation. All narrow-ridge lasers suffered from a substantial sidewall leakage current which leaves much room to improve both the fabrication and passivation techniques. Further advancements are expected with improvements in device fabrication (such as facet coating and dry etching). There is also room for optimization of device design, considering that there are many adjustable parameters, and this is still an early stage of development for this long wavelength spectrum.

Chapter 4: Far-field pattern and beam quality of ICL

4.1 Introduction

The performance characterization of a laser beam is fundamental to many scientific and industrial applications. A single longitudinal mode with a narrow line-width is required for high selectivity and sensitivity applications, especially in spectroscopy and laser-matter interaction. Hence, it is necessary to study the laser beam profile to understand and improve its quality. There are many figures of merits to characterize and analyze the quality of a laser beam such as the beam propagation quality factor, brightness, spot size, beam parameter product etc. A good beam can represent a well-designed waveguide and can, in some cases, indicate potential loss mechanisms inside the cavity. In this chapter, we will discuss the beam quality of three wafers which were processed in both broad-area and narrow-ridge geometries.

4.2 Type of laser beam profile

In the ideal case, the beam profile can be represented by a Gaussian beam. However, as it propagates through the narrow facet, the beam diffracts and becomes quasi Gaussian. This is analogous to light rays passing through a slit where the rectangular opening of the facet behaves as a slit. Immediately after the facet, the diffracted beam can be termed as “near-field” and away from the facet the projection of this near-field can be termed as “far-field” as shown in Figure 4-1.

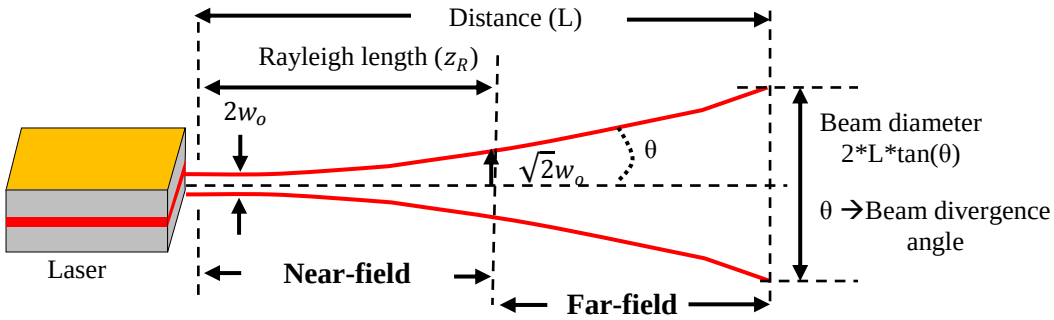

Figure 4-1: Typical laser beam with the near-field and far-field.

This is based on the Rayleigh length shown in Figure 4-1 which is the distance along the propagation direction of a beam from the waist to the place where the area of the cross section is doubled [85] and is defined by

$$z_R = \frac{\pi w_o^2}{\lambda}$$

where w_o is beam waist where the electric field falls down to $1/e^2$ (~13.5%) and λ is lasing wavelength. Rayleigh length determines the length over which the beam can propagate without diverging significantly. Based on this equation, the Rayleigh length of a typical ICL operating at 4.6μm or 6μm is about 1.3μm to 1.7μm, respectively.

An important parameter shown in Figure 4-1 is beam divergence angle (θ). The beam divergence of a laser beam is a measure for how fast the beam expands far from the beam waist and is defined by

$$\theta = \frac{\lambda}{\pi w_o}$$

4.2.1 Near-field

The near-field of a laser beam is located at a distance smaller than the Rayleigh length. For semiconductor lasers, this distance is very small, in the range of few microns, and is located close to the laser facet. As a result, a microscope and complex setup is often necessary to characterize the near-field beam profile. In our experiment, we mainly focused on far-field measurements. However, the near-field beam profile was calculated using the standard slab waveguide theory by our previous group member, the details of which can be found in his dissertation [61].

4.2.2 Far-field

The far-field is defined as the distance located more than the Raleigh length of the laser. This measures the angular spread of the laser beam both along the growth and lateral direction of the laser. The amount of spreading depends on the vertical and lateral guiding mechanism, refractive index contrast between the core and cladding, waveguide design, bias current, and heat generation. The far-field profile can be estimated by Fourier transforming the near-field. The laser facet is typically rectangular in shape which diffracts the light in different amounts and produces an elliptical far-field pattern. Based on the amount of diffraction, the laser far-field beam profile can be characterized along both the vertical as well as the growth directions.

- **Growth direction**

The active region width of the laser is very small in the growth direction compared to the lateral direction. As a result, the output beam diffracts very fast when propagating though this axis and hence this axis is often termed as the ‘fast axis’. The beam profile in this fast axis is always a single mode and diffraction limited. The

applied current of the laser does not affect the beam profile along this axis. The typical FWHM (full width half maximum) of a single mode beam of a diode laser in this direction is 15^o to 40^o [86]

- **Lateral direction**

Based on the design, the mesa stripe of an ICL can vary from tens of microns to hundreds of microns. Hence, the diffraction of light in this direction is small compared to the growth direction and is often termed as 'slow axis'. As the laser stripe is much wider than the wavelength of the laser, this direction can support a multimode laser output. The beam divergence along this axis changes with applied bias current. The typical FWHM of beam profile of a diode laser in this direction is 6^o to 12^o [86] .

4.3 Figures of merit

There are limited standard established models available to fully characterize the laser beam profile, however, beam divergence angle, beam quality factor, beam parameter product, brightness, spot size etc. are widely used to measure the quality of a laser beam. Essentially, how tightly a laser beam can be focused under certain conditions is the most important quality of any semiconductor laser. Some of these figures-of-merits are briefly discussed in next few sections.

4.3.1 Beam quality factor (M^2)

The beam quality factor is widely used to characterize the quality of a laser beam. This factor actually compares any laser beam to a pure Gaussian beam. Hence, the beam quality factor can be defined as the ratio of half-divergence angle of the laser beam to that of a pure Gaussian beam. Mathematically, the M^2 factor can be written as follows:

$$M^2 = \frac{Laser\ beam\ waist\ \times\ divergence\ angle}{Gaussian\ beam\ waist\ \times\ divergence\ angle} = \frac{w\,\theta}{w_o\theta_o} = \frac{\pi}{\lambda} w\theta$$

where w is the beam waist diameter, λ is the laser wavelength and θ is the divergence angle.

The value of this beam quality factor is equal to unity for a pure Gaussian beam. Actually, it's a measure about how much a laser beam deviates from a pure Gaussian beam. For example, M^2=1.5 means a laser beam cannot be focused down to a spot less than 1.5 times the focal spot diameter of a diffraction limited beam having M^2=1. Typically, for near-field, this value is close to unity but for far-field this quality factor becomes very high.

4.3.2 Brightness

The brightness of the laser is defined as the power emitted per unit surface area per unit solid angle. Higher brightness means better beam quality. A laser emitting power P with a circular beam cross section of diameter D and beam divergence angle θ will have brightness as follows:

$$B = \frac{4P}{(\pi D\theta)^2}$$

4.3.3 Spotsize

The spotsize of a laser beam is actually the radius of the irradiance profile. A lower spot size indicates good focusibility of the laser beam. The beam diameter is defined as the point where the maximum beam intensity falls by $1/e^2$, or 13.5%, of its maximum value. The spotsize is then defined as the radial distance from the center point of the maximum intensity to this $1/e^2$ point. We often calculate the beam diameter by this method which is illustrated in Figure 4-2:

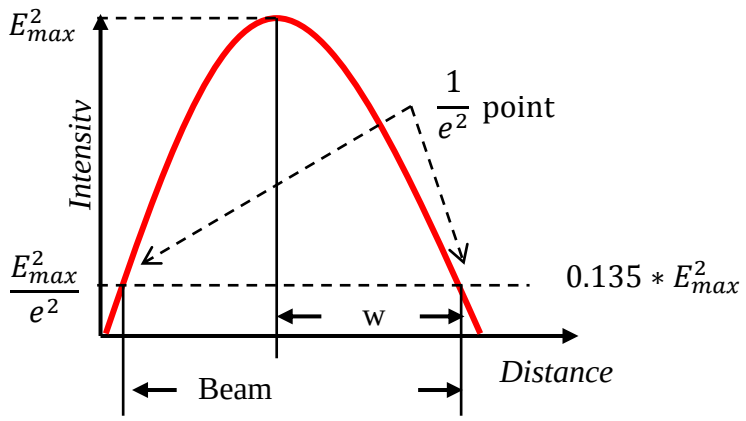

Figure 4-2: Definition of beam diameter of a Gaussian beam.

4.3.4 Beam parameter product (BPP)

The BPP is defined as the product of a laser beam's half divergence angle to the radius of its minimum beam waist. This paratermer quantifies the ability of a laser to focus on a small spot. The smallest possible beam parameter that can be achieved using a pure Gaussian beam is λ/π [87].

4.3.5 Gaussian function

The propagation of a laser beam can be approximated by assssuming that the beam has an ideal Gaussian intensity profile. The Gaussian function can explain the basic TE mode of the laser beam. Unfortunately, the true laser beam, especially for semiconductor lasers, is not Gaussian and diverges rapidly based on operating condtions. To accommodate this variance, the beam quality factor M^2 is defined and inserted into the Gaussian equation set given in subsequent sections.

Mathematically, the expression for the electric field of a laser is a solution of the Paraxial Helmholtz equation [88]. A Gaussian beam can be descrbed in terms of this electric field intensity by the following set of equations. In these equations the polarization direction is assumed to be in x-direction and the beam prapagation direction in the z-direction. Furthermore, the imaginary part of the equation is excluded to avoid complexity.

$$E(r,z) = E_o\hat{x}\frac{w_o}{w(z)}\exp(\frac{-r^2}{w(z)^2}) \tag{14}$$

$$w(z) = w_o\sqrt{1+\left(\frac{M^2 z}{z_R}\right)^2} \tag{15}$$

$$R(z) = z\left[1+\left(\frac{z_R}{M^2 z}\right)^2\right] \tag{16}$$

$$I(r,z) = I_o(z)exp\left(\frac{-r^2}{w(z)^2}\right) \tag{17}$$

where,

r is the radial distance from the center axis of the beam,

z is the axial distance from the beams's waist,

w(z) is the beam waist radius,

w_o is the radius at which the intensity falls to $1/e^2$,

$z_R = \frac{\pi w_o^2}{M^2\lambda}$ is called Rayleigh range, and

M^2 is the beam quality factor.

Figure 4-3 sketches a typical laser output with a Gaussian beam intensity profile both in the near and far-field. The property of a Gaussian beam is that it does not diverse linearly. As seen in Figure 4-3, the divergence angle at the beam waist is

extremely small. As the beam propagates, this divergence angle begins to follow the asymptotic cone. At z=0 and ∞ the wave front is planer as R(z) approaches infinity that means that the wave front curvature should increase to a maximum and then begin to decrease. The maximum curvature will occur at the Raleigh length position as shown in Figure 4-3. Note that the radius of the beam, w(z), at any position along the z direction can be related to full width half max according to $w(z) = \frac{FWHM(z)}{\sqrt{2ln2}}$.

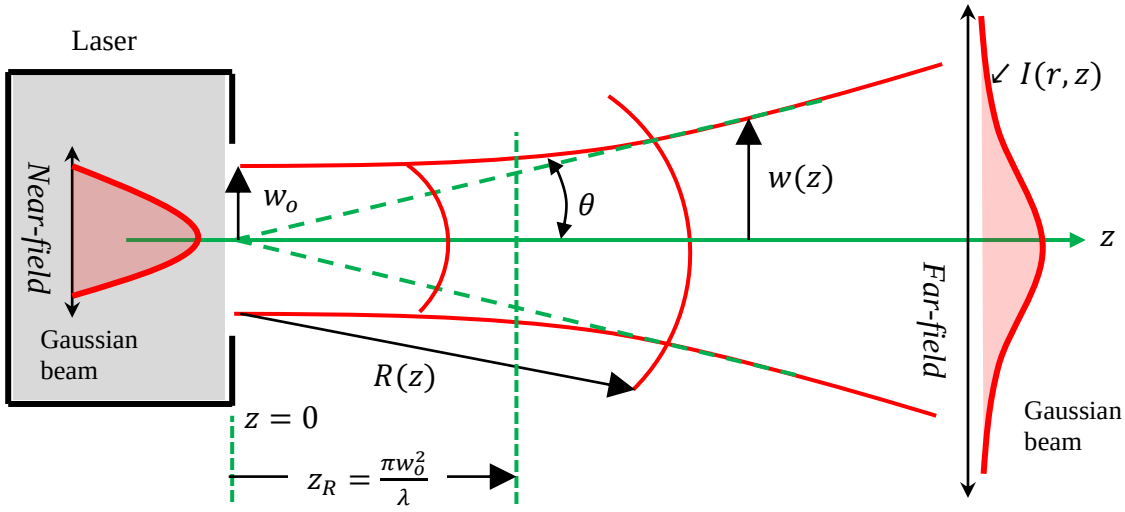

Figure 4-3: Sketch of beam profiles in near-field and far-field.

4.4 Near-field and far-field beam profile simulation

The ICL laser structure is a planner waveguide with a varying refractive index. The core of the laser has a higher refractive index than the cladding and substrate layer. As a result, the guiding of the laser beam is based on total internal reflection inside the laser waveguide. According to the slab waveguide theory, the electromagnetic field inside of a laser waveguide is a solution of Maxwell's wave equation [89]:

$$\nabla^2 \boldsymbol{E}(\boldsymbol{r},t) = \left[\frac{n^2(r)}{c^2}\right]\frac{\partial^2 \boldsymbol{E}(\boldsymbol{r},t)}{\partial t^2} \tag{18}$$

where $\boldsymbol{E}$ is the electric field vector, $\boldsymbol{r}$ is the radius vector, $n(\boldsymbol{r})$ is the index of refraction, and c is the speed of light in a vacuum.

For monochromatic waves, the solutions of this equation (18) have the form,

$$\boldsymbol{E}(\boldsymbol{r},t) = \boldsymbol{E}(\boldsymbol{r})e^{i\omega t} \tag{19}$$

where ω is the radian frequency. Substituting equation (19) into (18), we obtain,

$$\nabla^2 \boldsymbol{E}(\boldsymbol{r},t) + k^2 n^2(\boldsymbol{r})\boldsymbol{E}(\boldsymbol{r}) = 0 \tag{20}$$

where $k = {}^{w}/_{c}$. By solving this equation (20) with appropriate boundary conditions at the guide walls, the TE and TM mode can be found. In our case, the transfer matrix method was used to find the solution by our previous graduate student Dr. Yuchao Jiang. The calculated near-field intensity profile of a laser used in this experiment is given in Figure 4-4.

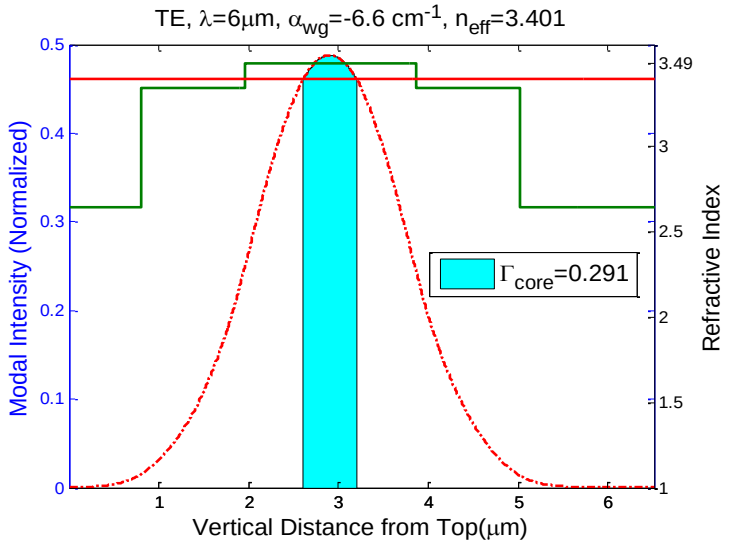

Figure 4-4: Near-field intensity profile of a 6μm laser (wafer V1192).

The far-field pattern can be obtained by Fourier transforming the near-field pattern [90]

$$I\,(x,y,z) = \left(\frac{I}{\lambda z}\right)^2 \left| \iint E(x',\,y') e^{\left\{-\frac{i2\pi}{\lambda z}(xx'+yy')\right\}} dx'dy' \right|^2 \tag{21}$$

where $I\,(x,y,z)$ is the intensity at far-field and $E(x',y')$ is the amplitude of the near-field electric field. However, the semiconductor surface modifies the far-field pattern and gives rise to a special obliquity factor. The origin of this obliquity factor can be explained by Huygen's radiation pattern. According to this theory, any small aperture has a radiation pattern which is dependent on the obliquity and the far-field pattern has to be multiplied by this obliquity factor [91]. Hence, the far-field pattern of a semiconductor laser can simply be written as:

$$I_{far} = O_{TE}(\theta)|E(\theta)|^2 \tag{22}$$

where

$$E(\theta) \propto \int_{-\infty}^{\infty} E_z e^{-ik_o z \sin\theta} dy \tag{23}$$

$$O_{TE}(\theta) = \cos^2\theta \left| \frac{1+\sqrt{n^2-\sin^2\theta}}{\cos\theta+\sqrt{n^2-\sin^2\theta}} \right|^2 \tag{24}$$

where *n* is the effective refractive index of the waveguide. The simulated far-field pattern by using Equation (22) for an ICL is shown in Figure 4-5:

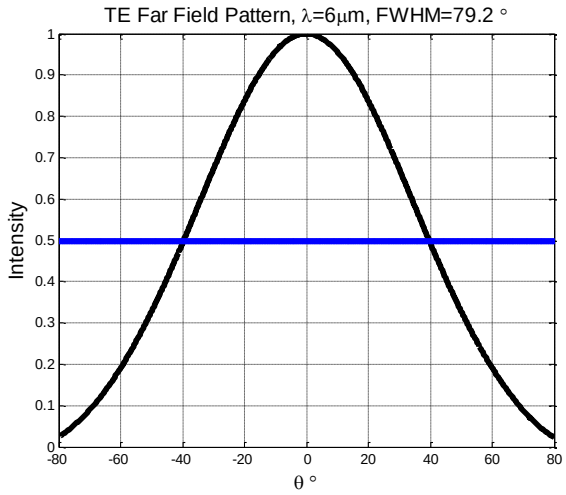

Figure 4-5: Simulated far-field intensity profile of a 6μm laser.

4.5 Experimental setup

The far-field beam profile characterization is comparatively easier than the near-field characterization due to its simple experimental setup. This setup needed an infrared detector placed more than the Rayleigh length from the laser facet to detect the signal. A MCT detector from Teledyne Judson Technologies with a 12μm cutoff frequency was used in this purpose. The signal from the ICL was very weak, hence a Lock-in amplifier was used to retrieve the weak signal. The detected signal from lock-in was then recorded and plotted using *Origin Lab* software for further analysis. The diagram of the experimental setup along with an original image is shown in Figure 4-6:

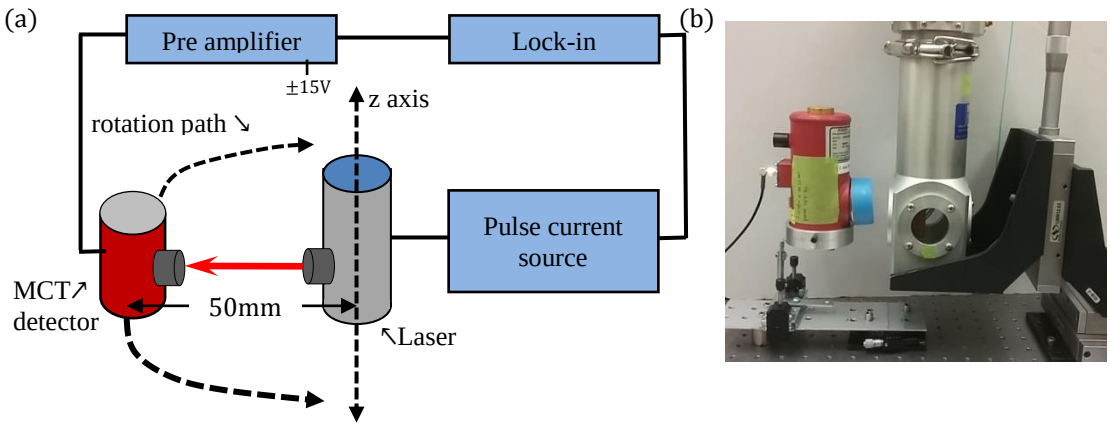

Figure 4-6: (a) Schematic of the far-field experimental setup, (b) original setup.

As mentioned in an earlier section, the distance between the laser and the detector should be more than the Rayleigh length. In our case, the Rayleigh length was calculated to be less than 2μm hence the detector could be placed anywhere more than this distance. We placed the detector at 50mm away from the laser. This distance was chosen so that the maximum rotation of ±30^{o} would then be possible for the detector stage to rotate freely around the laser. Furthermore, the signal output from the detector at this distance was found repeatable and reasonable.

The beam profile along the growth direction was obtained by rotating the detector around the laser cryostat until the detector stage had no room to rotate further in our setup. The Lateral beam profile was obtained by moving the vertical z axis of the laser cryostat at least ±30mm from the center of the detector. Due to the limitation of the setup, it was not possible to rotate the MCT detector in the vertical direction to obtain the lateral beam profile. However, the Cartesian coordinates were converted into Spherical coordinates by considering the laser and detector in the x-y plane and also the beam was corrected for this field of view according to [32] as shown in Figure 4-7.

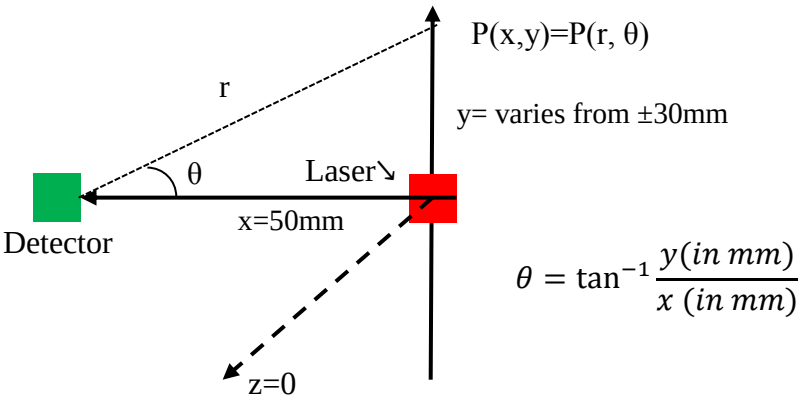

Figure 4-7: Cartesian to Spherical coordinate change for the lateral beam profile.

The center of the laser and the center of the rotational stage were aligned to make them concentric. Any misalignment may distort the beam shape and can cause errors in calculating the beam diameter.

4.6 Results and discussion

In this far-field beam profile experiment, around 30 lasers ranging from 10 to 150μm stripe size with different cascade stages were characterized. The MCT detector was rotated around the laser cryostat to record the beam profile along the growth direction. The reason to place the detector on a rotatory station is due to its limited field of view (±33^{o}) [61] which is insufficient to collect the entire laser light when the detector moves away from the laser. Moreover, the laser light might be reflected back from the polished wall of the detector holder and can affect the original signal.

The half divergence angle of the far-field beam was calculated using two different methods to check the integrity of the experiment. The first method is based on the beam diameter of the far-field and the distance between the laser and the detector. The beam diameter of a far-field is measured by the FWHM where the beam intensity

falls to $1/e^2$ or 13.5% of its maximum value and the distance between the laser and the detector was kept at 50mm. The method of calculating θ is shown in Figure 4-8.

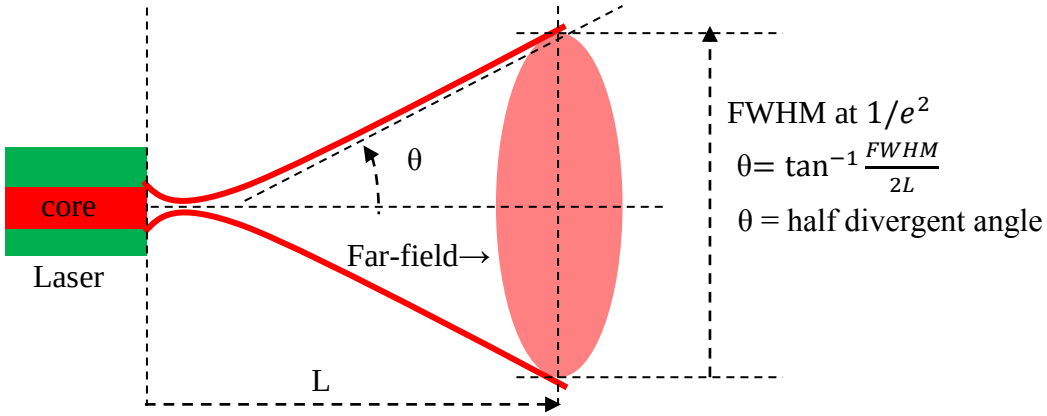

Figure 4-8: Calculation of half divergence angle from the experimental far-field pattern.

The second method was based on taking the far-field measurement at two different distances from the laser. The idea of this measurement was based on the fact that the wave front of the laser beam would diverge at the same rate when the distance was increased. This method is described in Figure 4-9 :

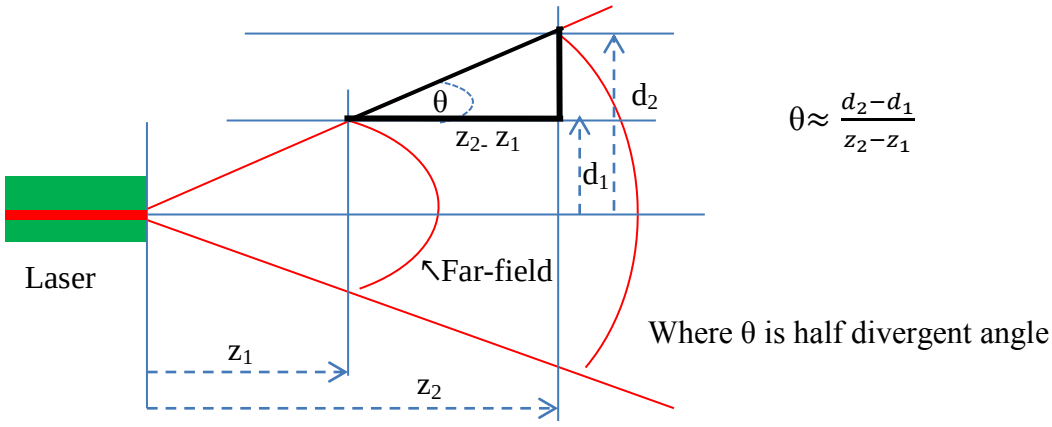

Figure 4-9: Alternative method to calculate half divergence angle.

Both of these methods should be accurate and reliable to calculate the half divergence angle, however, the later method needs two sets of data at two different distances, which increases the complexity and was avoided.

4.6.1 Vertical beam profile

The width of the active region along the growth direction is 416nm for the wafer V1189 & V1191 and 608nm for V1192. According to diffraction theory, the smaller width will diffract the light faster. As a result, the divergence angle of the first two lasers from wafer V1189 and V1191 should have comparatively larger values than those from the wafer V1192. However, the result shows that the median value of the half divergence angle of all three wafers along growth direction are comparable as given in Table 4-1.

Table 4-1: Median value of FWHM of three lasers.

Sample	Wavelength (μm)	Size of active region (nm)	Half divergence angle (median, degree)
V1189	4.6	416	48.60
V1191	4.6	416	50.34
V1192	6.0	608	49.86

All of the wafers mentioned above exhibited similar divergence angles with less than ~3.5% difference. The possible reason of having slightly higher divergence angle for lasers from wafer V1192 might be due to the fact that the half divergence angle increases with increasing lasing wavelength following the equation $\theta = \frac{\lambda}{\pi\omega}$. The beam profile along the growth direction for different stripe size lasers from these three wafers are shown below in Figure 4-10:

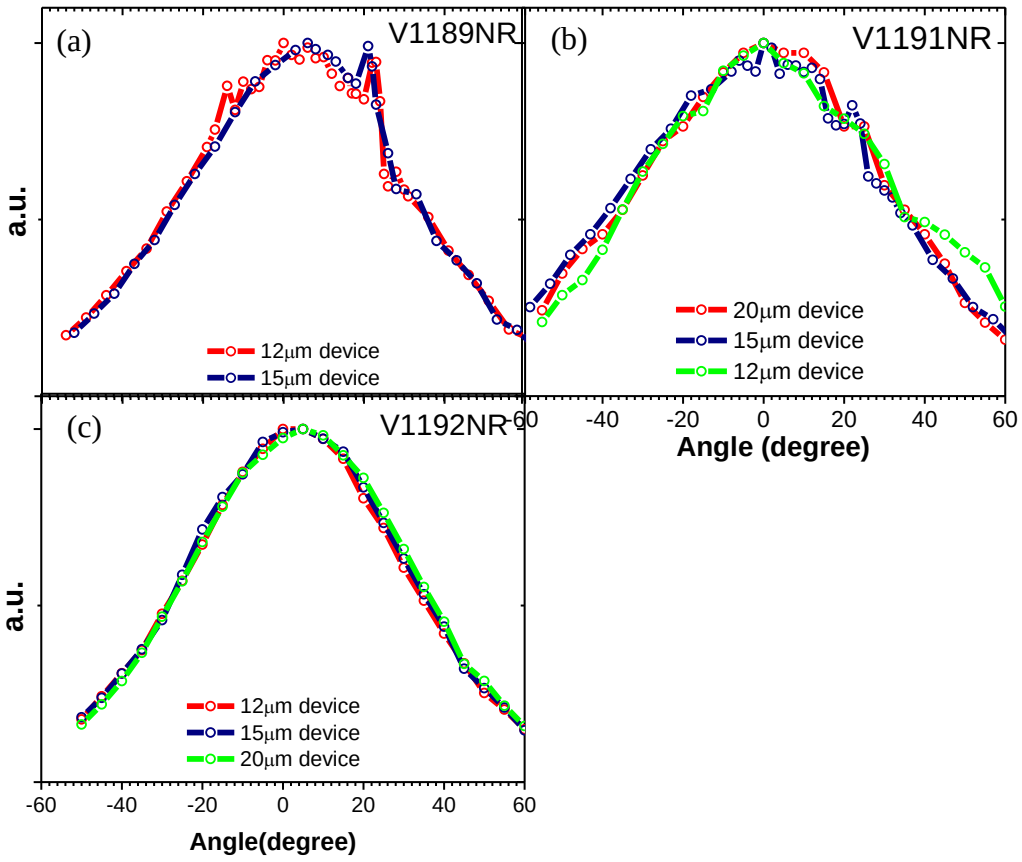

Figure 4-10: Beam profile along the growth direction of narrow ridge lasers from the wafers (a) V1189, (b) V1191, and (c) V1192, respectively.

Apart from their similarities in the half divergence angle, the lasers from V1192 have smooth and consistent far-field patterns with no ripples or zigzags on the profile as shown in Figure 4-10 (c). The ripples and roughness on the beam shape usually indicate the presence of mode leakages [92]. Hence, the beam profile smoothness could be related to superior waveguide design, better confinement of the electric field, lower internal loss and especially internal mode scattering. However, more lasers from different wafers are needed in order to firmly relate beam profile to waveguide issues.

The experimental results are compared with the simulated beam profile for different size laser stripes and shown in Figure 4-11.

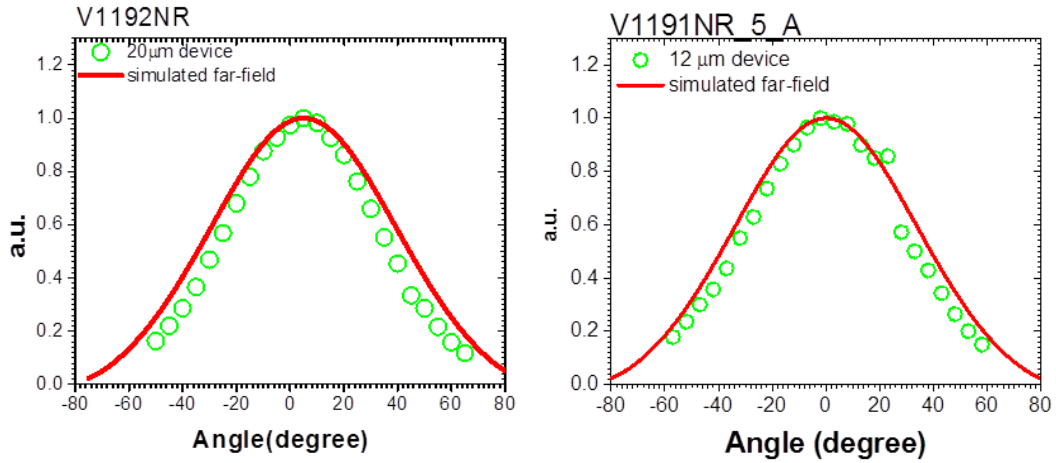

Figure 4-11: Comparison of the simulated beam profile with the experiment.

The simulation is based on Equation (22) which uses the near-field beam waist, far-field divergence angle and lasing wavelength to calculate the beam intensity. The beam waist, w_o and divergence angle are calculated from the simulated near-field intensity as shown in Figure 4-4. We have found that the simulated beam spreads over the experimental beam profile as shown in Figure 4-11. This can be explained by the fact that the optical parameters used in the simulation were collected from contemporary handbooks of optical constants which may vary. As a result, the simulated data spread over the experimental profile. The beam quality factor M^2 is calculated by dividing the measured half divergence angle to that from a pure Gaussian beam along growth direction from three wafers and plotted in Figure 4-12.

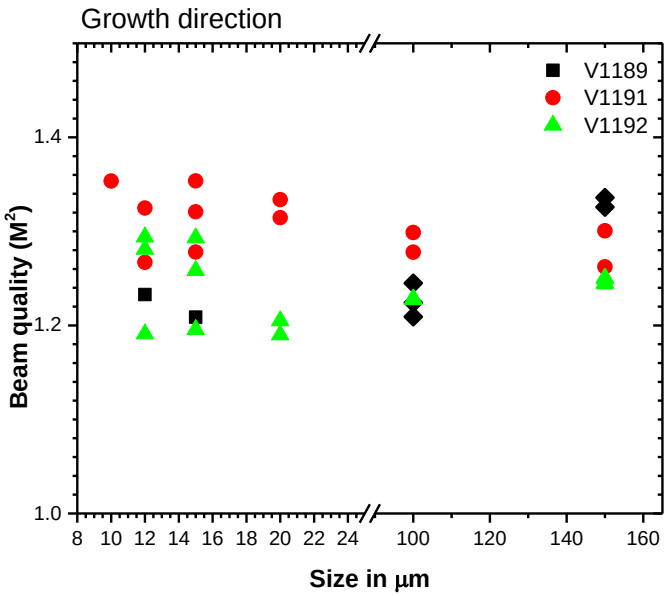

Figure 4-12: Beam quality factors in the growth direction.

The beam quality factor M^2 is found in the range of 1.2 to 1.35 for all of the lasers from all of the wafers. These values are close to unity which indicates better beam quality in this direction. Hence, we can conclude that the far-field beam profile along the growth direction is diffraction limited and close to a Gaussian beam.

4.6.2 Lateral beam profile

To increase the laser output power, often the laser is prolonged along the lateral direction as the active region width has to be fixed based on the waveguide design requirement. Thus, a bigger active region volume can generate higher laser output power. However, this bigger stripe size of the laser degrades the beam quality by accommodating higher order lasing modes in this direction. The lateral beam profile along with higher order modes from both narrow-ridge and broad-area lasers are shown in Figure 4-13 and Figure 4-14.

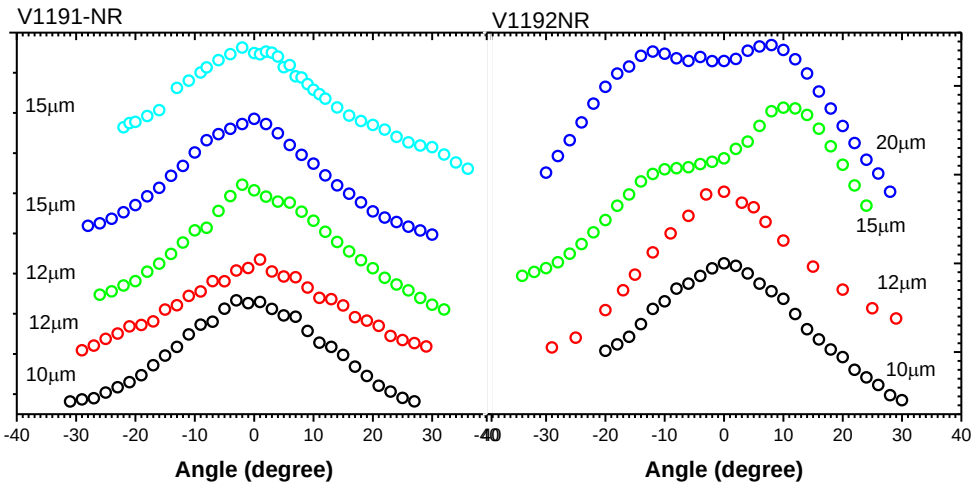

Figure 4-13: Lateral beam profiles of narrow-ridge lasers (stripe size, 10 to 20µm).

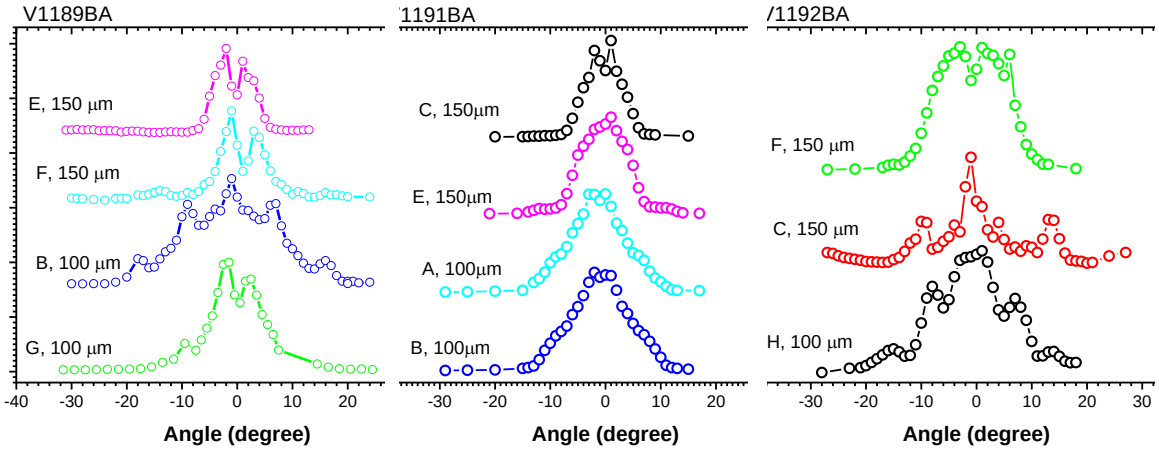

Figure 4-14: Lateral beam profiles of broad-ridge lasers (stripe size, 100 to 150µm).

Figure 4-13 shows that the lasers with smaller stripes, especially 12µm or less, exhibited single mode far-field quasi-Gaussian beams where the lasing wavelength is comparable to the stripe length. As the stripe size started to get larger, higher order modes started to show up and became prominent on 100µm or higher stripe size lasers as seen in Figure 4-14.

The refractive index of any index guided lasers changes due to the free carrier plasma effect. When operating conditions change, especially the bias current, then the mode competition takes place inside of the waveguide and the fundamental TE mode or higher order modes can gain sufficient energy to show up in the output. As seen in Figure 4-15, a broad-area laser with a 100μm strip size exhibited two higher order lobes in the far-field when applied bias current was slightly higher than the threshold current. As the applied current increased from 2 to 4A, the refractive index was changed inside which affected the beam profile. In Figure 4-15, initially two lobes were observed and eventually the right lobe was suppressed with an increase in the applied bias current which presumably affected the cavity gain. Nevertheless, this gain mechanism might also come from thermal generation too. However, the applied pulsed current was very small and should generate a negligible amount of heat.

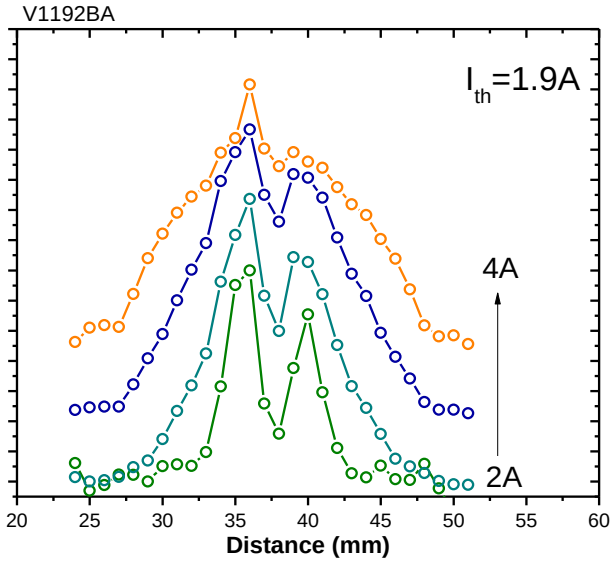

Figure 4-15: Effect of bias current on the lateral beam profile.

Similar to the growth direction, the beam quality factors in the lateral direction were calculated and plotted as shown in Figure 4-16.

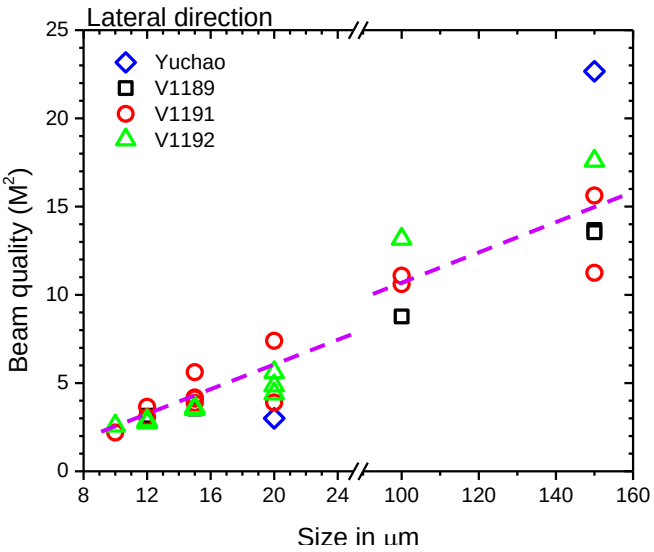

Figure 4-16: Beam quality factor in the lateral direction.

As expected, the beam quality factor increases with an increase in the lateral stripe size of the laser. The value of M^2 was found in the range of 2.2 to 18, depending on the device stripe size (10 to 150μm). These large beam quality factors indicate inferior far-field beam quality in the lateral direction which is lower than the beam quality factor obtained from ICL (DFB laser) from our group [32]. Though there is no straight relationship found between the stripe size and beam quality factor, it is evident from Figure 4-16 that the higher stripe size degraded the beam quality.

4.7 Conclusion

The laser beam of an ICL was investigated and analyzed for both broad-area and narrow-ridge geometries in the far-field region. Along the growth direction, a single-mode near diffraction limited laser beam was obtained. A Multi-mode laser beam was observed in the lateral direction as expected. These lateral modes are dependent on the applied bias current. The propagating far-field beam profile was compared to the simulated far-field pattern and a reasonable agreement was obtained. Finally, the beam

propagation factor was plotted against the laser stripe size. This factor was found to be close to unity along the growth direction, indicating better beam quality, and below 18 along the lateral direction indicating further room for improvement. More thorough investigation on far-field measurements can be carried out by also measuring the previously grown ICLs. In this regard, this study could be very helpful towards better understanding of the ICL laser beam optics.

Chapter 5: Single mode operation of cleaved-coupled-cavity ICL

5.1 Introduction

Recently, OU's InAs-based laser demonstrated record low threshold current density with room temperature operation beyond 6μm wavelength [16]. Here, an ICL along with an interband cascade infrared photodetector (ICIPs), a detector class from this IC family, were monolithically integrated together to form a lab-on-a-chip proto-type , [93]. In this chapter, the capability of ICLs are extended by demonstrating single longitudinal mode by using two-section cleaved-coupled-cavity (CCC) laser.

5.2 Motivation and background

Some particular applications (e.g., tunable laser absorption spectroscopy, gas detection, data transmission, THz wave generation etc.) require single-mode lasing. This is especially important in optical communication to ensure error-free data transmission. In high resolution spectroscopy, along with the requirement of single mode emission, narrow line width is also preferred to achieve the necessary selectivity to distinguish the molecules that have similar vibrational-mode absorption peak.

There are many ways to achieve single mode emission from a laser, including: extremely short cavity lasers [94], distributed Bragg reflector (DBR) lasers [95], external cavity lasers [96], photonic crystal resonators [97], and distributed feedback lasers (DFB) [98, 99]. Among these, DFB and DBR lasers are well established to demonstrate single mode lasers but they require complicated fabrication process such as regrowth and grating fabrication etc. The other laser categories often need additional

equipment to operate in a single mode that are susceptible to mechanical vibration. These additional design requirements impose challenge in device design, growth, process and fabrication, which ultimately affect device performance, cost and compactness.

In the 1980s, a novel and new concept was proposed for lasers to generate single mode emission by coupling two Fabry–Pérot (FP) cavities [34, 35, 100, 101]. This approach can be reconsidered and applied to interband cascade lasers as an alternative way to overcome some of the limitations related to the mentioned contemporary techniques to meet up the present and future size and power requirement. Furthermore, the simple design of these coupled cavities can keep the packaging compact making it suitable for low power on-chip chemical sensing applications.

5.3 Two-section cleaved-coupled-cavity (CCC) laser

In the regular design of semiconductor lasers, the gain medium, often called *active region* is sandwiched between two low-refractive index cladding regions to confine light. The generated light confined into this active waveguide region gets amplified and leaves the cavity through the cleaved facet as a coherent laser light. The lasing wavelength and corresponding state-of-the-art performance depend on the design, geometry and material system used. The conventional semiconductor laser design, especially that uses FP resonator as a gain medium, generates multiple longitudinal lasing modes in their output.

To generate low cost, easily fabricated and less complex single-mode lasers, the simplest technique is to etch a shallow slot on top of the ridge of a FP resonator to separate the cavities and provide constructive interference to select a particular mode

and destructive interference to suppress the unwanted side modes. In this regard, several composite cavity structures were studied theoretically and experimentally including cleaved-coupled-cavity, V-coupled cavity and multi-section lasers [102-105]. These structures require deeply etched mirrors with narrow gap and vertical sidewalls.

Considering the simplest operating principle and easy way of fabrication, two-section cleaved-coupled-cavity (CCC) laser are an appropriate method to generate single mode in ICL. In our version of this method, CCC can be realized by using regular etching technique such as reactive ion etching (RIE) or focused ion beam (FIB) milling. To prepare the CCC based on our ICL, we are required to etch such a narrow gap which should be comparable to the lasing wavelength. For this purpose, based on its availability at our University and wanting to avoid the design requirement of a special, extra mask in dry etching technique, we chose FIB as our etching method. Furthermore, FIB will provide the flexibility to adjust the size of the etch-gap between the two CCC laser sections.

Figure 5-1 shows a schematic cross-sectional view of a two-section CCC laser comprises of two FP cavities, denoted as *cavity-1* and *cavity-2*. These two cavities are electrically separated by a narrow air-gap. Cavity-1 is referred to as the *"active resonator"* and cavity-2 as the *"passive resonator"*. Typically, the length of the active resonator is longer than the passive resonator. The purpose of the active resonator is to generate multimode longitudinal lasing and provide most of the gain. The passive resonator provides a tuning mechanism to select a particular mode of the active resonator and suppress other side-modes. These cavities are pumped by separate electrical current as I_1 and I_2. These electrical currents will give the flexibility of

controlling the output spectrum of the combined laser by adjusting the individual cavity gains and refractive indexes via these input currents. The air-gap between the FP resonators acts as *coupling medium* and should be comparable to the lasing wavelength.

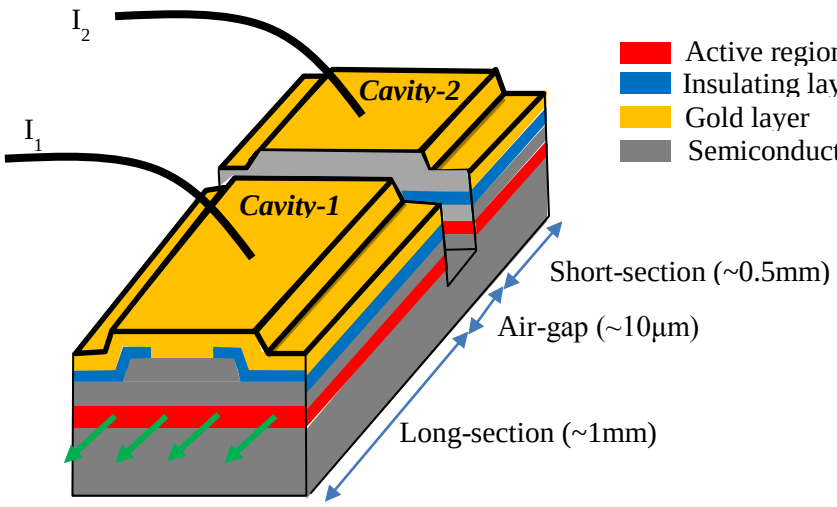

Figure 5-1: Schematic of a CCC laser with two electrodes.

The operating principle of coupled cavity laser is simple. The long-section generates multiple longitudinal modes with shorter mode spacing and the short-section generates modes with longer spacing, as shown in Figure 5-2.

.

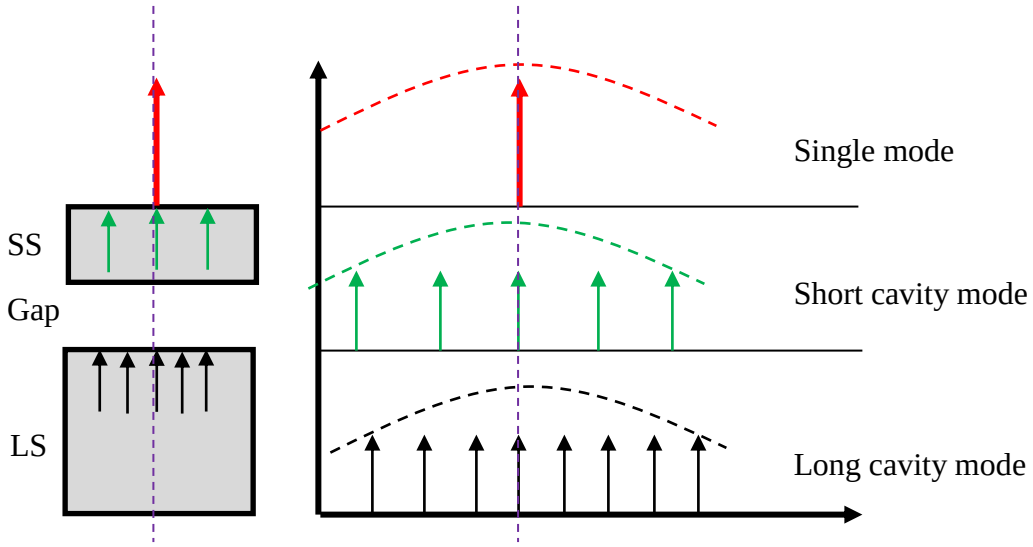

Figure 5-2: Operating principle of a CCC laser.

The relative position of these modes with respect to individual cavity can be shifted by changing the applied current in each section. The applied current injects carriers in the active region that changes the refractive index and shifts the modes accordingly, without changing the mode spacing as the length of the sections are fixed. Typically, the current in the long-section is kept constant, while the current in the short-section is changed in such a way a mode in this short cavity coincides with a mode coming from the long-cavity. These selected common modes from both the cavities will then undergo the constructive interference and lasing at this single mode wavelength results. The side modes of the long-section will be suppressed by destructive interference, as illustrated in Figure 5-2.

In short, the coupled cavity laser, the output spectra from both the cavities couple based on the coupling efficiency inside the air-gap, and select a single resonant mode. A brief theory of operation and simulations based on a scattering matrix approach are described in the following section.

5.1 Theory formalism by scattering matrix method

In regular single-cavity FP lasers, the threshold gain requirement is independent of wavelength where each of the allowed cavity modes will have the same threshold gain. But, for coupled cavity lasers, the threshold gain requirement of a given mode will depend on the gain or loss of both individual laser section and the air-gap where the optical feedback takes place. The light that enters this air-gap from both the cavities undergoes multiple reflections by the partially reflective etched-sidewalls. A fraction of the light from the air gap returns back into the active section of the two devices. The strength and phase of the coupling between the two laser sections depends on this air-gap geometry.

To analyze this coupling between the two cavities, we adopted the simple transfer-matrix method to find the transmission, reflection and coupling coefficients of the air-gap coupler. The rigorous analysis was done by Henry *et al*., [34] who developed a threshold gain model using a round trip condition for longitudinal modes to find relationships between wavelength tuning and mode selection behavior, where the key design parameters were the cavity length ratio and the size of the air-gap coupler. This theory was later extended to design multi-section laser cavities to obtain more control on device operation [106, 107]. However, in our case, we keep the physics simple as we just had two cavity sections to control the gain and only needed to determine our optimum air-gap length to be etched by FIB.

Following on Figure 5-1, the geometry of the coupled cavity laser is shown in Figure 5-3, where the length L_1 of the active cavity is longer than the passive cavity length L_2. The coupling of light between these two cavities is affected by the loss and

phase shift experienced by the optical field, associated with the gap-coupler of length L_g. As shown, the reflectivity of the laser facets are r_1 and r_2. The air-gap itself can be treated as a FP cavity, where the amplitude of the incident electric field from active and passive cavity are E_1 and E_2, and the corresponding reflected fields are E_1' and E_2'.

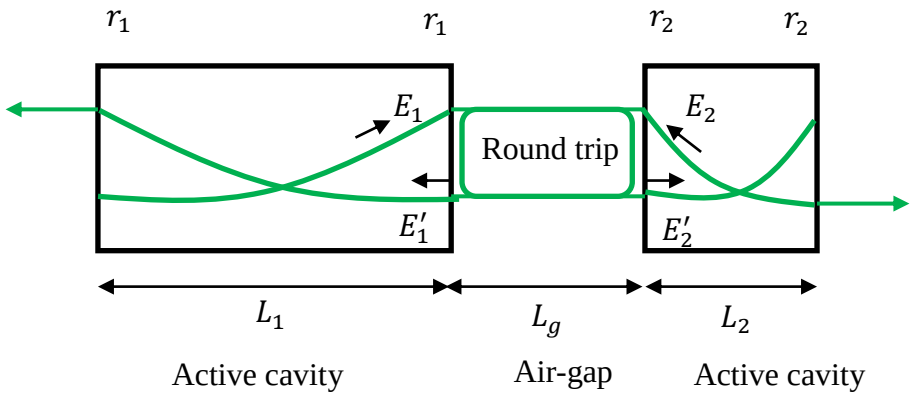

Figure 5-3: Coupled cavity laser for transfer matrix formalism.

Applying the transfer matrix method, the coupling of the air-gap are related by the following matrix elements,

$$\begin{pmatrix} E_1' \\ E_2' \end{pmatrix} = \begin{pmatrix} S_{11} & S_{12} \\ S_{21} & S_{22} \end{pmatrix} \begin{pmatrix} E_1 \\ E_2 \end{pmatrix}. \tag{25}$$

In this matrix, the reflection coefficient is defined as $S_{11} = E_1'/E_1$ and the transmission coefficient as $S_{21} = E_2'/E_1$in the air-gap. Similarly, S_{12} and S_{22} can be obtained and written as:

$$S_{11} = S_{22} = r_1 - \frac{r_2\,(1 - r_1^2)t_g}{1 - r_1 r_2 t_g} \tag{26}$$

and $$S_{21} = S_{12} = \frac{[t_g(1-r_1^2)(1-r_2^2)]^{\frac{1}{2}}}{1-r_1 r_2 t_g}, \tag{27}$$

where t_g is defined as:

$$t_g = e^{2i\beta_g L_g} = e^{2ik_0 L_g} * e^{-\alpha_g L_g}$$
$$\text{with} \quad \beta_g = k_0 + i\frac{\alpha_g}{2}, \tag{28}$$

where β_g is phase shift, $k_0 = \frac{2\pi n_{eff}}{\lambda}$ is propagation phase, $\alpha_g = \Gamma g_m - \alpha_{loss}$ is gain constant, Γ is confinement factor, g_m is modal gain, and α_{loss} includes all other cavity losses.

In an ideal case, there is no loss inside the air-gap coupler and the maximum transmission of electric field occurs when $L_g = \frac{m\lambda}{2}$ (with m=1, 2, 3 …), as shown in Figure 5-4 (a). Practical air-gaps are lossy mainly due to the diffraction spreading of the beam and this loss can be estimated [108, 109]. For a lossy air-gap coupler (loss arbitrarily chosen for simulation), the total strength of transmission decreases with the length of air-gap, as seen in Figure 5-4 (b). Hence, it is recommended to keep the air-gap smaller than the length of a multiple of half wavelength for best performance.

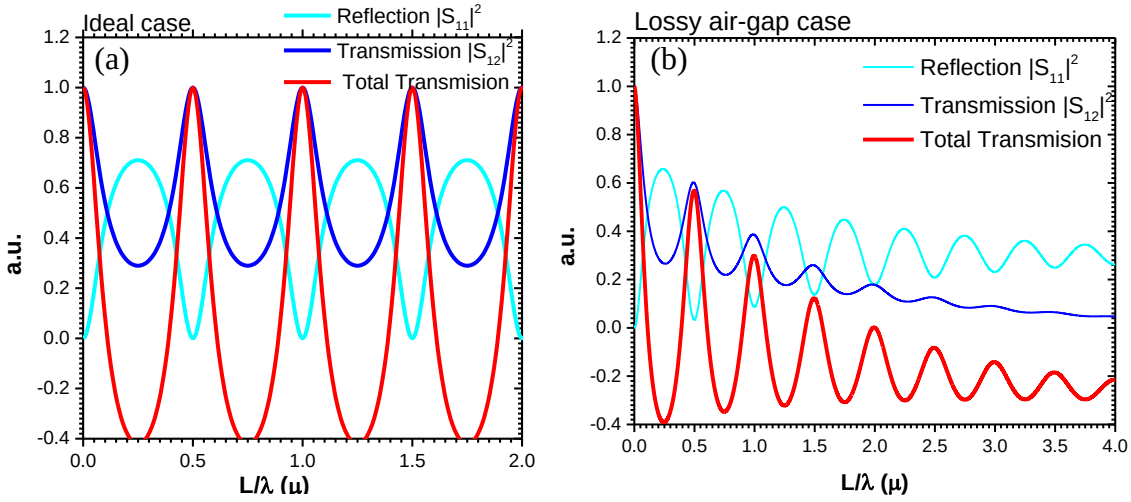

Figure 5-4: Simulated transmission and refection coefficient in the air-gap in the (a) ideal and (b) lossy cases.

The strength and phase dependence of the coupling can be expressed in the form of complex transmission and reflection coefficient as follows:

$$C = e^{i\theta} = \left(\frac{S_{12}S_{21}}{S_{11}S_{22}}\right)^{\frac{1}{2}} \tag{29}$$

where C is mutual coupling coefficient, and θ is phase of the coupling.

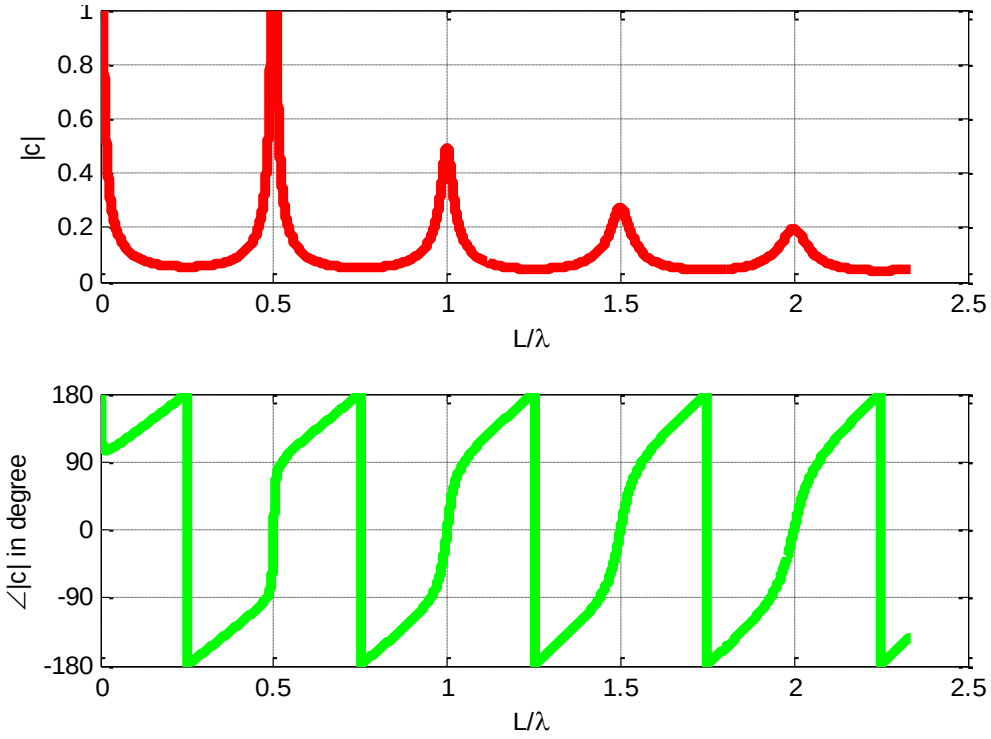

Figure 5-5: Dependence of the coupling constant *C* and coupling phase θ to the air-gap width *L*.

Figure 5-5 shows the dependence of the value and phase of the mutual coupling constant on air-gap length. This figure shows that the coupling constant is higher when the air-gap is a multiple of half wavelength of the laser. At his half wavelength point, the phase of the transmitting and reflecting wave is zero, due to the constructive interference of the waves.

5.2 Device structure

To realize CCC, a six-stage type-I ICL grown on a GaSb substrate with quaternary $Ga_{0.45}In_{0.55}As_{0.22}Sb_{0.78}$ quantum well (QW) active regions was used for the base structure. The entire ICL structure was grown on an *n*-type GaSb substrate in a V90 molecular beam epitaxy (MBE) system using As and Sb valved cracker cells and conventional group-III and dopant effusion cells, by the National Research Council of Canada. The calculated band profile based on two band model and detail layer sequence of one cascade stage is shown in Figure 5-6.

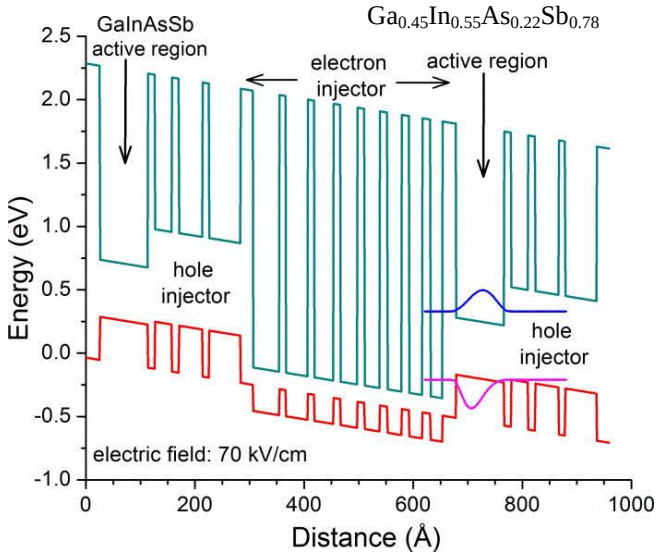

Figure 5-6: Calculated band profile of one cascade stage under an electric field of 70KV/cm [110].

More details about this ICL structure and laser performance have been reported elsewhere [110]. After processing at OU, a nominal ridge width of 12μm and a cavity length of 1.5mm was selected to make the CCC laser. Along the longitudinal cavity direction of this ICL, there is a ~50μm-wide stripe without a gold layer as shown in a scanning electron microscope (SEM) image (see Figure 5-8 (b)) that electrically connects the two adjacent sections. This stripe was originally designed to allow

cleaving the structure into 1.0mm or 0.5mm-long lasers. The connecting gold layer (above the 50μm-wide stripe) was deposited by using electroplating gold of ~4μm thick.

After the device was selected, FIB technique was used to make the two-section laser by milling through the above mentioned gold stripe and into the mesa. The detail of the focused ion beam etching is described in below section.

5.3 Focused ion beam (FIB)

FIB is a technique used particularly in semiconductor industry, material science and increasingly in biological field for deposition and ablation of material [111] by using finely focused beam of gallium ions that can operate at a low beam currents for imaging or high beam current for site specific sputtering or milling. An illustrative schematic of FIB with Ga^+ ion as a source on an arbitrary material is shown in Figure 5-7.

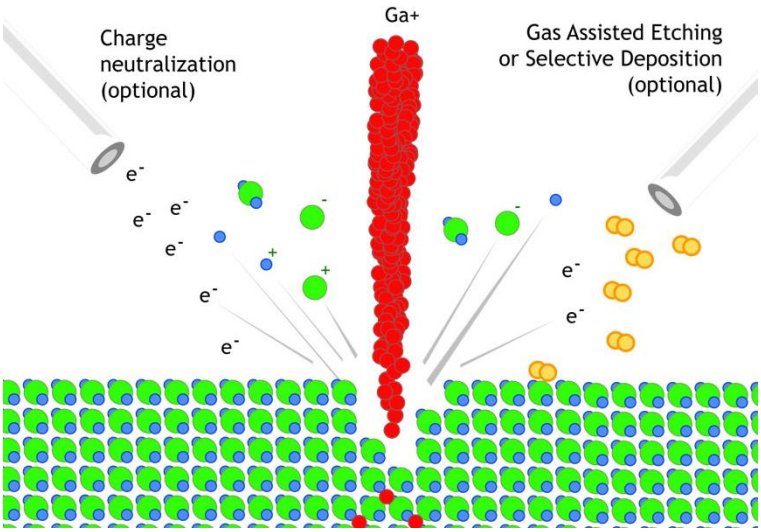

Figure 5-7: Illustrative schematic of a focused ion beam milling [112].

■ Why FIB?

From coupled-cavity laser theory, the length of the air-gap coupler that separates the active cavity to the tuning passing cavity should be comparable to the lasing wavelength of the laser. Indeed, the best coupling can be achieved if the air-gap becomes the multiple of half of the lasing wavelength. There are few choices available to open narrow channel on top of the mesa considering the lasing wavelength as 3.15μm. The easiest would be micro-cleaving technique that would follow the natural cleave line to "break" the laser into two parts or create a "V" shaped groove on it [113]. However, this technique needs a special skill-set and it is experimentally difficult to align the two cavities. The other typical technique is to dry etch the trench which can precisely control the etching width and depth and particularly it is very direction while etching down and it can able to produce vertical and smooth trench sidewalls [107]. But, this technique requires additional masks and associated lithography that would increase the complexity and the cost of the process. Another technique to open a trench is wet chemical etching. However, the wet etching of the different III-V materials in the laser structure is y preferential (etch rates vary), which typically produce over-hanging sidewall structures. Furthermore, the etching speed and directionality is hard to control. As a result, it is very difficult to produce the required shallow trench, with flat perpendicular sidewalls using wet chemical etching.

Focused ion beam is an easy and low-cost technique to open shallow channels on top of the mesa of semiconductor lasers. This technique uses Ga ion bombardment on sample surface to sputter out the host material and make a trench. Hence it is a physical, non-reactant technique to make any type of trench. This technique does not

require any special processing or fabrication, and it available on cross-beam SEMs. As was found in this work, the optical performance of natural cleaved facets and the facets made by FIB are comparable [114].

The FIB technique was successfully used in quantum cascade laser (QCL) to cut 8μm-deep trenches about 9μm×32μm in lateral size isolate two laser sections [115, 116]. In some cases, gas-assisted FIB etching is used to improve the quality of the etching (side and bottom walls) [117, 118].

- **Key criteria, figure of merit and etch recipe**

The main criteria for FIB milling of ICL are to produce a vertical and smooth sidewall profiles. The reflectivity of this etched mirror will depend on the quality of the etching. Another criterion of FIB etching is to precisely control the etching dimensions because the width of the trench is very important (it is often comparable to lasing wavelength).

The key figure-of-merits of FIB milling is the quality of the sidewall. These qualities are measured in terms of smoothness, device resistivity, and degradation over time. The smoothness of the sidewall is measured by comparing the SEM images of the sidewall from different angle to that of as-cleaved facet. A rough, corrugated and angled surface degrades the reflectivity of the facet. The resistivity of the laser before and after FIB etching should be comparable. Lower resistivity after may indicate the deposition of a conducting gallium layer along the sidewalls. Finally, the FIB etched surface should be stable over time.

To achieve these criteria, different FIB recipes were investigated in order to obtain smooth, vertical and stable sidewall profile. The process of removing the atoms

(sputter removal) from the surface is done by striking the surface to be etched with Ga^+ ions. Usually, higher FIB current is used for coarse and fast milling and this typically produces rough surfaces. During this process, the tendency of the etched material to get re-deposited on the sidewall is high. To address this problem, often different types reactive or non-reactive gas species such as Ar, XeF_2 *etc*. are used to physically (Ar) or chemically (F from XeF_2) assist with the removal of the etched by-products so as to prevent sputter re-deposition. Lower FIB current are usually necessary to polish initially rough surfaces. In this low current FIB milling, the possibility of re-deposition of by-product atoms on etched sidewall is lower. This re-deposition can be reduced significantly by etching all the four side walls in rapid sequence (etch one layer from one wall and then a layer from the opposite wall, etc.), but this requires precise control over etching patterns an dimensions [119].

Damage associated with FIB milling is mostly depend on beam energy, current and geometry. High energy milling leaves rough bottom and sidewalls that are typically followed by fine polishing with lower energy FIB beam, as a recovery step to improve sidewall morphology. Using FIB beams at angles to the side walls can also lead to better surface quality. With appropriate precautions, FIB is an easy and quick way to make shallow channel on mesa to isolate two sections of ICL.

- **Design requirement**

The coupled cavity laser required two sections of unequal length that needs to be electrically and optically isolated. For our work, we choose a 1 mm-long narrow-ridge laser (~10μm wide mesa). Along the longitudinal cavity direction of this ICL, there was a ~50μm wide stripe (see SEM image in Figure 5-8). To make a ~1mm long active

cavity and ~0.5mm long passive cavity, we need to isolate these two sections electrically by milling a ~40μm-wide slot through the electroplated Au layer, as indicated by the red dashed line in Figure 5-8. For the second FIB slot for optical isolation, we needed to choose the width of the slot as a multiple of lasing wavelength. In this regard, we choose to make a ~10μm wide and ~9μm long slot into the mesa, as shown by red dashed in line in Figure 5-8. For both slots, the depth of milling needed to should be more than 6μm to go completely through the active region.

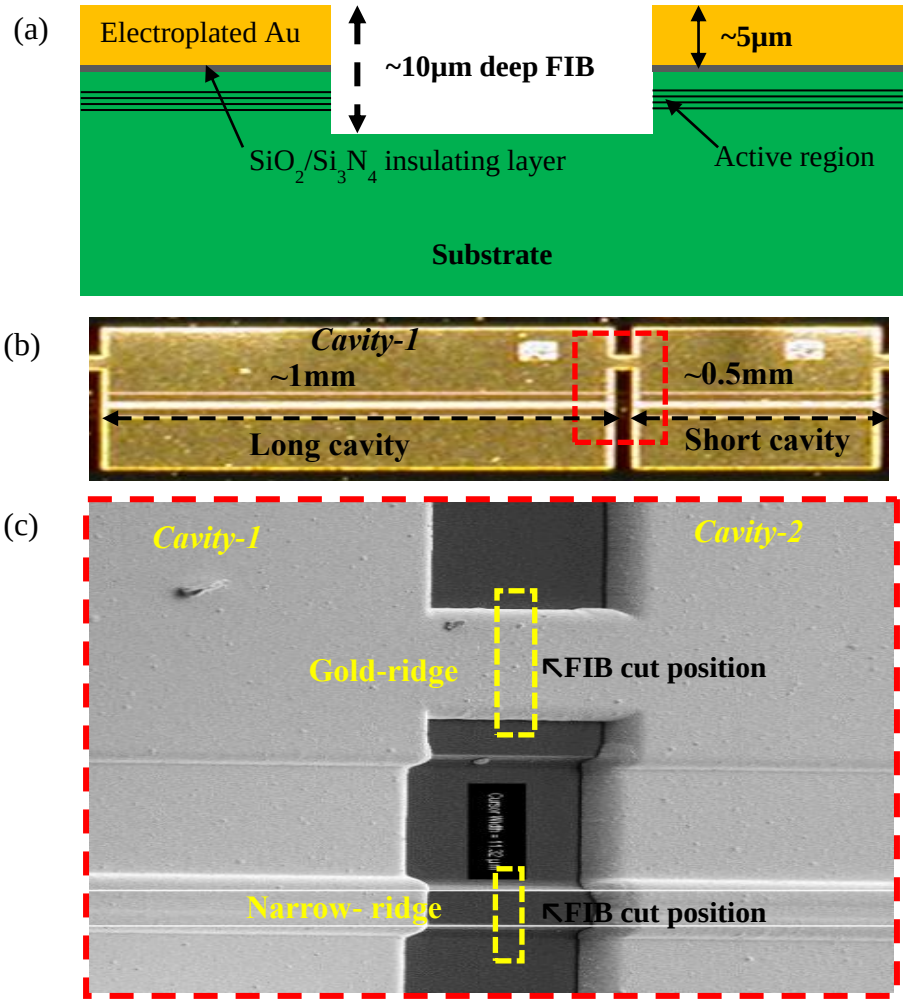

Figure 5-8: (a) Schematic of a CCC laser, (b) Differential Interference Contrast (DIC) image, and (c) Scanning Electron Microscopy (SEM) image.

The design parameters are as follows:

- **Semiconductor mesa depth** : ~3.3μm
- **SiO_2/Si_3N_4 thickness** : ~0.4μm
- **Ti+Au contact layer** : ~4.5μm
- **Narrow-ridge cut** : ~10×9×10μm^3
- **Au-bridge cut** : ~60×2×10μm^3

■ Experimental setup

The experimental setup and procedure for FIB started with mounting the sample on a custom made sample holder. The FIB gun, as shown in Figure 5-9, is 36^o angle with respect to horizontal line. To make the FIB nozzle perpendicular to the laser, the stage was placed in a tilted angle of ~14^o. The working distance between the tip of the FIB nozzle to the device was kept below 5mm as per the FIB manual.

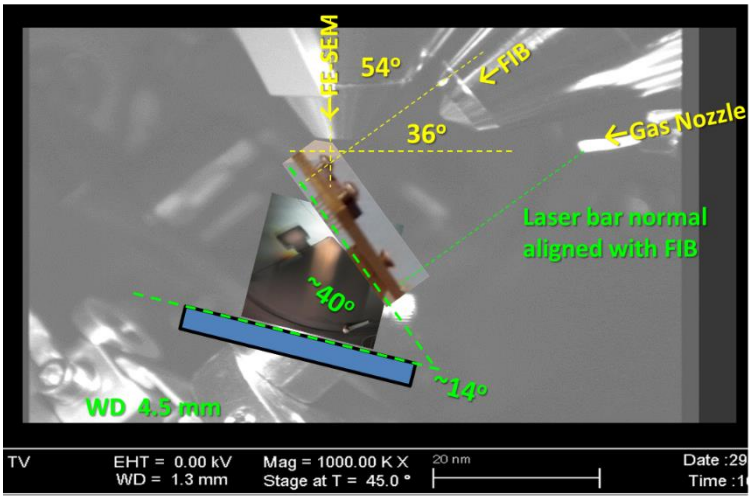

Figure 5-9: Camera view from back inside the SEM chamber. The SEM, FIB and gas nozzles are marked, and relative angles were shown.

After placing the ICL, the gas nozzle was placed as close as possible to efficiently provide gas flow to milling surface. The milling direction was chosen from middle to the edge of the sidewall to keep the by-product re-deposition to a minimum. After finishing the milling, a few good SEM images were taken to check the important properties of the milled slot, such as the width, depth and sidewall morphology. Finally, after taking the device out, the resistance was measured and compared to that of comparable devices or the values before the FIB etching process.

- **Gold-bridge milling**

The FIB milling starts with slicing the gold bridge to electrically isolate the two sections of the laser. According to the design, a 60μm×10μm×10μm slot is sufficient to separate it. The depth of this milling is not critical as long as it could penetrate through the insulating layer underneath the gold layer. Actually, two processes were developed to successfully separate this gold bridge. Both of the processes were carried out using gas-assisted milling, as described in the narrow-ridge milling section.

According to the first process, a 60μm×10μm×10μm slot was milled using a high FIB current of 2nA and 30keV accelerating voltage. In this coarse milling step, we found that gold from top of the layer redeposited at the bottom of the semiconductor walls resulting in a decrease in the device resistance. To clean up this gold layer, a fine polish region with width of ~100nm using a 50pA FIB probe current and 30keV accelerating voltage was used. This fine polished increased the sidewall smoothness and device resistance, as shown in Figure 5-10 (b). However, this method was time consuming as it introduced two extra polishing steps to clean up the gold redeposition.

Furthermore, the milled debris started depositing on the opposite sidewalls during the fine polishing of one sidewall.

In the second process, two small slots of 60μm×2μm×10μm were milled in two places on the gold bridge, as shown in Figure 5-10 (a). As the width of the milling was small (in the range of ~2μm), the gallium and the milled atoms were less prone to get redeposited into the sidewalls. Furthermore, this coarse milling took less time to operate.

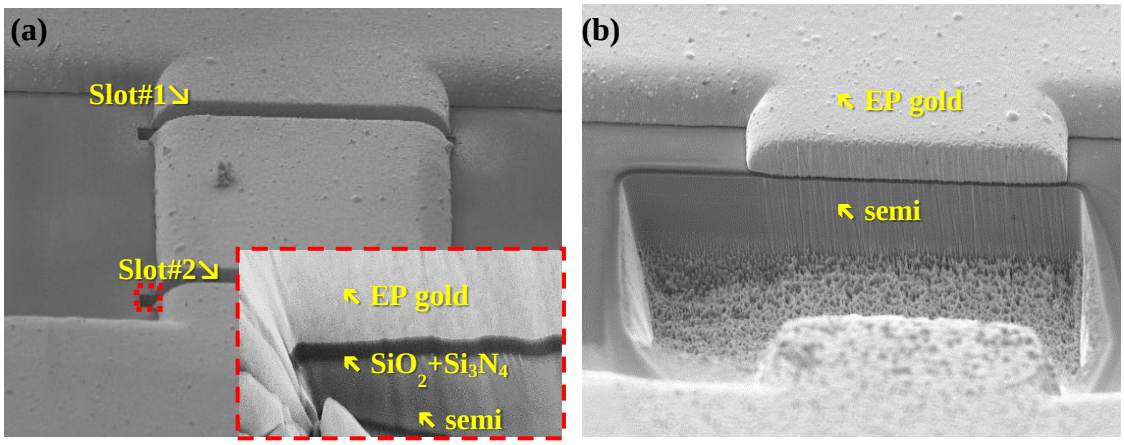

Figure 5-10: (a) SEM image of the gold-bridge with two small milled slots, inset: sidewall of the slot and (b) with one large milled slot.

■ Narrow-ridge milling

In this milling process, we cut a 10μm×9μm×10μm slot on top of the laser mesa structure to optically separate the two laser sections. The sidewall of this slot should be smooth so that its reflectivity is comparable to that of a cleaved facet. This sidewall must not be coated with any kind of layer of gallium or conductive debris, otherwise, it will short the active region and hurt the performance of the two lasers.

Again, the device was mounted on a custom-made sample holder and the working distance between the ICL and FIB nozzle was ~1mm. The position of the slot

was selected to be approximately in the middle of the mesa. Based on the literature and instrument manual, the FIB beam current for coarse milling was selected as 2nA with 30keV accelerating voltage. This *Zeiss Neon* machine used for FIB had the ability to see the real-time milling in SEM mode, so, we were observing the milling for all the time. The milling took ~30min to finish and the corresponding SEM image is shown in Figure 5-11 below.

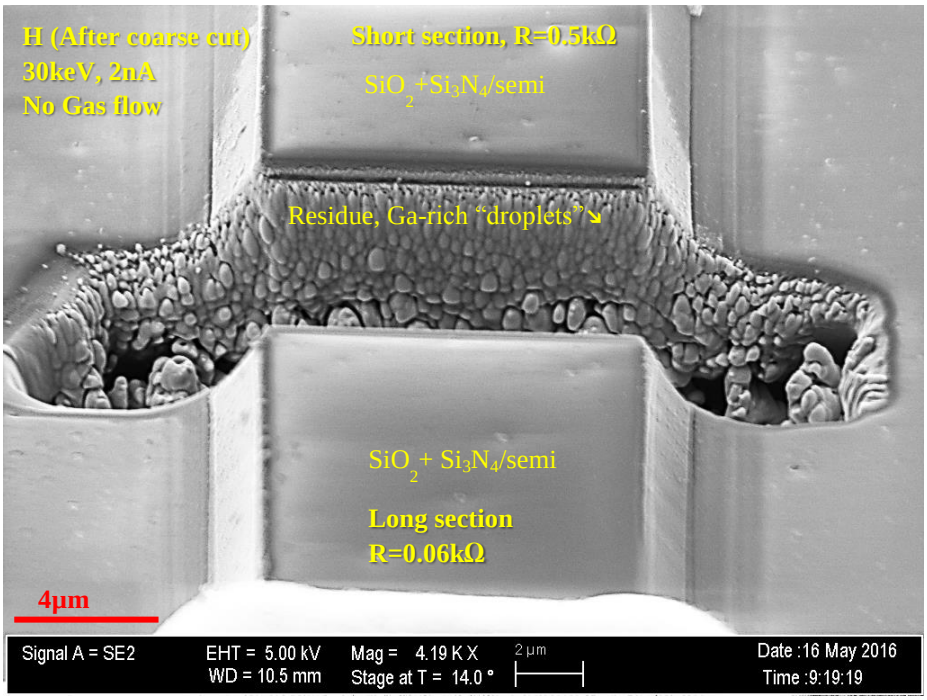

Figure 5-11: (a) SEM image of the mesa after the gross-cut. Rough side-wall is seen.

The resistances of the laser bars after the course milling were below ~1kΩ in both sections (it was ~22kΩ before milling). This is due to the formation of Ga-rich droplets on the active region making the sidewalls rough and conductive (see Figure 5-11). The FIB probe actually rasters from side to side to cut a single layer. When it milled deep down inside the slot, the etched by-products start to get deposited on the sidewalls of the slot making it rougher. We tried to cut the slot by using two sequences:

the first sequence started from middle to one edge and second sequence started from middle to other edge, but the resistance of the after etch devices did not improve appreciably. We also dipped the rough slot into dilute (5%) hydrochloric acid to remove the Ga-rich droplets but the laser resistance only went up to ~2kΩ. We also tried to fine polish the sidewall one at a time with low FIB current of 100pA and 30keV accelerating voltage. But, the by-products started depositing on the opposite sidewalls while polishing them individually.

To improve the sidewall morphology and resistivity, the concept of gas assisted milling was introduced (this is commonly used for milling semiconductors) [117, 118]. In this gas assisted milling, a burst of the xenon fluoride (XeF_2) gas is every 10 second during milling from ~1mm top of the semiconductor surface. The purpose of this gas is to react with the sputtered atoms to make products which are more easily removed from the sidewall. In the case here, Ga (MP 29.7˚C -near liquid) is not easy to remove by sputtering, while GaF_3 (MP 880˚C) the reactant from XeF_2+Ga is easy to remove by sputtering. By using gas-assisted FIB milling, we were consistently able to achieve the smooth sidewall shown in Figure 5-12.

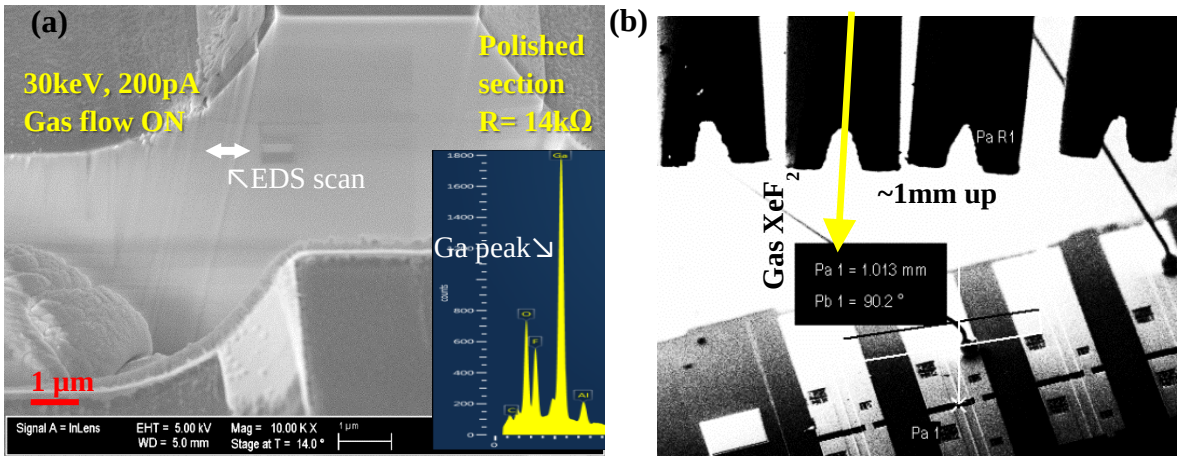

Figure 5-12: (a) XeF_2 gas assisted milling, inset: EDS scan and (b) Gas Injection System (GIS) of *Zeiss Neon* FIB machine.

The resistance of the polished section increased from ~1.6 to ~14kΩ after this gas-assisted polishing step. Finally, we use the SEM to do energy-dispersive x-ray spectroscopy (EDS) analysis (elemental sensitivity with ~1µm depth and lateral resistivity) on the surface of the polished sidewall to further understand their chemical composition. We found these sidewall regions still gallium rich, as indicated by the Ga peak in the EDS scan (see inset of Figure 5-12 (a)). This thin Ga-rich layer on this sidewall probably comes from redeposition when the polishing of the opposite sidewall. However, the presence of this layer only results in a small increase in laser resistivity and the lasers and single-mode ICL were demonstrated.

- **Other issues related to FIB**

While using FIB to mill the ICL, we experienced several issues that we completely or partially solved. One issue was the blurry image from the FIB, especially for high probe current. It was important to get reasonable, accurate image to place the FIB rectangle on a correct position of the sample to start the milling. This problem was solved by using a *Faraday cup* to measure the probe current and by repeatedly adjusting

the focus, stigmation, and condenser voltage *etc*. to optimize image quality. Another problem was an approximately 2μm offset between the actual milling location and the location set by the software. This problem was partially solved by manually placing the milling rectangle to the set location on the laser bar taking into account this amount of offset.

- **Future direction to address some issues**

The main issue that we faced during FIB milling was the sputter re-deposition of the milled atoms on the side wall surface that made this surface conductive, reducing the resistance of the lasers. We addressed this issue and solved it by using gas-assisted milling and by fine polishing the sidewall.

The degree of this re-deposition can be further reduced significantly by adopting frame-cut method [118] in which we will mill a slot along all sidewalls by etching along the perimeter of a rectangle with increasing size. As this method mills small single slices of the sidewalls in sequence (*e.g.*, one slice from one face then one from the opposing face, etc.), the possibility of debris re-deposition will be reduced significantly. However, due to licensing issues for our Zeiss-FIB software, we could not take advantage of this method.

5.4 Result and discussion

The final SEM image before and after FIB milling of the gold-ridge and narrow ridge is shown in below Figure 5-13. In this figure, the 1-5 represents the FIB cutting sequence.

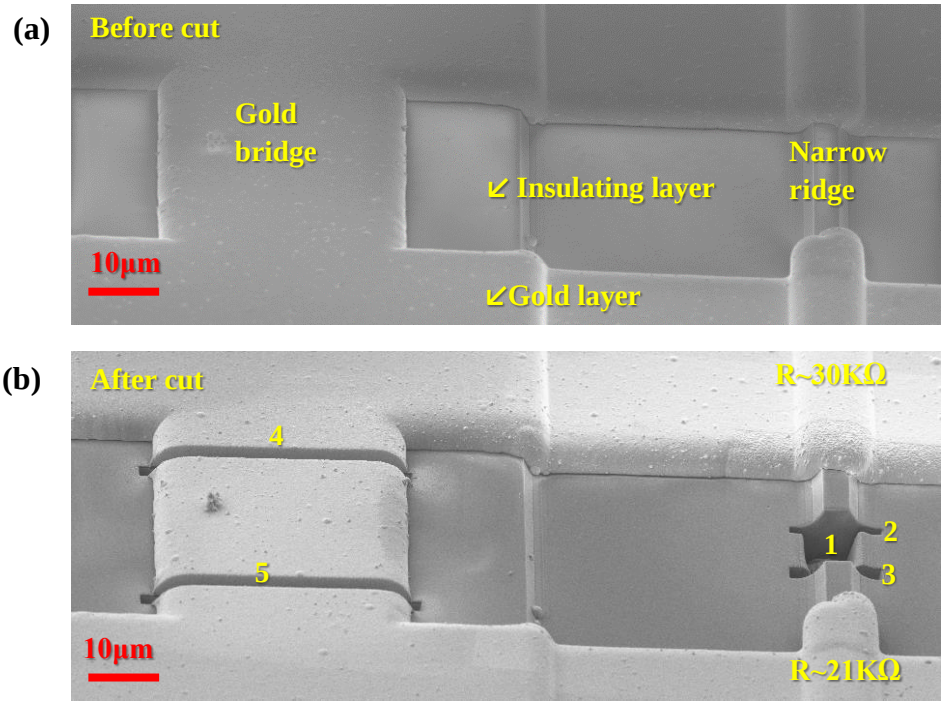

Figure 5-13: SEM images of (a) the base ICL before FIB milling and (b) the fabricated CCC after the FIB milling.

The recipe obtained for both coarse milling and fine polishing is shown in below in Table 5-1.

Table 5-1: Focused ion beam milling recipe for coarse milling and fine polishing.

Recipe	Coarse milling	Fine polishing
Cut area: narrow ridge	$10\times9\times10\mu m^3$ cut	$12\times1\times5\mu m^3$ cut
Cut area: gold bridge	$60\times2\times10\mu m^3$ cut	Not used
Current	2nA	50pA
Accelerating voltage	30keV	30KeV
Surface quality	Rough	Smooth
Milling time	Typical 30min	More than 2hours

■ I-V-L of the cleaved-coupled-cavity laser

Before FIB milling, the base ICL (cavity length: 1.5mm, ridge width: 12μm) with as-cleaved facets lased at 3.1μm in cw mode (inset of Figure 5-14) with a threshold current density of $370A/cm^2$ at 20^oC. After FIB milling, the long laser section of CCC

unit (cavity length 1mm) lased in cw mode with an increased threshold current density of 490A/cm^2 at 20^{o}C. This increase in threshold current density is mainly attributed to the larger mirror loss for a shortened cavity (from 1.5 to 1mm). As shown by the current-voltage-light (*I-V-L*) plots in Figure 5-14, we observed similar threshold current densities for the two other 1mm-long ICLs with cleaved facet mirrors fabricated from the same wafer. Thus, the quality of the FIB-milled facets on GaSb-based laser structures is comparable to cleaved facets.

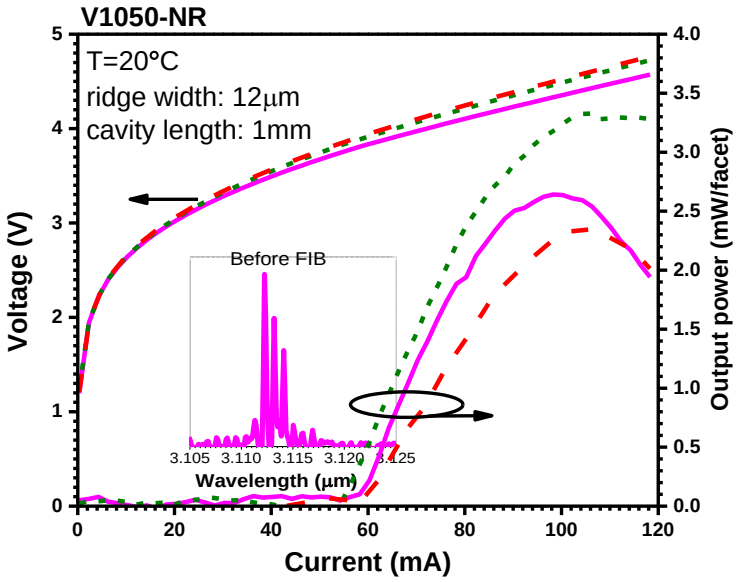

Figure 5-14: The I-V-L characteristics of the long laser section (1mm) of the CCC laser (solid lines) compared with two ICLs of the same length (dashed and short dashed lines) with as-cleaved facets [93], inset: lasing wavelength.

The two sections of the CCC were mounted on the heat-sink in such a way that the laser emission spectrum and output power could be collected only from the 1mm-long laser's outer facet. At 20^{o}C, the output power from the outer facet of the long laser section of the CCC (corrected for the window's transmission but not for beam divergence) was 2.6mW at 95mA bias current, as shown in Figure 5-14. Considering

the power loss (40%) associated with the beam divergence, the CCC laser's actual output power is estimated to be 4.3mW.

■ **Single mode operation**

The lasing spectra of the long section (LS) laser was obtained at 20^{o}C with no current applied into the short section (SS). The LS laser lased at 3.12μm wavelength with threshold current density of 500A/cm^{2}. The mode spacing was 1.35nm between two longitudinal modes, as shown in Figure 5-15 (a). The lasing spectra of short section laser was not obtained because the outer facet of this laser was oriented so that that it was not possible to collect the light from it. We expect this laser requires more threshold current density than the LS and for it to have longer mode spacing because of its smaller length.

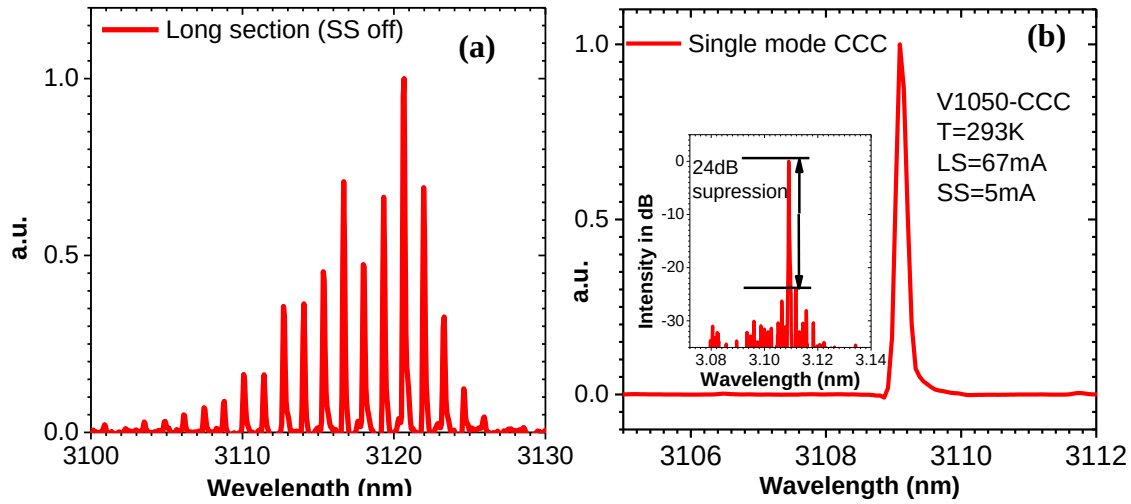

Figure 5-15: (a) The long section of the CCC is lasing at 3.12μm while the short section laser is off and (b) the single mode emission of the CCC laser. Inset: single mode suppression ratio of ~24dB.

To suppress the side modes seen in Figure 5-15 (a), dc current was applied to the short-section. This short-section acted as a passive resonator to select one single mode

of the long-section by constructive interference and suppress all other mode by destructive interference. Accordingly, the applied dc current in this section was kept slightly below threshold to avoid operational complexity. The single mode operation of the CCC laser is shown in Figure 5-15 (b) with lasing wavelength of 3109nm. The full width half max (FWHM) of this single mode is found as ~0.19nm.

The side mode suppression ration (SMSR) was obtained as ~24dB, as shown in the inset of Figure 5-15 (b). This value of SMSR was higher than 30dB reported for InP-based coupled cavity QCL devices and 43dB for GaAs-based QCLs [106, 116]. Single mode operation of coupled cavity approach was demonstrated for GaAs based THz QCLs with SMSR in the 30-40dB range [120]. However, 24dB SMSR is a reasonable value for most of the applications.

■ **Estimation of the group refractive index**

The group refractive index of laser can be estimated by the following equation if the mode spacing is known [106].

$$\text{Refractive index, } n = \frac{1}{2L\Delta v} \qquad (30)$$

where L is the cavity length of the laser, Δv is the adjacent longitudinal mode separation of the laser.

The LED spectra obtained from the long-section laser is shown in Figure 5-16 (b). In this spectrum, two longitudinal mode spacings between the adjacent LED peaks were observed ($1.326cm^{-1}$ and $1.386cm^{-1}$), where only one was expected. These different longitudinal mode spacing are probably be due to the interference of the reflected light coming from the FIB air-gap (FIB slot is ~15μm wide and an external reflective mirror can result in this optical interference). Furthermore, the increase in

temperature due to the applied dc current in the long-section can cause Joule heating and affect the refractive index [106]. The LED modes at the bottom of the Figure 5-16 (b) were simulated using $f(\lambda) = r_1 r_2 e^{(gL+4i\pi nL/\lambda)} - 1$, where r_1 and r_2 are mirror reflectivities (~28%), L is the length of the laser (~ mm) and *n* is the refractive index (3.77), which agrees reasonably with the experimental data.

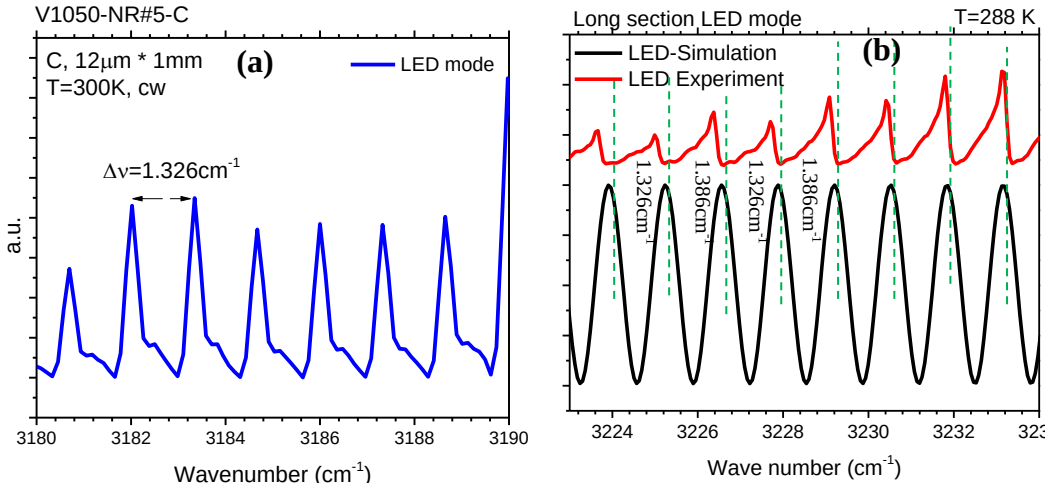

Figure 5-16: (a) LED mode spectra from a 1mm long ICL to estimate group refractive index, and (b) comparison of the LED spectra of the CCC laser with simulation.

To verify this result, we took the LED spectrum from another laser of the same size (1mm) (see Figure 5-16 (a)). The distance between the adjacent LED modes was found to be 1.326cm^{-1} which corresponds to a group refracted index of 3.77 for the ~1mm long laser. These ICLs are based on GaSb substrate and the refractive index of GaSb near 3.1μm is 3.73 [121], so this estimate of group refractive index is reasonable. This estimated refractive index was used in all the simulations in this chapter.

■ **Experimental results with simulations**

In this section, we plot the experimental results that show the single mode hops associated with increasing the applied current along with simulations of the longitudinal modes of the individual sections (see Figure 5-17). The group refractive index *n* was adjusted to make the simulated CCC modes aligned to the experimental CCC modes. This adjusted *n* correlates to the amount of heat generated inside the CCL due to the bias current applied to the short section.

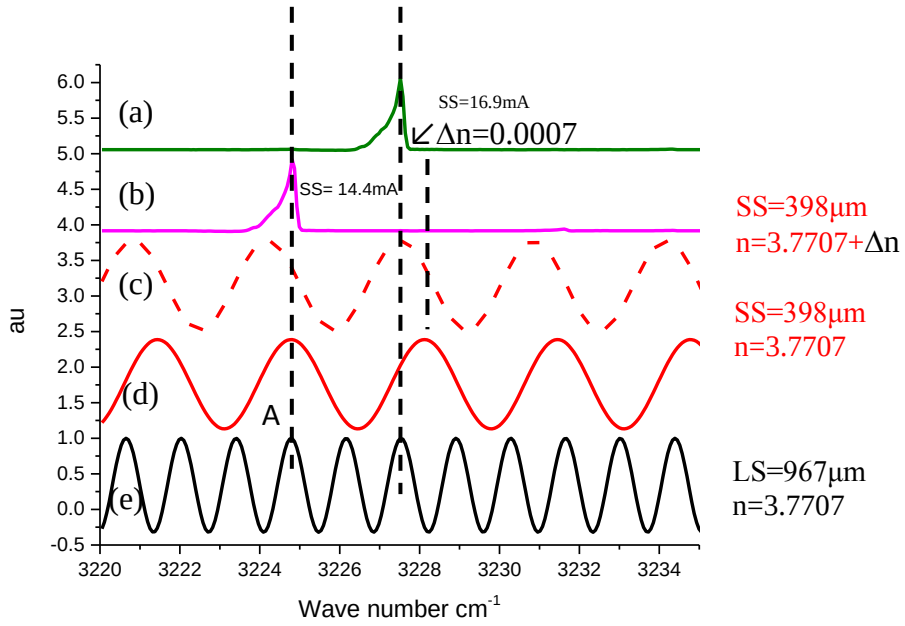

Figure 5-17: (a) & (b) Experimental lasing spectra with a single mode-hop, simulated emission from the (c) CCC laser, (d) short-section, and (e) long-section.

In Figure 5-17, the black line at the bottom of the plot represents the simulated longitudinal modes of the long laser section by using the estimated group refractive index as 3.7707, considering the laser is operating independently. Similarly, the red line above this black line represents the longitudinal mode of the short-section laser by considering it as an independent laser. At his point, the output of the CCC laser is be the

longitudinal mode that is common to both in LS and SS laser. Based on the simulation, a common longitudinal mode occurred at a wavenumber of 3224.8 cm^{-1} denoted by "A" in Figure 5-17. This simulated mode coincides with the experimental lasing mode when the SS laser was biased with 14.4mA current.

The next longitudinal mode was obtained when the bias of the SS laser was increased to 16.9mA. This applied current will generate extra carriers inside the device which will results in small change in refractive index. The red dashed line in Figure 5-17 is simulated by arbitrarily increasing the refractive index $\Delta n=0.0007$ that generates a CCC lasing mode at 3227.5cm^{-1}. This estimated Δn would be reasonable if the thermal resistance ($R_{thermal}$) and refractive index coefficient (dn/dT) remained reasonably similar with the value obtained from literature for ICL.

- **Justification of estimate of Δn**

We have selected the single mode of the CCL by varying the dc current at short-section by keeping the current constant in long-section. Increase in short section current will induce joule heating to the laser. Due to this heating the refractive index will change, and short cavity mode comb will experience a red shift (move towards short wave number). After a certain amount of red shift, it will align with a long section mode to create a resonance and a possible single mode laser will emit as seen in Figure 5-17. The expected temperature change due to joule heating at short cavity can be estimated by using the following equation [122].

$$\Delta T = R_{\text{thermal}} V_{\text{ss}} I_{\text{ss}} \tag{31}$$

where $R_{thermal}$ is the thermal resistance, V_{ss} and I_{ss} are voltage and current of the short cavity. The thermal resistance for linear mesa tripe type laser source can be estimated by a quasi-two-dimensional heat flow equation [122].

$$R_{\text{thermal}} \approx \frac{\ln\left(\frac{4h}{w}\right)}{\pi K L}, \tag{32}$$

where h is mesa depth, w is mesa width, L is length of the laser cavity, and K is the thermal conductivity of the substrate. The thermal resistance is estimated as ~9.6K·cm^2/kW for a 398μm short-laser (SS) with 9μm (from SEM image, design 12μm) active region width and 3.3μm mesa depth on GaSb (thermal conductivity of 0.32W·cm^{-1}K^{-1}) substrate. This estimated thermal resistance is reasonable because the reported thermal resistance for a 10μm narrow-ridge type-I ICL was ~8K·cm^2/kW on GaSb based substrate near 3.2μm [110]. For V_{ss}=3.5V, I_{ss}=16.9mA the temperature of the laser will increase 0.6K.

Based on this estimated thermal resistance, the refractive index coefficient can be calculated by using $\left(\frac{1}{n}\frac{dn}{dT}\right)$ where the value of dn is 0.0007 (from earlier) and dT as 0.6K. The estimated refractive index coefficient of GaSb is found as 30×10^{-5}K^{-1} which is much higher than the literature value of 8.2×10^{-5}K^{-1} [123]. This disagreement is most likely due to the underestimation of thermal resistance, but overall the agreement is reasonable. Both the lasers were biased during the CCC operation and the generated heat will be larger than the estimation. By using back-calculation, the thermal resistance of ~38Kcm^2/kW actually agrees well with the estimation.

■ Tuning of CCC

The wavelength tuning of the CCC can be obtained by changing the applied current to the long-section or short-section and keeping the bias current fixed to the other section. Usually, the longer section acts as active resonator and shorter section as a passive resonator or simply a tuner. We obtained lasing spectra by changing the current of both these sections.

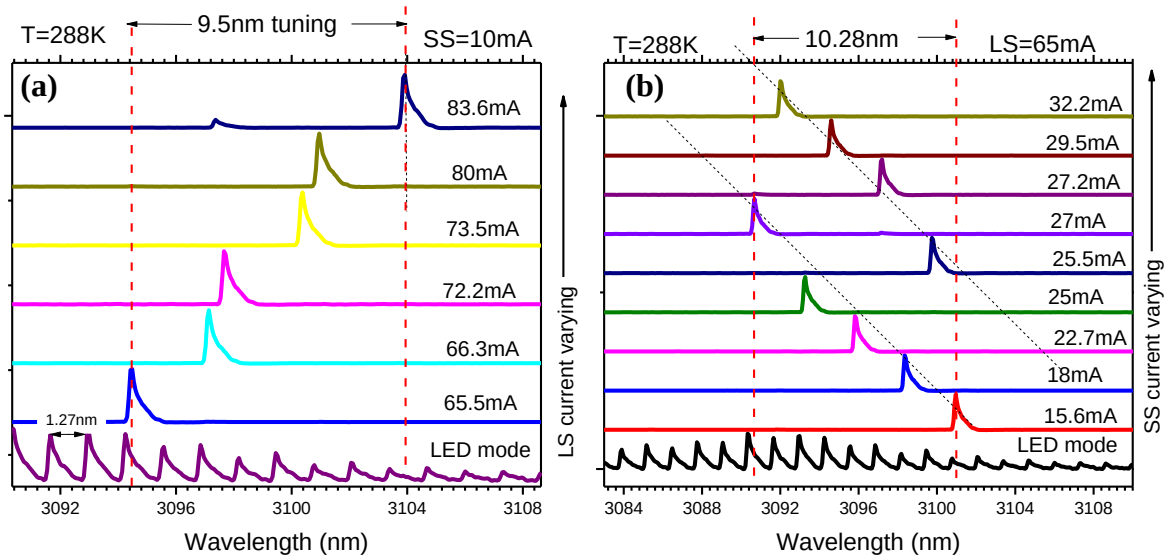

Figure 5-18: Quasi-continuous tuning spectra of the CCC laser by varying the (a) long-section current and (b) short-section current.

Figure 5-18 represents a quasi-continuous tuning spectrum of a CCC laser by varying the current of both the long and short sections. In part (a) of this figure, a quasi-continuous tuning of 9.5nm was obtained by varying the dc current of the long section from 65.5mA to 83.6mA with a fixed current of 10mA in short-section. In part (b), the tuning range of 10.28nm was obtained by fixing the current in LS at 65mA and by varying the SS current from 15.6mA to 32.2mA.

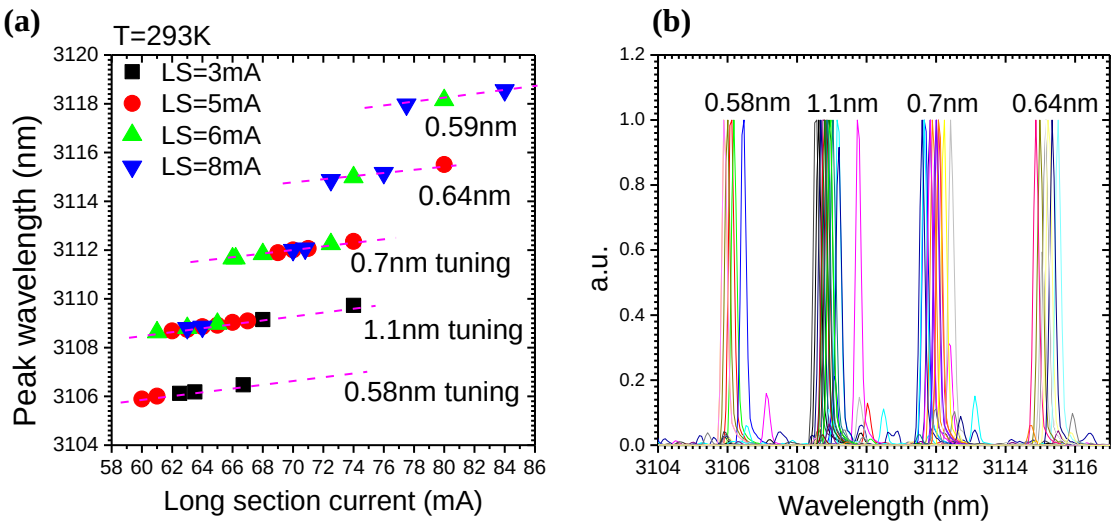

Figure 5-19: (a) & (b) continuous tuning range of the CCC laser.

Figure 5-19 (a), above, represents a mode-hop free continuous tuning of CCC by different combination of LS and SS current. The maximum continuous tuning range of 1.1nm was obtained centered at 3108.9nm wavelength for various combinations of LS and SS current. Actually, CCC ICLs have tuning limitations inherent to their operating principle as compared to distributed feedback or external cavity lasers that often have orders of magnitude larger tuning ranges.

5.5 Conclusion

In this chapter, we designed and fabricated a single-mode CCC laser that lased near 3109nm and consisted of 1mm long-section and a 0.5mm short-section lasers. These two sections were separated by a narrow slot milled using a focused ion beam. In this regard, recipes were developed to successfully mill narrow slots to electrically and optically separate the laser into these long and short sections. The reflectivity of this milled facet was found comparable to the as-cleaved facet. By using this two-section method, single-mode room-temperature ICL operation with a side-mode-suppression-

ratio of 24dB demonstrated. A quasi-continuous tuning range of 10.3nm and mode-hop free tuning of 1.1nm for various combination of long- and short-section currents was obtained. The mode-hopping for this CCC laser was simulated and is in reasonable agreement was found.

Chapter 6: High frequency operation of interband cascade infrared photodetector (ICIP)

6.1 Introduction

High-speed optoelectronic devices are in demand for the mid-IR region due to the presence of two transparent atmospheric windows covering the 3-5μm and 8-14μm spectral regions. These atmospheric windows require a high bandwidth laser and detector for free space optical communication from space to earth. In addition, some specific application such as heterodyne detection requires devices capable of high speed operation.

In the high frequency area, experimental evidence shows that an ICL can operate at frequency above 3.2GHz [124]. In this regime, the performance of a conventional photodiode is limited by their long carrier transit time because of the use of a thick absorption layer. Their high-speed operation can be achieved by reducing the thickness of the absorption region, but this achievement will come at a cost of reduced quantum efficiency and hence a trade-off is often made. However, this limitation can be circumvented by taking advantage of the cascade design scheme in ICIP devices where a small absorber thickness becomes favorable for high speed operation and cascade stages help to increase the device performance. As a result, an ICIP device has the flexibility to demonstrate high speed operation without compromising performance.

In this chapter, we investigate the high frequency response of single and multi-stage ICIP devices that have different absorber thicknesses and confirm the results with an appropriate simulation technique. In addition, we established a one-meter long free

space optical (FSO) link and characterized its transmission quality in terms of eye diagrams.

6.2 Device design, growth and fabrication

Mid-IR ICIPs operating near 4.3μm are selected to investigate the high frequency performance at room temperature. These devices have a single stage or multi-stage cascade region with absorber thickness ranging from 300nm to more than 1000nm. The absorbers are a type-II superlattice structure in which each period consists of a InAs(27Å)/GaSb(15Å)/AlSb(2.7 Å)/InSb(2.6Å)/AlSb (2.7Å)/GaSb (15Å) layer sequence. The details of this ICIP can be found in ref [125]. In a regular ICIP design, these superlattice absorbers are sandwiched between an electron barrier and a hole barrier. The device structure along with the flow of the carriers inside the device is shown in Figure 6-1.

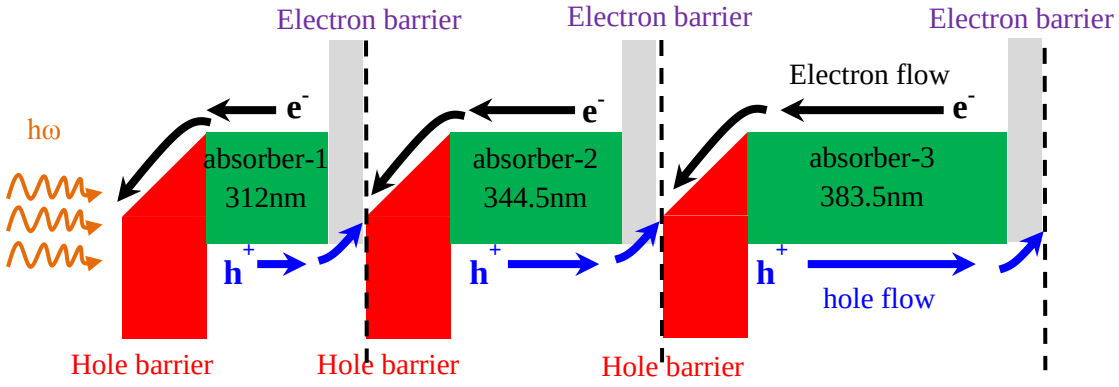

Figure 6-1: Device structure of a representative three stage ICIP. The absorbers are sandwiched between the electron and hole barriers.

All the detectors investigated in this experiment were grown by molecular beam epitaxy (MBE), then processed and fabricated at University of Oklahoma. An important step was to design a suitable mask that included the requirements for high frequency

characterization as will be described in section 6.3.3. The wafers were processed with device sizes ranging from $20\times20\mu m^2$ to $400\times400\mu m^2$. The mesa was defined by using conventional contact UV photolithography and wet chemical etching. The device was then passivated by 174nm of Si_3N_4 followed by 224nm of SiO_2. The top and bottom contacts were made from a 330nm Ti/Au layer. The insulating and metal layers were deposited by RF sputtering techniques. Finally, the devices were mounted on a chromium coated heat sink followed by wire bonding.

6.3 Experimental setup

A schematic of the high frequency experimental setup is shown in Figure 6-2. In this experiment, a super imposed ac signal was swept into the laser while the response from the detector was collected. The ac signal from 200KHz to 1.5GHz was generated by an analog signal generator and was swept with a 2ms dwell time. This ac signal then was mixed with the 200mA dc laser bias current by a bias-tee and finally fed into the laser. The temperature of the laser was kept at 293K by a thermoelectric cooler. The output of this laser at a 3.15μm lasing wavelength was then collimated by two Germanium coated lenses onto an ICIP.

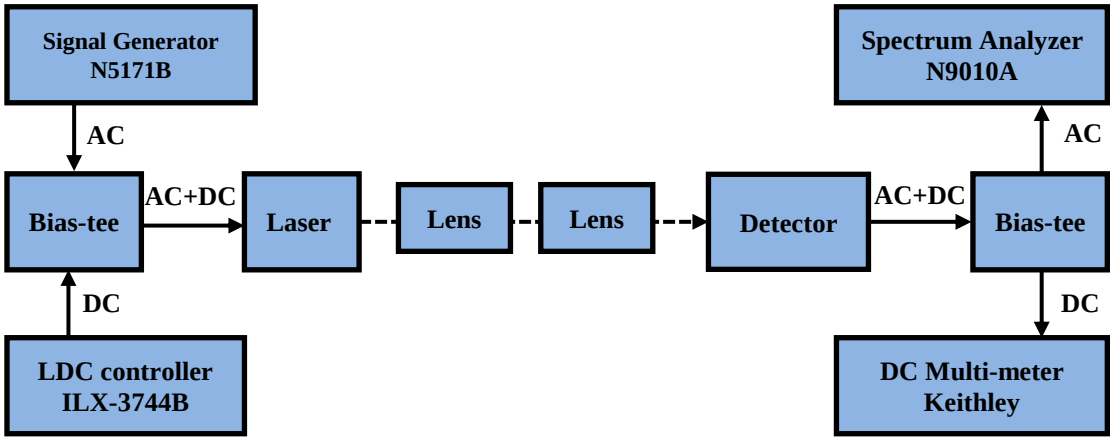

Figure 6-2: Block diagram of the high frequency experimental setup.

The ICIP responded to this combined signal and generated a mixture of ac and dc signals. This combined output from the detector was then passed through a bias-tee which separated the ac part and fed into the Spectrum Analyzer. The temperature of the detector was kept in RT which varied from 20 to 22^{o}C depending on the air conditioning set temperature of the lab. During this experiment, the entire detector holder (see Figure 6-4) was covered with a ~5mm thick metallic cylindrical-shaped shield to protect against external interference. The laser and the detector holder were properly grounded to avoid any circulating ground loop current.

In this high frequency experiment design, the most difficult part was to design the laser and the detector test station which was required to be compact and capable of reducing the influence of external interference and parasitic currents. These two test stations are described in brief in the following two subsections.

6.3.1 Laser test station

We designed a temperature controller system by using a thermoelectric cooler (TEC) that regulated the temperature of the laser from 0^{o}C to above room temperature.

In this design, the hot side of a TEC was attached to a 1.25”×1.25”×2” copper slab to remove the generated heat. The gold-plated laser heat-sink was placed on the cold side of the TEC. In both cases, a thermally conductive adhesive grease was placed underneath the TEC and the heat-sink for better heat conduction. To read the temperature of the laser, a 10KΩ thermistor was attached by a spring to the top of the laser heat sink and placed as close as possible to the laser. The schematic and a top view of the laser TEC temperature controller setup is shown in Figure 6-3.

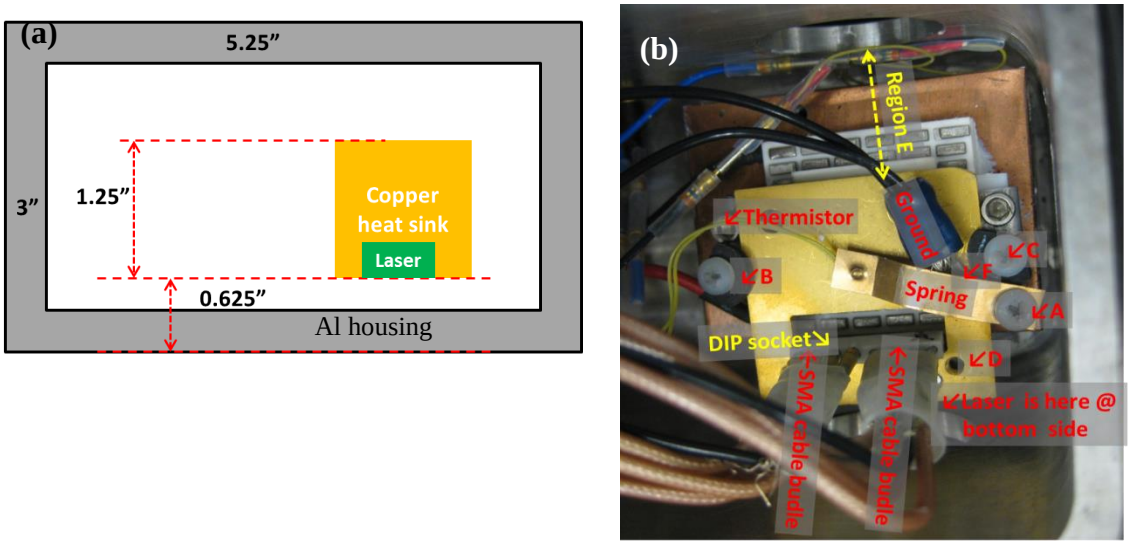

Figure 6-3: Thermoelectric cooled high-frequency test station for a laser, (a) schematics and (b) real setup.

In this setup, all the connecting screws are made from non-conductive Teflon to avoid metal interference. The grounding cables were properly soldered and connected to a single point to avoid the presence of any ground loop current. All the interconnections were made by using high frequency SMA (Sub Miniature version A) coaxial cables.

6.3.2 Detector test station

We designed a compact high frequency detector holder that held the bias-tee on top of a copper base plate and the heat sink at the bottom as shown in Figure 6-4. This copper base plate worked as a common ground for both and helped to reduce the output noise level significantly. The bias-tee was placed as close as possible to the detector to keep the length of the connecting SMA coax wire short because longer cables would generate unwanted dips in the detector output. As the output signal level from the detector was weak, the length of the cable played a key role in distorting the detector response.

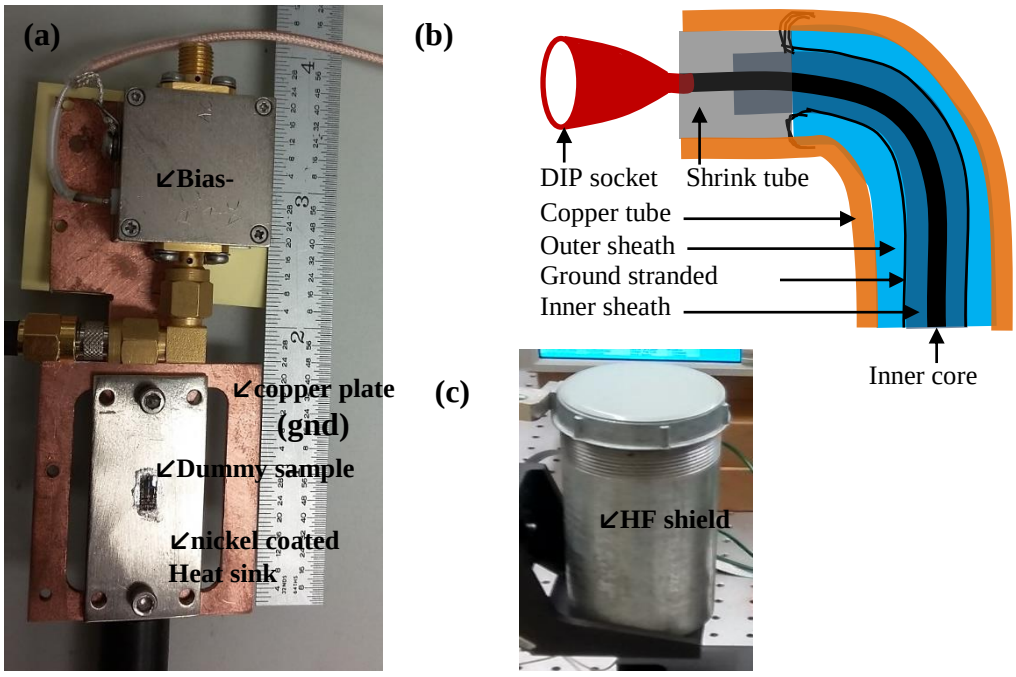

Figure 6-4: (a) Detector test station with the copper base-plate, bias-tee and heat-sink, (b) high frequency connector, and (c) ~5mm thick metal shield.

To further reduce the noise, a custom connector was designed to connect the DIP socket of the detector to the bias-tee as shown in Figure 6-4 (b). The wiring quality of this connector was very important because dangling wires and the unshielded portion

of the coax cable were vulnerable in picking up external signals. In this connector, a female DIP socket was soldered into the inner portion and a copper tube with a quarter inch bend tightly covered the outer shield of a coax cable. This resulted in a smooth, clean and low-noise output signal. In addition, a ~5 mm thick metal shield was placed to cover the whole detector test station to prevent penetration of any kind of strong external electromagnetic sources such as from the surrounding instruments. The purpose of the compactness in designing this high frequency setup is to reduce the noise level in the weak signal coming out from the detector.

6.3.3 High frequency mask design

We designed a mask as shown in Figure 6-5 to fabricate and process the ICIP that should be able to demonstrate high frequency operation. The main feature of this mask was the size of the bonding pad which was much smaller than in the regular design. As a result, it will have a small *RC* time constant that will in turn increase the 3-dB bandwidth of the ICIP. The bonding pads were $100\times100\mu m^2$ and $100\times230\mu m^2$. They couldn't be reduced further because the diameter of the gold ball that attached to the bonding pad was in the range of 70 to 80μm. Another feature of this mask was the smaller size of the device. We knew that a smaller detector can demonstrate better bandwidth by reducing parasitic capacitance. So, we kept the device size as small as $20x20\mu m^2$. The further reduction of device size would be difficult as the under-cut in the device mesa by wet chemical etching during device fabrication and processing would be severe.

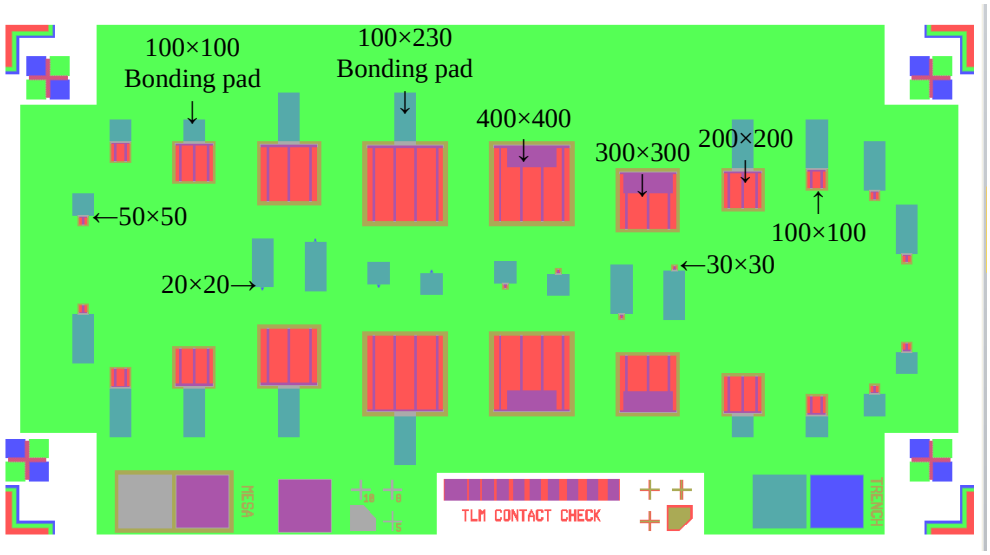

Figure 6-5: High frequency mask for the ICIP fabrication.

Table 6-1 summarizes the details of the high frequency mask. In this table, the window size means the open semiconductor area for metal fingers to collect the photocarriers. The insulating strips around this window are transparent to mid-IR light. This window is opened by dry etching the insulating layer. The gold fingers are placed on this open semiconductor window to efficiently collect the photo generated electron-hole pairs.

Table 6-1: Parameters of the high frequency mask.

Mesa (μm)	Window (μm)	# devices	# of Fingers	Finger W/L(μm)	Finger Spacing (μm)	Busbar W/L (μm)	Bonding pad (μm x μm)
20	12	4	1	4/9	N/A	12/3	100x100,100x230
30	20	4	1	4/16	N/A	20/4	100x100,100x230
50	40	6	1	8/35	N/A	40/5	100x100,100x230
100	90	4	2	8/80	42	90/10	100x100,100x230
200	180	4	3	8/170	58.5	180/10	100x100,100x230
300	270	4	3	8/260	92	270/10	100x230, on mesa & trench
400	360	4	4	8/350	92	360/10	100x230, on mesa & trench

6.3.4 Instrument calibration

We used a thermoelectric cooler, thermistor and TEC controller to regulate the temperature of the laser. The thermistor (model TCS-610) was attached on top of the heat-sink of the laser to provide a temperature feedback to the TEC controller which in return regulated the current passing though the TEC to control the temperature of the laser. The three elements were bought from three different vendors and hence their synchronization of operation needed to be adjusted.

A thermistor is an inexpensive and accurate way to monitor the temperature of a laser diode. It is a resistor that exhibits a nonlinear resistance-temperature (R-T) characteristic which can be modeled by an empirical expression commonly known as Stein-Hart Equation as written below:

$$\frac{1}{T} = A + B\ln(R) + C\,[\ln(R)]^3 \qquad (33)$$

where T is the temperature in Kelvin, R is the resistance of the thermistor and A,B,C are the Stein-Hart coefficients.

To verify the *R-T* response of the thermistor, we entered the vendor provided Stein-Hart coefficients (A=1.1235, B=2.35, C=8.4538) into our LDC controller, monitored the temperature of the laser heat sink by a general-purpose thermocouple (type-K, Chromel/Alumel), and recorded the change in resistance with temperature. In addition to this response, we recorded the variation in the temperature of the system to estimate the time taken by the system to reach a stable temperature. Both of these results are shown in Figure 6-6:

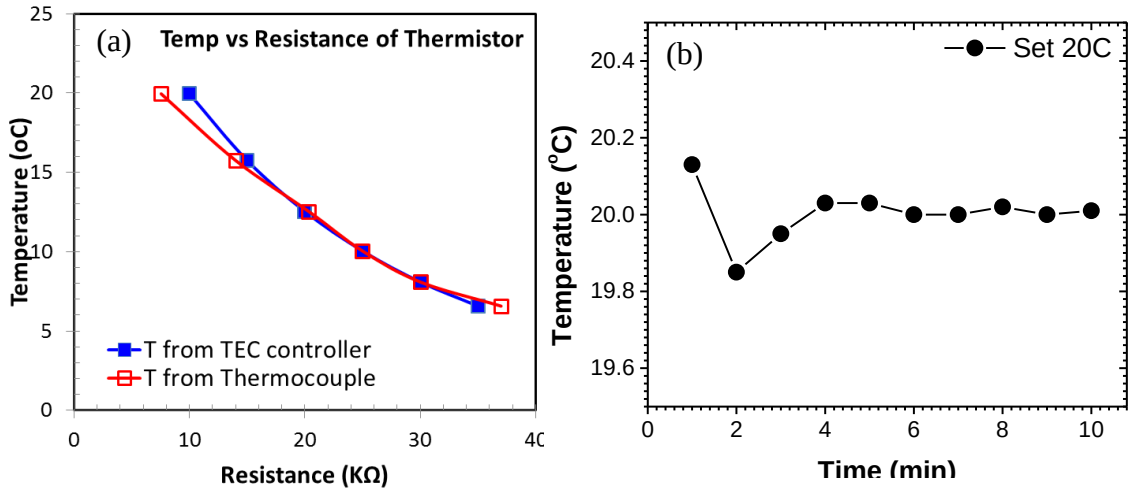

Figure 6-6 (a) Temperature *vs.* resistance measured for a commercial thermistor and (b) the stability time of the system.

It is evident from Figure 6-6 (a) that the temperature measured by both the TEC controller and general purpose thermocouple is in good agreement near our temperature of interest of 20°C. There is a variation at lower and higher temperature ends which might come from inappropriate or misplaced contact of the thermistor with the laser heat sink or from the aging of the thermocouple. After setting the temperature to 20°C, the system takes more than 10 min to stabilize and remains stable for rest of the experiment as seen in Figure 6-6 (b). This verification of system parameters validates the integrity of our experiment and results.

6.4 High frequency simulation

Theoretical analysis showed that an ISB transition based quantum cascade device can have a cut off frequency more than 65GHz [126] because of their intrinsic fast phonon assisted carrier lifetime. The carrier lifetime of these types of devices are in the range of pico-seconds which is order of magnitude shorter than the IB based

devices. The below section estimates the intrinsic frequency response of ICIP devices based on available experimental and theoretical data.

6.4.1 Equivalent circuit

To calculate the intrinsic bandwidth of IB based cascade devices, we need to build an equivalent electrical circuit model. This electrical model considers the effects of capacitance, inductance and resistance inside the device as lumped parameters. A typical ICIP and corresponding equivalent electrical circuit model are shown in Figure 6-7:

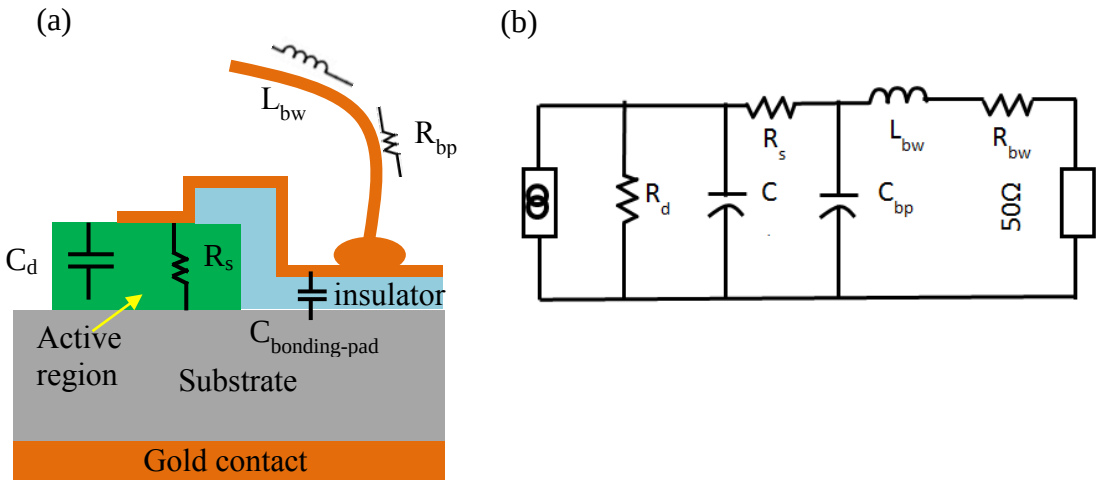

Figure 6-7: (a) A typical ICIP (not to scale) and (b) the corresponding equivalent circuit.

The ICIP will have a series resistance that originates from top contact (R_s) and gold wire bond (R_{bw}) of the detector. Usually, the device series resistance can be estimated from an I-V curve at large forward bias. The shunt resistance that is connected in parallel is termed as device resistance. The value of this device resistance at room temperature is in the range of ~KΩ and can be estimated from the slope of the I-V curve at the origin (i.e V=0). This high resistance doesn't affect the bandwidth of the device and can be considered as infinity in the device simulation. There are mainly

two sources of capacitances in an ICIP. One arises from the bonding pad of the devices. The bonding pad acts as a parallel plate capacitor with SiO_2 and Si_3N_4 as the dielectric material. Another source of parasitic capacitance originates from the cascade region of the device. This device capacitance can be considered similar to a p-n junction capacitance. Intrinsically, this device capacitance determines the speed of operation of any type of photodetector. The inductance in this equivalent circuit comes from the gold bonding wire that connects the device bonding pad and chip carrier bonding pad. The inductance of this gold wire can be estimated by measuring the length of the bonding wire and using the specification data provided by the vendor. The effect of this inductance comes into play at a certain frequency when it counter balances the capacitive effect of the equivalent circuit.

6.4.2 Intrinsic bandwidth of ICIP devices

The main carrier transport mechanisms inside the device that are related to the high-speed operation of optoelectronic detectors are as follows:

1. RC time constant of the device (τ_{rc_device})
2. Diffusion time of the carriers (τ_{diff})
3. Drift time of the carriers (τ_{drift})

The above-mentioned carrier transport mechanisms are related to the intrinsic properties of the material and hence can outline the limits of high speed operation. The contribution to the total transit time can be described by the below equation (34) [127]. The slowest term among them will define the upper limit of the high frequency operation.

$$(\tau_{total})^2 = (\tau_{rc\_device})^2 + (\tau_{diffusion})^2 + (\tau_{drift})^2 \quad (34)$$

The *RC* time constant of the device is related to device size and the dielectric constant of the constituent materials. The resistance can be considered as the series resistance (R_s) present across the device, including contact and device substrate resistances. The capacitance can be considered as a parallel plate capacitor with the area being the total active region of the detector. The expression of this device *RC* time constant can be expressed as:

$$R_s\tau_{rc\_device} = \frac{\varepsilon_o\varepsilon_r A R_s}{d} \quad (35)$$

where A is the area of the device, R_s is the device series resistance and d is the thickness of the absorber. Based on this equation, an ICIP of 20μm×20μm size with R_s=101Ω, and total absorber thickness equal to 2.496μm (each absorber is 312nm, 8 stage) will have a ~72GHz bandwidth. However, this bandwidth will be limited by the diffusion and external circuit parasitics.

6.4.3 Influence of external circuit parameters

The external parasitic components that arise from the bonding pad, insulator thickness and bonding wire length as shown in Figure 6-8.

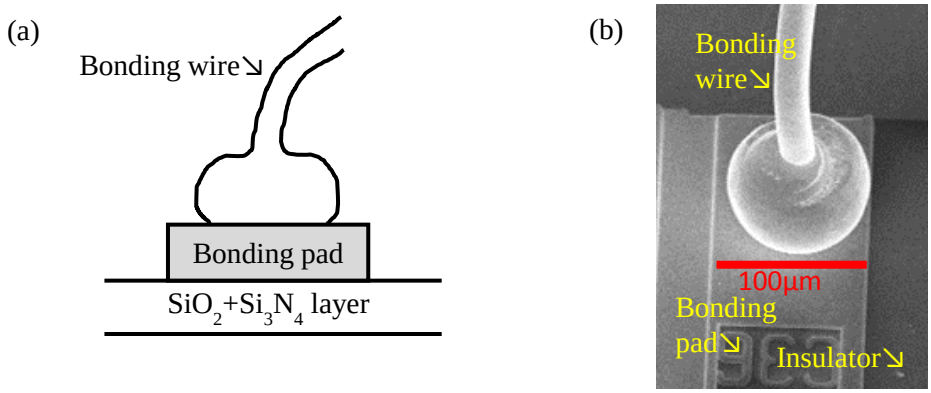

Figure 6-8: (a) Schematic of the gold bonding wire, bonding pad and insulating layer and (b) the corresponding SEM image.

The smallest bonding pad of the HF devices is a 100μm×100μm metal layer on top of a ~400nm insulating layer. This insulating layer acts as a dielectric material and the parasitic capacitance can be calculated by Equation (36). The diameter of the gold bonding wire is 1mil and a typical length ranges from 5 to 12mm. The inductance of the gold wire is calculated by the Equation (37) [128] and the resistance by equation (38):

$$C = \frac{\varepsilon_o \varepsilon_r A}{t} \tag{36}$$

$$L = \frac{\mu_0 l}{4\pi} \ln\left(\frac{4l}{r} - 1\right) \tag{37}$$

$$R = \frac{\rho * l}{A} \tag{38}$$

where ε_o is the permittivity of vacuum, ε_r is the relative permittivity, t is the insulating layer thickness, A is the area of the bonding pad, μ_0 is the permeability of vacuum, l is the length of the bonding wire, r is the radius of the wire, and ρ is the resistivity of gold ($\approx 2.44 \times 10^{-8} \Omega m$) .

The bonding pad capacitance is estimated as 1.2pF and the bonding wire inductance as 1.1nH. It was difficult to measure exactly the length of each bonding wire present in the device but an average length of ~7mm was selected for the calculation.

6.5 Results and discussion

The ICIP devices used in the high frequency experiments were fully characterized to understand the electrical and optical performance for device sizes ranging from 20 to 400μm. The zero-bias resistance and area products (R_oA) were extracted from I-V characteristics curve. The detectors made from same wafers had an average value of R_oA=0.2Ωcm^2 and a typical 20×20μm^2 ICIP had a resistance of ~35KΩ at 300K. As part of the optical characterization, the regular spectral response of a representative 200×200μm^2 device was measured at 300K under a zero bias condition using a calibrated 800K black body source as shown in Figure 6-9.

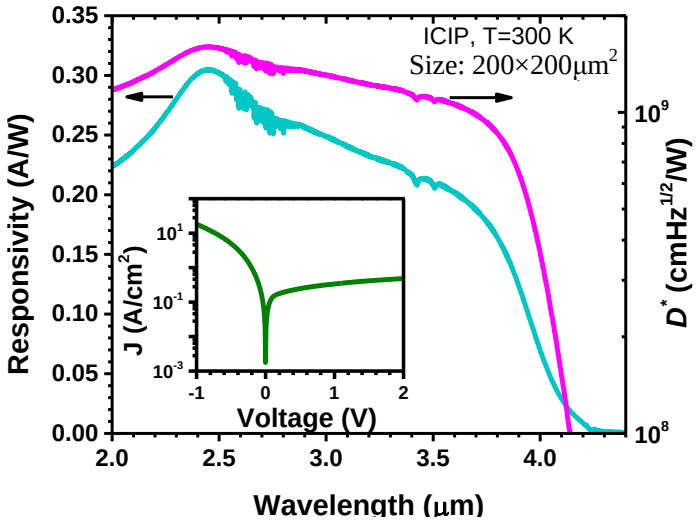

Figure 6-9: Zero-bias responsivity and Johnson-noise-limited detectivity of a 200×200μm^2 ICIP at 300K. Inset, dark J-V curve for the same ICIP at 300K [129].

This figure shows the 100% cut off wavelength of the representative device as 4.2μm which corresponds to bandgap of 0.295eV and a spectral response more than

0.2A/W at 300K. The Johnson-noise-limited detectivity of these devices reached a value higher than ~1x10^{9}cm.Hz$^{1/2}$/W. All these results are summarized in Table 6-2.

Table 6-2: Summary of the device performance of some mid-IR ICIPs at room temperature. Some of these devices were used in the high frequency measurement.

Wafer name	# of stages	λ_c (μm)	Zero-bias response (A/W)	Maximum response (A/W)	Zero-bias D^* (cm.Hz$^{1/2}$/W)	Maximum D^* (cm.Hz$^{1/2}$/W)
R146	8	4.3	0.127	-	9.67×10^8	-
R149	6	4.3	0.019	0.138 (at -1.79 V)	1.89×10^8	6.51×10^8 (at -1.79 V)
R150	3	4.3	0.029	0.174 (at -1.0 V)	2.17×10^8	6.40×10^8 (at -1 V)
R151	3	4.3	0.033	0.166 (at -1.5 V)	3.11×10^8	6.89×10^8 (at -1 V)
Y004D	3	4.3	0.255	0.261 (at 0.05 V)	1.35×10^9	1.62×10^9 (at 0.15 V)
Y005D	3	4.3	0.234	0.254 (at 0.1 V)	1.35×10^9	1.75×10^9 (0.15 V)
Y008D	6	4.3	0.216	-	1.62×10^9	2.0×10^9 (0.15 V)
Y009D	8	4.3	0.154	0.16 (at 0.3 V)	1.08×10^9	1.29×10^9 (0.4 V)
Y010D	3	4.3	0.331	0.384 (at 0.5 V)	1.72×10^9	2.01×10^9 (0.15 V)
Y007D	1	4.3	0.723	0.803 (at 0.3 V)	1.67×10^9	2.04×10^9 (0.15 V)
Y011D	1	4.5	0.191	1.058 (at 1.0 V)	8.08×10^8	1.92×10^9 (0.8 V)
Y011D	1	4.5	0.847	1.360 (at 0.1 V)	1.33×10^9	2.08×10^9 (0.1 V)
Y012D	1	4.6	0.434	1.374 (at 0.4 V)	9.05×10^8	1.89×10^9 (at 0.3 V)
Y012D	1	4.6	0.712	1.610 (at 0.1V)	1.02×10^9	2.01×10^9 (at 0.1 V)

6.5.1 Bandwidth of ICL

For the high frequency measurements, the narrow ridge type-1 ICLs from wafer V1050-NR-1 were used as the IR source. The ridge width of the laser was 20μm and the laser temperature was maintained at 293K by using a thermoelectric cooler. The emission wavelength of the laser was 3.15μm with a laser threshold current density as 405A/cm^2 at 293K. The laser power was 1.7mW/facet as measured by a power meter at a 200mA applied dc current. The L-I-V curve of this source laser is shown in Figure 6-10.

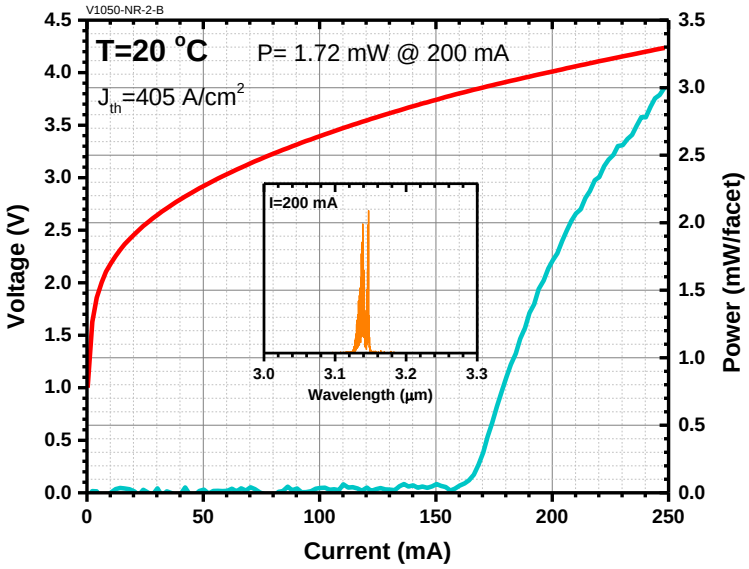

Figure 6-10: Current-Voltage-Power curve of the ICL at 20°C. Inset, lasing spectrum of this laser at 20°C [129].

The experimental work reported by the Soibel et al. [124, 130] demonstrated that ICLs are suitable for high speed operation and can be directly modulated at a frequency of 3.2GHz and above. The measurement of the bandwidth of the ICL is beyond the scope of this dissertation but we have estimated the frequency response of our ICL as shown in Figure 6-11.

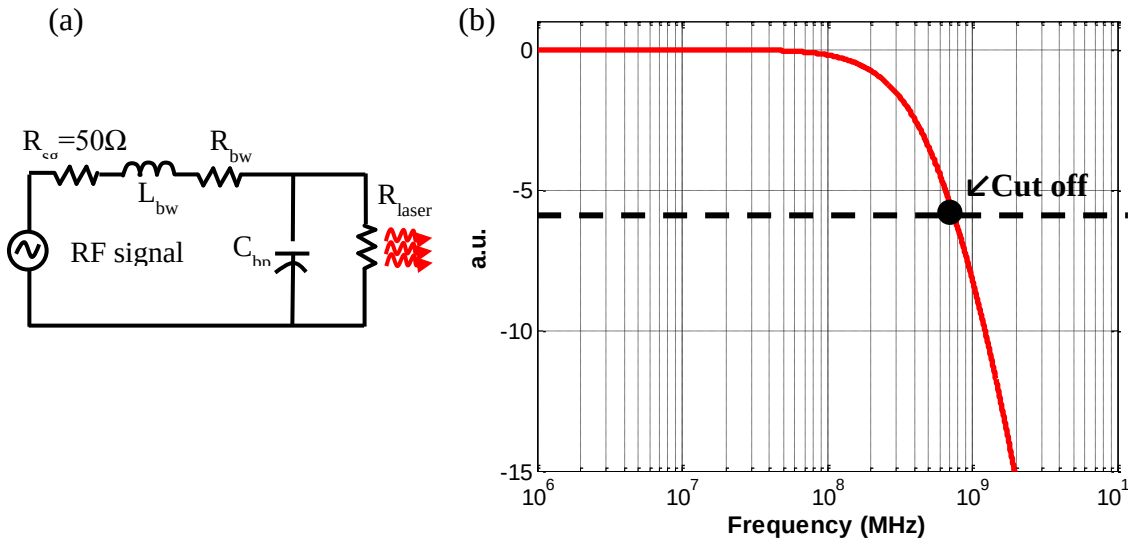

Figure 6-11: (a) Equivalent circuit model of an ICL and (b) Simulated frequency response at 300K.

In this simulation, the series resistance of the laser was extracted as 4.9Ω from the dV/dI vs. I plot at 200mA of applied current. The bonding pad of the laser was 300μm×2mm, which gives a very high bonding pad capacitance of 77.4pF. This value is much higher compared to the bonding pad capacitance as 1.1pF of our representative ICIP device. So it is evident that the high-speed modulation of our ICL is limited by the bonding pad capacitance and less affected by the bonding wire. The 3-dB cut off frequency of this representative laser was estimated as 757MHz. The detail measured and estimated parameters related to ICL are summarized in Table 6-3.

Table 6-3: Measured and simulated high frequency circuit parameters for the representative ICL at 293K.

Laser Size (μm×μm)	Laser resistance (Ω)	Bonding pad size (μm×μm)	Bonding pad capacitance (pF)	Bonding wire inductance (nH)	Bonding wire resistance (Ω)	ICL simulated bandwidth (MHz)
20×2000	4.9	300×2000	77.4	3.4	0.06	757

6.5.2 Noise reduction in HF experimental setup

In high speed semiconductor devices, usually micro-strip or coplanar transmission lines are used to efficiently route the generated photocurrent. The use of different types of transmission lines in high speed laser and detector packaging can significantly increase the high speed bandwidth by reducing the external parasitic noise [131-133]. However, we used conventional device packaging in our high speed experimental setup. As a result, the most challenging part at the beginning was to understand the noise source and then to optimize the setup to retrieve the weak signal.

In this section, we discussed the typical sources of noise that we have encountered during the high frequency experiment and the factors which we optimized to reduce this background noise. The design of the experimental setup was briefly discussed in Section 6.3. The packaging of the device started with mounting the detector wafer on a Nickel plated chip carrier by using indium solder. The devices are then wire bonded by using gold bonding wire of 1 mil diameter and approximately with 7mm length. A custom designed connector (see Figure 6-4) was used to connect the device to the bias-tee. All other connections in this setup were made through coaxial cables. In this experimental setup, the possible sources of noise that we have encountered are listed below Table 6-4:

Table 6-4: Possible sources of noise in high frequency experiment.

SL	Source of noise	Severity	Remarks
1	Length of the cable	High	Smaller length required
2	Length of the bonding wire	Very high	Smaller length required
3	Interference from chip carrier packaging	Medium	Transmission line type connectivity required
4	Dangling wires	High	Picks up outside signal
5	Impedance missmatch	High	Generate dips in output
6	Custom made coax connector	High	Reduce noise, good shielding
7	Grounding loop current	Very high	Increase noise if not properly grounded
8	Laser shielding	Medium	Generates noise
9	Detector shielding	High	Picks up surroundings if not shielded
10	Placement of the bias-tee	High	Place close to laser and detector
11	Compactness	High	Helps to reduce noise
12	Interference from instrument	Medium	Avoid placing too close to HF detector

A typical background noise before and after reducing most of these sources of noise is shown in Figure 6-12. The first part of this figure shows the background noise at different setup conditions up to a 500MHz bandwidth. Initially, the noise was so severe that the original signal was completely buried. The second part of this figure shows a clean back ground up to ~1.2GHz after reducing the background noises. The background noise was reduced by reducing the noise sources mentioned in Table 6-4. For example, the length of the connecting wires were kept as small as possible along with the bonding wires, the chassis of the instruments were properly grounded, a thick metal shield was used to cover the detector etc.

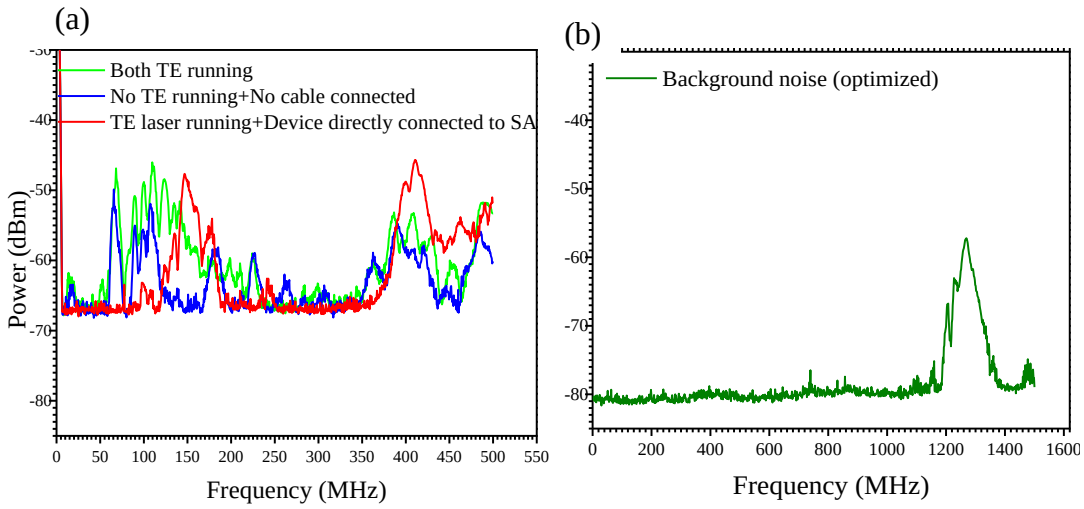

Figure 6-12: Background noises for an (a) unoptimized setup, and (b) optimized setup.

In our setup, the input impedance of the spectrum analyzer and output impedance of signal generator are 50Ω. For the ICL used in our measurements the differential resistance at 200mA and T=10°C was 4.4Ω. The ICIP's resistance (at T=27°C) was 5-35kΩ depending on its size. If the laser or detector impedance is not matched to 50Ω, reflection will occur in the coaxial cables. In addition, the length of the coaxial cable can be responsible for reflection. As a result, standing waves are generated in terms of peaks and dips in the output as seen in Figure 6-12 (a). The position and number of peaks and dips depend on the cable length and working frequency. Impedance mismatch and improper grounding can cause radiative noise at certain frequencies. This noise can be strong enough to obscure or even totally mask the detected optical signal at some frequencies. To reduce this type of noise, we investigated the possible ground loops in our setup and used metallic housings for both the laser and detector to shield the setup from the radiative noise. Alternatively, there are several well-established techniques (such as transformers and L-C networks) to

achieve impedance matching for certain frequencies. These techniques can reduce this noise and improve the system's overall performance.

To investigate the impact of compactness on device background noise, a detector wafer was mounted on a modified SMA connector as shown in Figure 6-13 (a). In this configuration, the bonding wire length was reduced to less than 1.5mm compared to the previous length of ~7mm. In addition, this setup removed the requirement of the connector mentioned in Figure 6-4 (b) because the whole setup was housed on top of a SMA connector. Furthermore, all the screws, mounting post, sample holder, base plate, sample binder etc. are replaced with PTFE (Teflon). As a result, we were able to remove the background noise above 2GHz as shown in Figure 6-13.

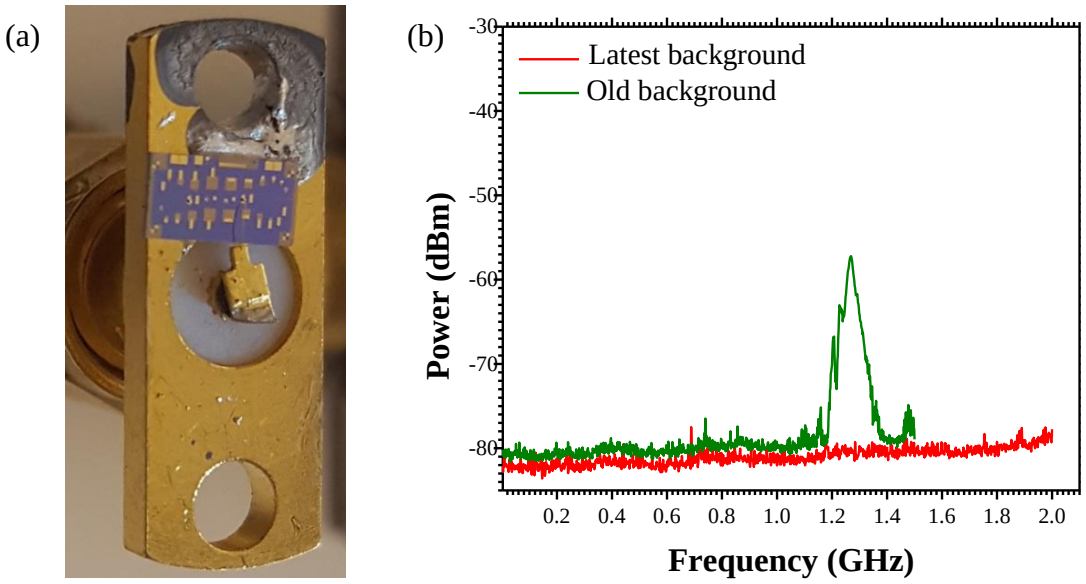

Figure 6-13: (a) Compact packaging with short bonding wire on a SMA connector, and (b) corresponding background noises.

However, we can only bond one device at a time in this setup and we were not able to observe the impact of this improvement on the device's 3-dB bandwidth. We tested only one $30\times30\mu m^2$ device that demonstrated a similar bandwidth as before.

6.5.3 Demonstration of 1.3GHz bandwidth

The frequency response of difference devices from an uncooled ICIP at room temperature are shown in Figure 6-14. All these responses were taken at a zero bias condition. The frequency dependent attenuation of bias-tees and coaxial cables were excluded from the measurements.

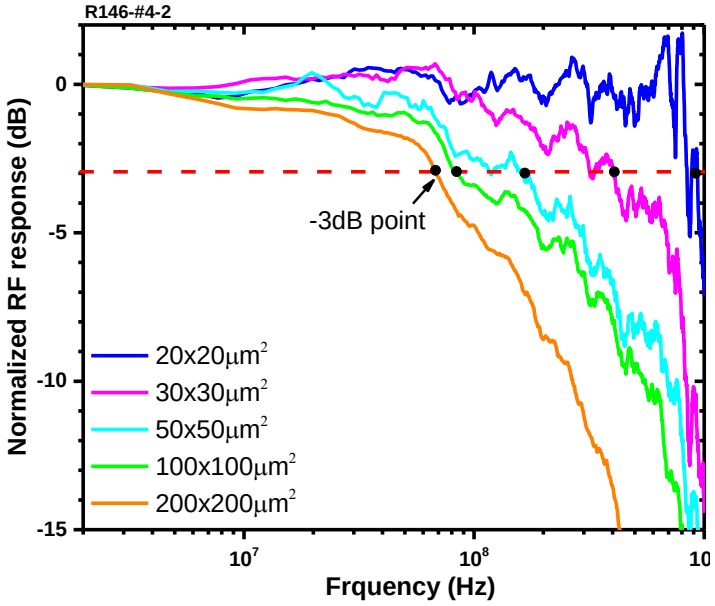

Figure 6-14: The measured frequency response of the MWIR interband cascade system using different sized ICIPs.

It is evident from Figure 6-14 that the frequency response of the devices increases with a decrease in device size. This implies that the high-speed device response is not limited by a fundamental process such as carrier transit time or device

RC constant. Rather, parasitic effects limit the performance of the detector. Hence, there is great room to improve device packaging and fabrication.

The highest 3-dB bandwidth of the system for a $20\times20\mu m^2$ ICIP device was obtained as ~850MHz at room temperature. This frequency response included the response from both the ICL and ICIP. The bandwidth of the ICL was simulated as ~760MHz by using the parameters that were directly measured. The calibrated frequency response R_{ICIP} was then extracted from the system response by using the following equation:

$$R_{ICIP} = \frac{R_{system}}{R_{ICL}} \tag{39}$$

where R_{system} is the obtained frequency response of the system, and R_{ICL} is the simulated response of the laser.

The extracted frequency response of a representative $20\times20\mu m^2$ ICIP was obtained as ~1.3GHz, which corresponds to a sub-nanosecond response time. To extract some device parameters, a fitting was carried out by solving the equivalent circuit shown in Figure 6-7. In this fitting, the resistance R_d of the ICIP was approximated as infinite because it was in the range of KΩ and had no effect on calculating the device bandwidth. All other parameters in the equivalent circuit model such as series resistance R_s, bonding pad capacitance, C_{bp}, bonding wire inductance, L_{bw} and resistance, R_{bw} were known except the device capacitance, C_d which was considered as the fitting parameter. A fitted curve of a representative $20\times20\mu m^2$ device is shown in Figure 6-15.

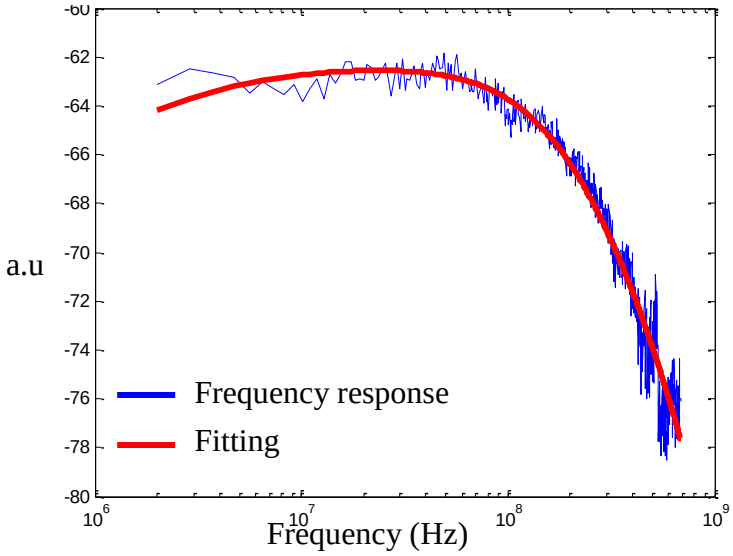

Figure 6-15: Example of fitting of a representative 20×20μm^2 device.

The measured and extracted parameters from the high frequency response of two representative devices are summarized in Table 6-5.

Table 6-5: Summary of measured and simulated high-frequency circuit parameters for two different-sized ICIPs. The ICIP capacitance (C_d) was deduced from a fit to the measurement data.

size	Resistance R_d	Capacitance C_d	Series R_s	Bonding pad size	Bonding pad capacitance C_{bp}	Bonding wire inductance L_{bw}	Bonding wire resistance R_{bw}	Simulated ICIP bandwidth	Simulated system bandwidth	Measured system bandwidth
(μm^2)	(kΩ)	(pF)	(Ω)	(μm^2)	(pF)	(nH)	(Ω)	(MHz)	(MHz)	(MHz)
20×20	35.1	1.04	101	100×100	1.1	11.1	0.44	1293	847	848
30×30	19.3	2.83	73	100×100	1.1	11.1	0.44	604	430	431

6.5.4 Free Space Optical (FSO) link

Both an ICL and ICIP can operate at room temperature and hence these optoelectronic devices together can establish a mid-IR FSO link. In this section, we will describe our high-speed mid-IR FSO link operating at room temperature and

characterization of its transmission quality in terms of an eye diagram. The setup of the time domain characterization of a FSO link is shown in Figure 6-16.

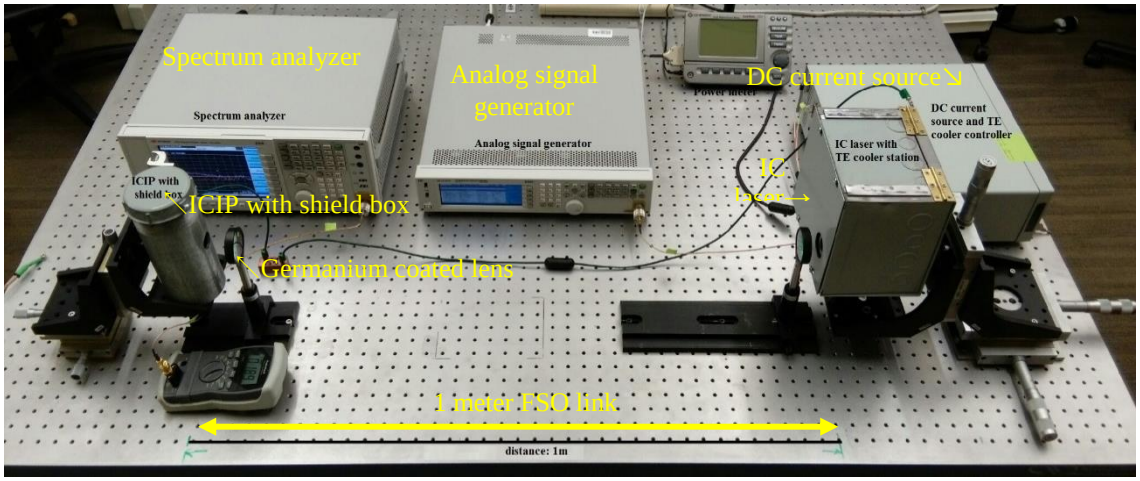

Figure 6-16: Experimental setup of a one-meter long mid-IR FSO link.

In this setup, the laser was operated at 20^{o}C with a 200mA bias current and an eight-stage detector was operated with a zero bias current at room temperature (23^{o}C). The distance from the laser and the detector was one meter and limited by the length of our optical table. The output from the laser was collimated to the detector by using two Germanium coated lenses (focal length of 5mm and 7mm) as shown in Figure 6-16. The output signal from the detector was strong and the frequency response of a representative device is shown in Figure 6-17. The presence of this strong signal implies that the length of the FSO link can be increased further without the need of a signal amplifier.

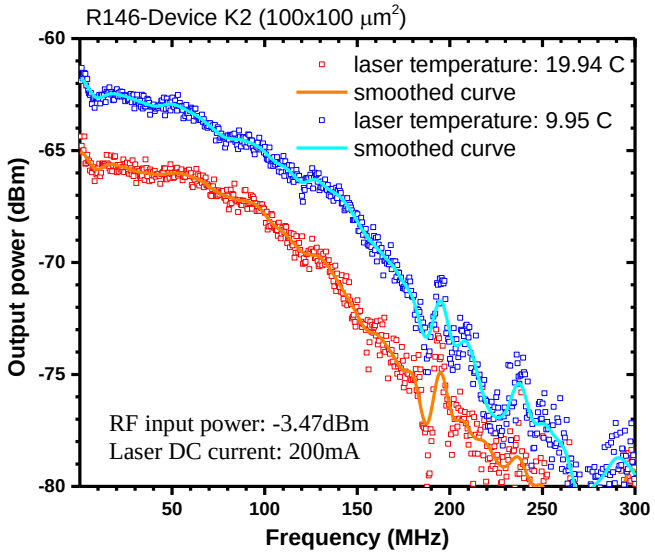

Figure 6-17: Frequency response of a representative ICIP from a one-meter long FSO link.

To identify the integrity of the optical link, time domain characterization was performed to obtain an eye diagram. The eye diagram is a common indicator of the quality of signals in high-speed digital transmission. In this regard, the analog signal generator was replaced by an arbitrary wave form (AWG) which was used to generate a pseudo-random binary sequence (PRBS). The response of the ICIP was then fed into an oscilloscope which captured the eye diagram as shown in Figure 6-18.

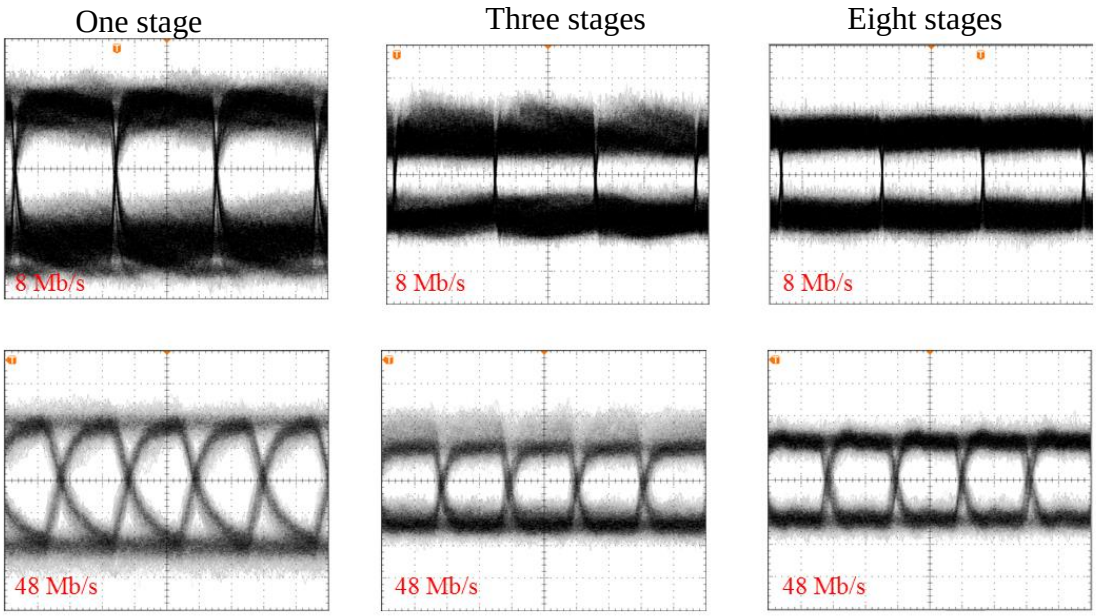

Figure 6-18: Eye diagrams for 50µm×50µm ICIPs with a different number of stages and absorber thicknesses. Each horizontal division is 40ns (top row) and 10ns (bottom row). Bit rate was 8Mb/s (top row) and 48Mb/s (bottom row) [129].

Three ICIPs were investigated to generate eye diagrams. The first detector had a single-stage absorber of 1040nm thickness. The thickness of the largest absorber was 383.5nm in the three-stage detector and 591.5nm in the eight-stage detector. The maximum PRBS signal that the AQW was able to generate was 50Mb/s.

In an ideal case, the eye diagram should look like a rectangular box. However, in reality, the pattern is distorted due to imperfect transmission of data. The openness of the eye diagram is a good measure of the link quality. Based on the frequency domain measurement, open and clear eye diagrams were expected from three and eight stage devices. It is evident from Figure 6-18 that the eye diagram is much distorted in the single-stage detectors both at a high and low bit rate compared to multi-stage detectors that have short absorbers. Although single stage detectors exhibited limited rise and fall

times for a high bit rate of 48Mb/s, the multi-stage detectors didn't exhibit any signal distortion up to this bit rate.

The high-speed performance both in the frequency and time domains is found inferior in single-stage detectors compared to multi-stage thin absorber detectors, although all exhibited similar specific detectivity in the low frequency region. This result indicates that the multi-stage short absorber detectors are suitable for high speed operation.

6.5.5 Size dependency of high speed operation

We have characterized ICIPs ranging from 20μm^2 to 400μm^2 for high frequency operation. The 3-dB bandwidths of these detectors are shown in Figure 6-19 as a function of device size.

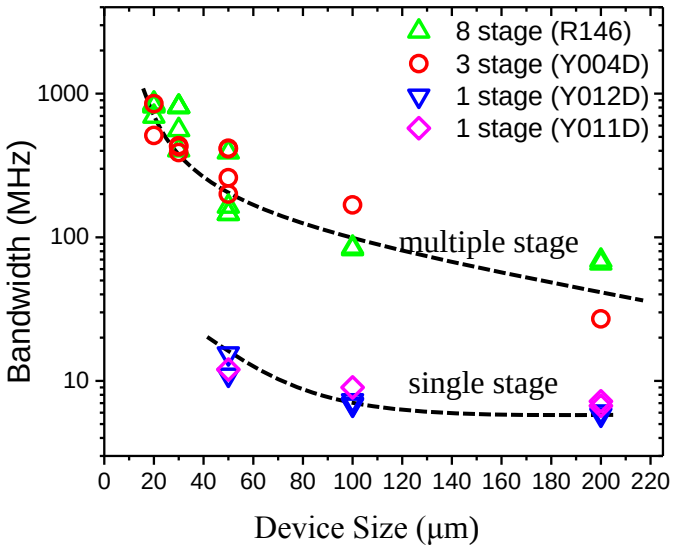

Figure 6-19: Frequency response of detectors from single and multiple stage wafers.

Form this figure, the smaller size devices exhibited higher bandwidth than the larger size devices. This size dependency of bandwidth indicates that our devices are not limited by the intrinsic carrier transit time. The external parasitic such as bonding

pad, bonding wires, and series resistance. play a vital role to limit the high-speed performance of our ICIPs. Furthermore, Figure 6-19 shows the advantage of using multiple thinner absorbers in active region as they are able to demonstrate higher 3-dB bandwidth.

The bandwidths of ICIPs were broadly distributed in Figure 6-19 especially for $20\mu m^2$ and $30\mu m^2$ size devices. These devices were investigated by scanning electron microscopy as shown in Figure 6-20.

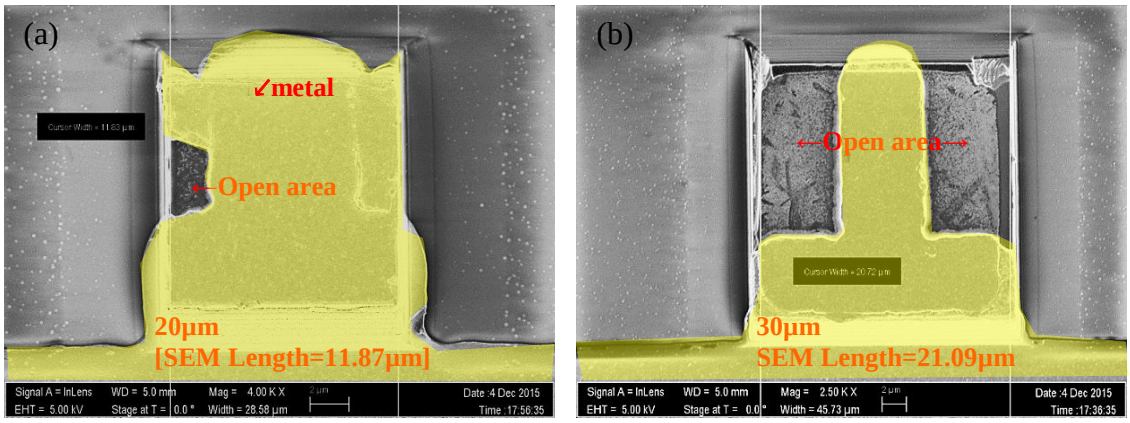

Figure 6-20: Scanning Electron Microscopy image of a (a) $20\mu m^2$, and (b) $30\mu m^2$ detectors. Yellow color represents top gold layer (original image is black & white).

This is evident from the Figure 6-20 that the size of the device becomes much shorter than its design value after the processing and fabrication of the wafers. For example, a $20\times20\mu m^2$ device is found more than 40% shorter than its original design value. Furthermore, improper metallization as seen in Figure 6-19 (a) almost covered the entire device, leaving only a very small open area for light absorption. This open area varied from device to device and hence the scattered 3-dB bandwidth. Results of SEM measurements of the devices are summarized in Table 6-6.

Table 6-6: Summary of the measurement of device length by SEM.

Actual Device dimension	Measured average Length in DIC	Measured Average length in SEM	Designed Length	% deviation
µm x µm	µm	µm	µm	%
20x20	13.63	11.87	20	41
30x30	22.49	21.09	30	30
50x50	42.57	41.60	50	17
100x100	93.59	90.44	100	10
200x200	xx	188.3	200	6

A possible reason for this shorter device length is preferential wet chemical etching that etched more than ~4.3µm on all sides of a device. This preferential etching can be circumvented by using a unidirectional dry etching method. The metallization of the device can be improved by careful alignment of the mask and by optimizing the sputter metal deposition parameters.

6.6 Conclusion

In summary, we have characterized a few mid-IR ICIPs to demonstrate the high frequency response at room temperature. In this regard, a high frequency mask was designed to fabricate devices from $20\mu m^2$ to $400\mu m^2$. A high frequency experimental setup was also designed and implemented with negligible background noise by optimizing the external noise parameters. Eliminating the background noise was a big

challenge of this experiment. These ICIP devices demonstrated high frequency response up to ~1.3GHz that corresponded to a sub-nanosecond carrier lifetime. Some important device parameters such as device capacitance were extracted from the response curve by fitting an equivalent model of the system. In addition, a one-meter free space optical (FSO) link was established. The quality of this link was measured in terms of eye diagrams. This research confirmed that the external parasitics such as device geometry, bonding pads and electrical bonding wires are the main limiting factors for high frequency operation of ICIPs rather than the intrinsic physics of the device. It is expected that the 3-dB bandwidth of an improved packaged device could increase the response to tens of GHz.

In the future, the bonding wires can be replaced by metallized hole and spring contacts [134] that will reduce the inductance. Bonding pads can be reduced by further reducing the device dimensions. The underlying insulating layer can be increased and optimized. Furthermore, a better ohmic contact layer can be grown to further reduce the contact resistance of these devices.

Chapter 7: Carrier transport in interband and intersubband based optoelectronic devices

7.1 Introduction

Interband cascade (IC) and quantum cascade (QC) devices are two major semiconductor technologies in the mid-IR region with potential applications in remote sensing, spectroscopy, medical science, and military operation. They share the same concept of recycling carriers by connecting individual active regions in cascade fashion to improve device performance. However, IC devices are based on interband transition (IB), which is relatively a slow process with carrier lifetime in the order of ~ns range. On the other hand, QC devices are based on intersubband (ISB) transition, which is intrinsically a very fast process due to fast phonon scattering. As a result, inherently QC devices suffer from higher dark current compared to IC devices. Another indirect consequence of short carrier lifetime is lower quantum efficiency in QC detectors, since the collection efficiency of photo-generated carrier is penalized. IB and ISB transitions are fundamental key feature of IC and QC based devices, respectively. So, it will be interesting and illuminating to portray this feature in terms of a common figure-of-merit in a single framework.

In this chapter, we extracted reverse saturation current density (J_o) from different IC and QC devices by fitting a simple diode equation and plotted them in a single framework to portray their fundamental difference, such as carrier lifetimes.

7.2 Carrier transport in semiconductor devices

The optoelectronics devices that we studied in this work are based on IB or ISB transition mechanisms, which are described in brief in the flowing sections.

7.2.1 Intersubband transition

ISB transition takes place in the conduction band of a quantum well in QC devices. The energy levels in the bound state can be calculated by solving Schrödinger equation with appropriate boundary conditions. The energy separation between the sub-bands determines the operating wavelength of the device and can be controlled by changing quantum well thickness. The key feature of this type of transition is very short non-radiative carrier lifetime (~ps) due to fast optical phonon scattering. The common ISB based optoelectronic devices are Quantum Cascade Laser (QCL), Quantum Cascade Detector (QCD), and Quantum Well Infrared Photodetector (QWIP). An illustrative schematic of ISB transition in the conduction band of a quantum well and the operation of a representative ISB based QCL device are shown in Figure 7-1 (a).

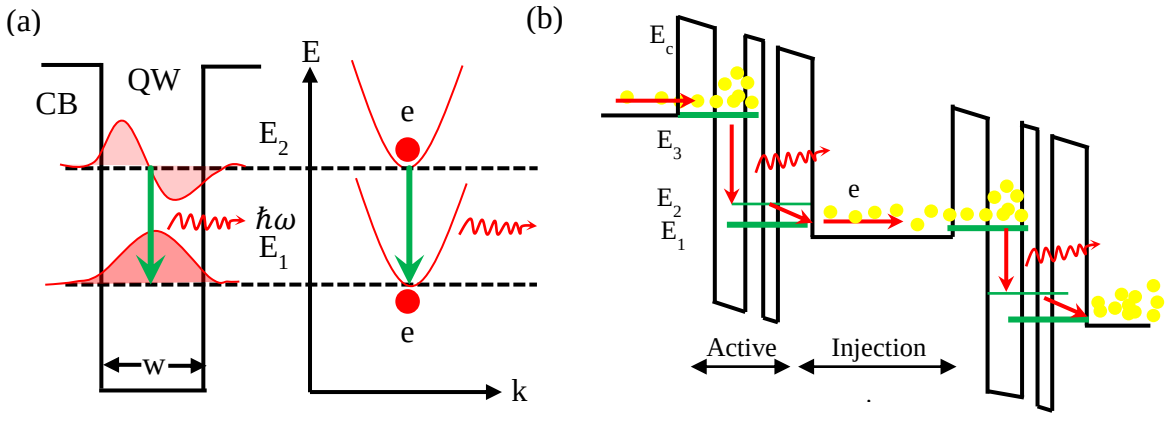

Figure 7-1: (a) Illustrative schematic of an ISB transition in the conduction band of a quantum well, and (b) the carrier transport mechanism of a QCL.

7.2.2 Interband transition

IB transition takes place between the conduction and valence bands in a quantum well structure. Depending on their design, this transition can occur in the same quantum well, or between the adjacent quantum wells. Similar to ISB transition, the energy separation between the transition bands can be engineered by changing the thickness of the quantum well; thus their operating wavelength can be tailored to a wide range. The main advantage of this type of carrier transition is that it doesn't suffer from the fast phonon scattering and the carrier lifetime is ~ns range, which is orders of magnitude longer than the one in ISB transition. Some optoelectronic devices based on IB transition are Interband Cascade Laser (ICL), Interband Cascade Infrared Photodetector (ICIP), Interband Cascade Thermophotovoltaic (IC TPV), etc. An illustrative schematic of IB transition along with the operation of a representative ICL is shown in Figure 7-2.

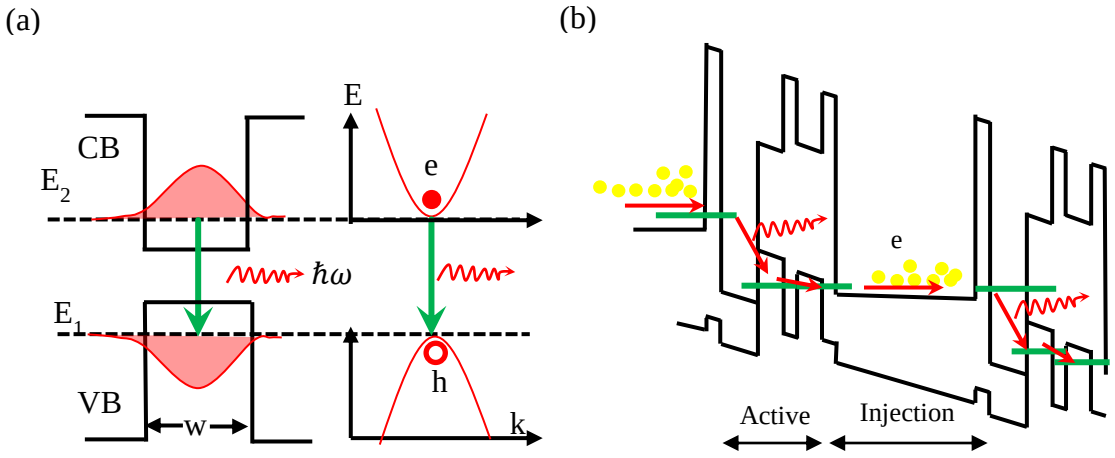

Figure 7-2: (a) Illustrative schematic of an IB transition in a quantum well, and (b) the carrier transport mechanism of an ICL.

7.3 Existing carrier transport models

In an ICIP, the dark current is mainly related to diffusion, generation-recombination (g-r), interband tunneling, and surface leakage currents. In a QCD, the sources of dark current are high electron escaping probability by thermionic emission and tunneling to adjacent QWs. There are many established methods, such as capacitive voltage measurement (C-V), capacitance deep level transient spectroscopy (DLTS), and temperature dependent current voltage (I-V) measurements to characterize carrier transport mechanism. However, there are limited qualitative and quantitative models or simulations are available [135-137] to describe the carrier transport mechanism between these two technologies. The French group [135] analytically derived a model termed as *'thermalized cascade model'* to describe the carrier transport in QCDs. They summed up all the paths that an electron can follow to cross the structure followed by relating it to device resistance. The OU group developed a theoretical framework to study the signal and noise of ICIPs [137]. This model is based on the assumption that the carrier transport is limited by the diffusion process. However, all the mentioned models are complex and very specific to particular device groups; hence, a simple and generalized model is necessary that can address all the structures.

7.4 Development of a semi-empirical model

Shockley diode equation is a universal and important equation to describe the I-V characteristic of semiconductor p-n junction given by equation (40. Unlike a diode laser, the active region of IC and QC devices are connected in cascade to recycle the generated carriers; however there is a voltage drop across each stage. Hence, this diode equation can be applied to each of this active region separately and the effect of total

cascaded region can be included by multiplying the ideal factor (n) to the exponential part of the diode equation with number of stages, N_c. In this diode equation, the reverse saturation current density (J_o) is an important parameter that is related to fundamental device parameters, such as carrier lifetime, diffusion length, and carrier mobility. This is because J_o in IC and QC devices is strictly tied to the thermal generation of electrons in the absorber region, which is exactly the reverse process of relaxation of electrons. In this model, the zero bias resistance-area-product (R_oA) is semi-empirically related to the J_o of the device. This model is developed by discussing with Dr. Rui Q. Yang in a private communication and is described below.

Shockley diode equation can be written as follow:

$$I = I_o\left(e^{\frac{eV}{nN_c k_B T}} - 1\right) \tag{40}$$

If we differentiate this equation (40) with respect to V, and set V=0 for zero bias operation, we will get

$$\frac{dI}{dV} = I_o \frac{e}{nN_c k_B T} e^{\frac{eV}{nK_B T}} = I_o \frac{e}{nN_c k_B T}\Big|_{V=0} = \frac{1}{R} \tag{41}$$

Hence, we can get a semi-empirical relation between J_o and R_oA as,

$$R_oA = \frac{nN_c \mathrm{k}_B \mathrm{T}}{eJ_o} \tag{42}$$

where J_o is reverse saturation current density, n is diode ideality factor normally ranges from 1 to 2, k_B is Boltzmann constant, e is the electron charge, A is the device area, and T is temperature. This equation (42) can empirically be applied to any IC or QC devices to estimate the J_o from their zero-bias resistance-area-product (R_oA).

7.5 Extraction of reverse saturation current density (J_o)

In practical cases, because of the effects of parasitic resistances (in shunt and series), the standard diode equation (40) needs to be modified to a more appropriate form. Actually, any quantum well based IC or QC devices can be simplified into an equivalent electrical circuit as shown in Figure 7-3. In this equivalent circuit, the series and shunt resistances are considered as a lumped parameter with an ideal diode in series.

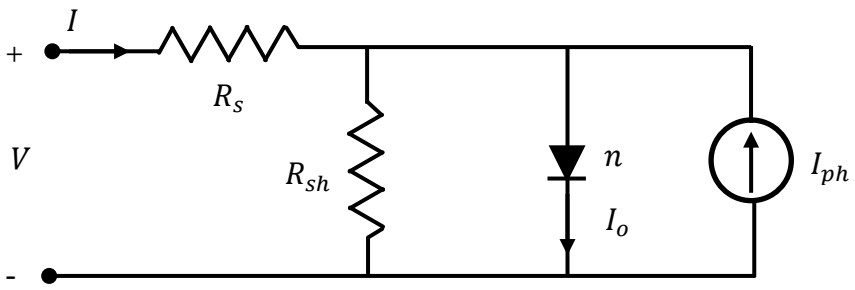

Figure 7-3: Equivalent circuit model of a typical *photovoltaic cell* structure.

The I-V characteristic of this model can be expressed by an implicit equation commonly known as *photovoltaic cell* equation [138].

$$I = -I_{ph} + I_o\left\{\exp\left[\frac{q}{nN_c k_B T}(V - IR_s)\right] - 1\right\} - \frac{V - IR_s}{R_{sh}} \qquad (43)$$

where I_{ph} is the photo current, I_o is reverse saturation current, q is electron charge, n is diode ideality factor, N_c is number of stage, k_B is Boltzmann constant, R_s is series resistance, R_{sh} is shunt resistance, and T is absolute temperature. If the shunt resistance of the device is much bigger than the series resistance, we can simplify the relation further by ignoring the voltage drop due to the series resistance. The value of the series resistance in an ICIP devices is typically less than 10Ω [139], which mainly originates

from contact resistance between the metal and semiconductor, and energy level misalignments in the device band structure. Hence, under dark condition, we can obtain a simplified equation as below:

$$I = I_o \left[\exp\left(\frac{qV}{nN_cK_BT}\right) - 1\right] + \frac{V}{R_{sh}} \quad (44)$$

This equation (44) has been applied to fit the experimental I-V data with n, I_o and R_{sh} as fitting parameters. The fitting was carried out by using *Origin Lab* software (the result is confirmed by the curve fitting tool of *Matlab* software) and the fitting result of few representative devices are shown in Figure 7-4. A suitable voltage range was chosen to best fit the equation (44). The green line in the Figure 7-4 represents experimental data and red line represents the fitted data.

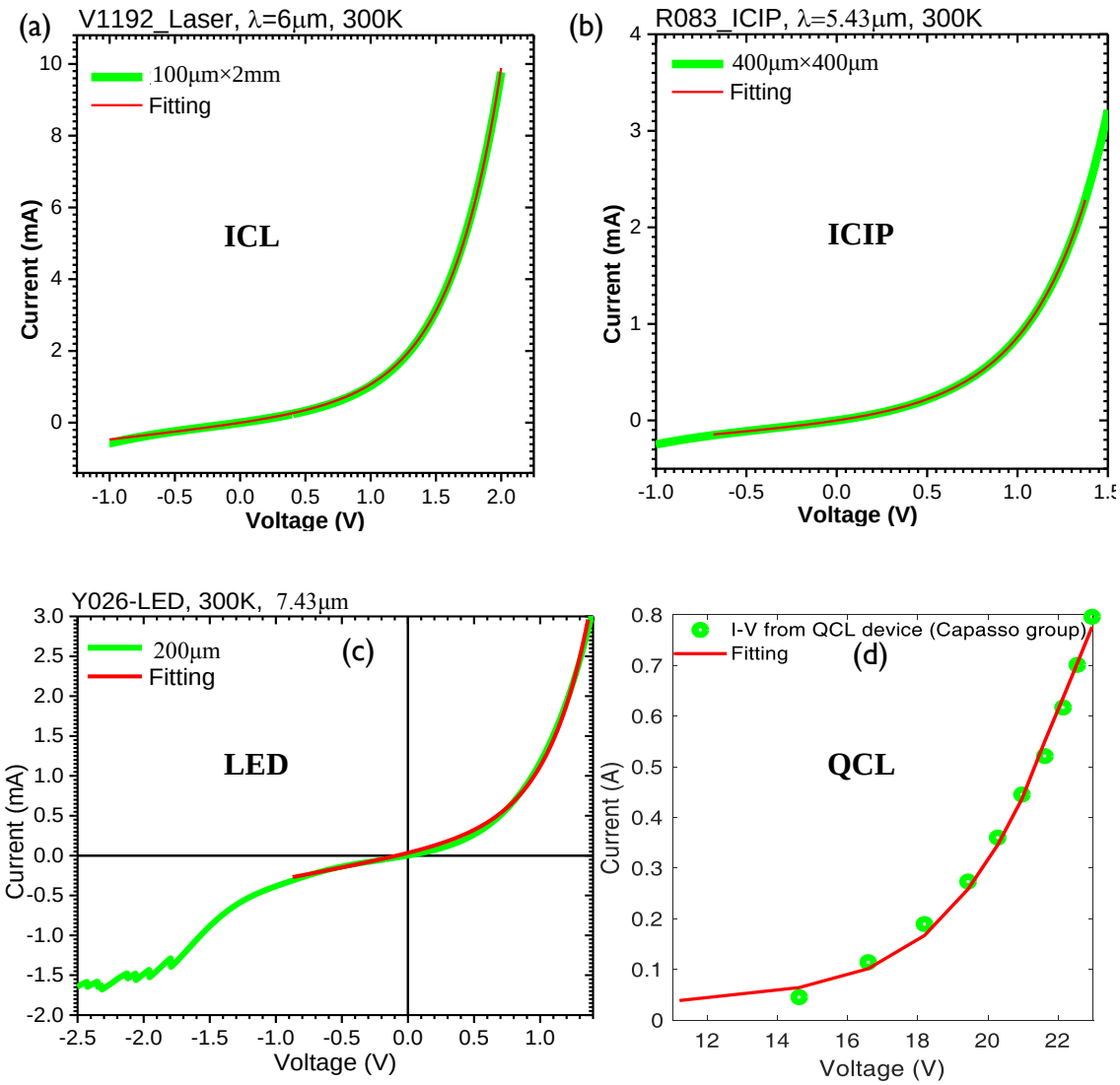

Figure 7-4: Example of fitting the equation (44) to I-V curves from the representative (a) ICL , (b) ICIP, (c) LED, and (e) QCL.

The fitting were moderate for most of the LEDs. It is worth mentioning that we observed negative differential conductance (NDC) [140] at large reverse bias (see Figure 7-4 (c) after -1.7V) for most of the LEDs especially at longer wavelengths. This is similar to what we observed in long-wavelength ICIPs, which is related to the sequential turn off of resonant tunneling of minority carriers through the electron barriers. The fitting of the representative QCL structure is moderate too and this data

was collected from Capasso's group [141]. The fitting of other ICIPs and ICLs used in this work are good and two representative plots are shown in Figure 7-4 (a) & (b).

7.6 Discussion

The I-V characteristic data were taken at 300K from IC and QC devices. The operating wavelengths were kept in the range of 3 to 8μm because the room temperature data were not available above these regions. The ICIPs had square size devices ranging from 50 to 1000μm and the ICLs had rectangular size geometry ranging from 10 to 150μm (2mm length). We found that the extracted J_o values from these IC devices were size dependent and the smaller devices had higher J_o value than the bigger devices. So, it is necessary to extract the intrinsic bulk J_o value for fair comparison.

The following section describes the procedure of extracting bulk J_o value from the size dependent reverse saturation current density.

7.6.1 Size dependency of J_o

It is well known that the devices made from III-V materials suffer from surface leakage current due to the presence of unsatisfied dangling bonds along the device sidewall, which is easily oxidized and can make a conductive leakage channel. One way to measure the surface resistivity of this sidewall is to plot the inverse of resistance-area-product (*1/RA*) to the perimeter by area (*P/A*) and then extract the slope *(inverse of this slope is resistivity)* and the intercept *(inverse of this intercept is bulk resistance-area-product)* by the following equation [142]:

$$\frac{1}{R_o A} = \left(\frac{1}{R_o A}\right)_{Bulk} + \frac{1}{\rho_{sw}}\left(\frac{P}{A}\right) \tag{45}$$

where ρ_{sw} is the device sidewall resistivity. The $\left(\frac{1}{R_oA}\right)$ vs. $\left(\frac{P}{A}\right)$ plot of a representative ICIP is shown in Figure 7-5.

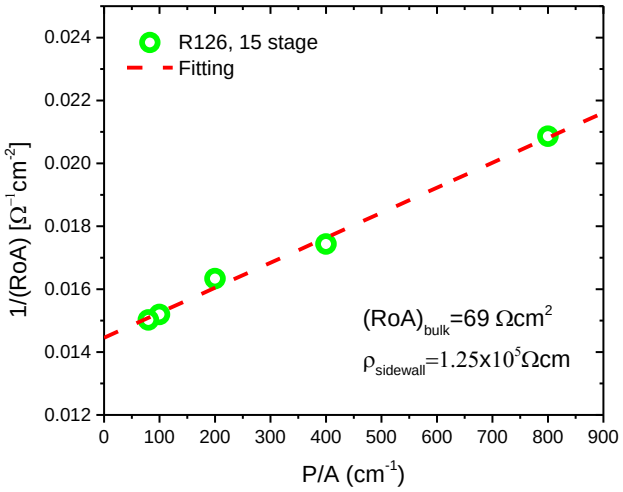

Figure 7-5: Size-dependent R_oA of a representative ICIP (wafer name, R126) at 300K.

We have found a certain degree of size dependent behavior in these extracted J_o values. So, it is necessary to eliminate the effect of size dependency to extract the J_o value for the bulk semiconductor. Analogous to R_0A, we plotted all the J_o values from the same wafer at 300K against *P/A* and extracted the J_o value for bulk semiconductor by a linear fitting as shown in Figure 7-6.

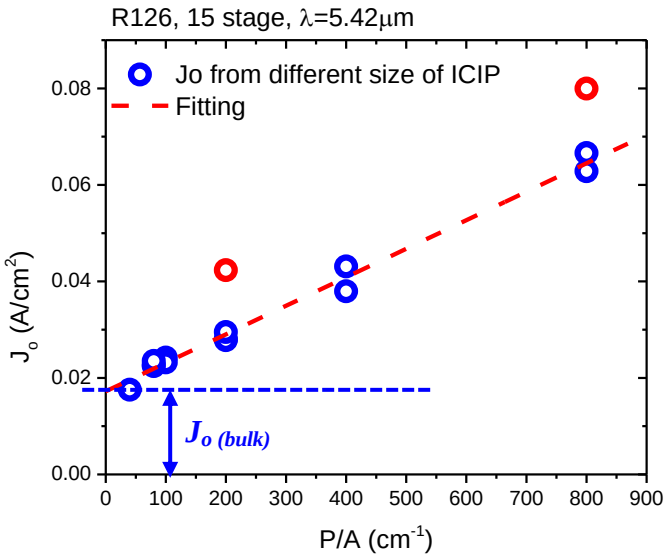

Figure 7-6: J_o values of all the devices from a representative ICIP are plotted and bulk J_o value is extracted from the intercept.

The extracted bulk J_o values at 300K from the representative devices are summarized in Table 7-1.

Table 7-1: Summary of the bulk J_o values at 300K.

Device	Type	λ (300K)	J_o (bulk)
#	#	μm	mA/cm^2
Y026	LED	7.43	186.50
Y053	LED	7.2	317.15
Y040	LED	6.25	186.53
Y052	LED	5.2	4.01
Y049	LED	3.11	-
Y041	LED	3.27	4.81
Sb0377	ICIP	3.73	0.365
V1050	ICIP	3.35	0.364
R083	ICIP	5.43	6.53
V1191	Laser	4.57	7.51
V1183	ICL	4.28	4.72
V1192	ICL	6	16.1

7.6.2 Correlation of J_o to carrier lifetime

Since the J_o value is directly related to the thermal generation of electrons, the shorter carrier lifetime would magnify itself with higher J_o. After extracting the J_o

values from different IC and QC devices, we put them in a single framework by plotting J_o values as a function of ΔE, which is the bandgap for interband devices, or the energy difference between the two transition subbands for QCLs and QCDs as shown in Figure 7-7. The red triangles represent J_o values from IC devices, which were obtained by fitting the diode equation to their respective I-V curves. The blue circles represent J_o values from QCDs at 300K, which were obtained by applying the semi-empirical model mentioned in equation (42). The green triangles represent J_o values from QCLs at 300K temperature in pulsed mode (data were collected from Faist's and Capassa's group [141, 143]).

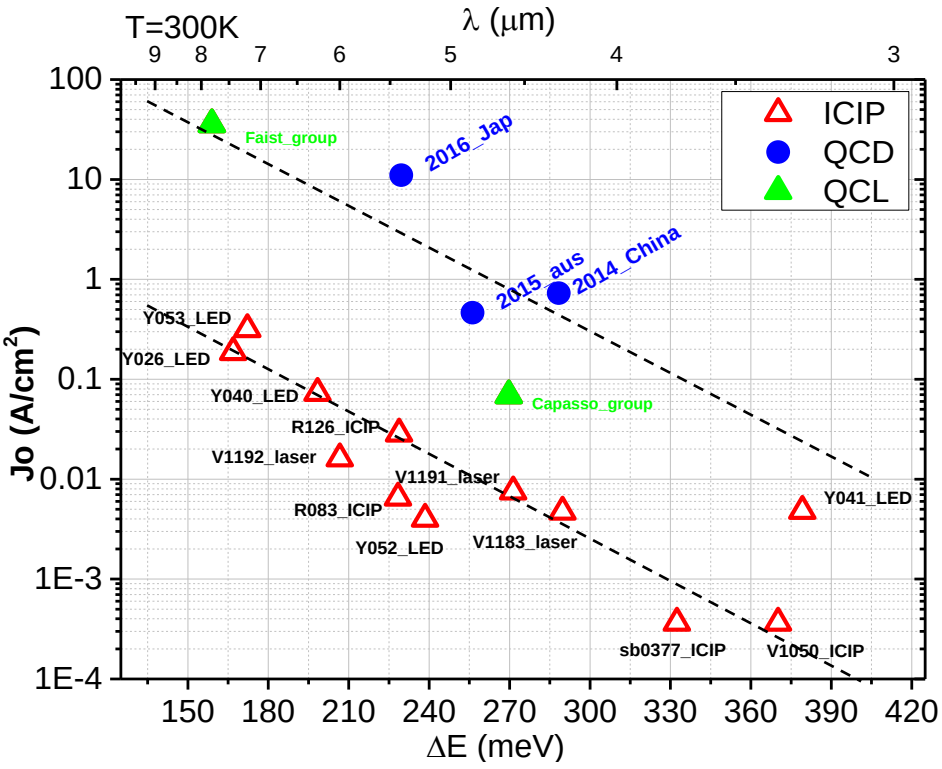

Figure 7-7: J_o values as a function of ΔE of different IC and QC devices.

Fundamentally, the devices based on ISB transition have approximately three orders of magnitude shorter carrier lifetime than IB transition based devices. Figure 7-7

shows two distinct trend lines for both IC and QC devices, which are more than two orders of magnitude apart. These two trend lines in fact portray the very fundamental key difference between IC and QC devices, such as carrier lifetime.

7.6.3 Effect of J_o on device performance

J_o value is an important intrinsic property of semiconductor optoelectronic devices which can affect the performance of IB and ISB based devices. The effects of J_o on common key figures-of-merit are discussed below.

7.6.3.1 p-n junction devices

The origin of reverse saturation current is mainly due to the diffusive flow of minority carriers in reverse direction in a p-n junction. When minority carriers are generated, the barrier potential helps them to cross the junction. The amount of the current depends on the generation of minority carriers that can diffuse across the junction. The flow of minority carriers doesn't depend on the applied reverse voltage; rather it depends on operating temperature and concentration of minority carriers. Thus, reverser saturation current represents the intrinsic property of materials. For example, the J_o value is in the order of ~nA for silicon and ~μA for germanium p-n junctions because silicon has large energy band-gap (1.1eV) compared to the energy band-gap of germanium (0.7eV). As a result, less minority carriers are thermally generated at any temperature in silicon than that in germanium [144]. Thus J_o value can be useful for selecting appropriate materials for specific applications.

7.6.3.2 Specific detectivity

The figure-of-merit that is mostly used by the detector community to characterize the performance of detectors is specific detectivity *(D*)*, which can be expressed as (Johnson limited) [145] :

$$D^* = R_i \sqrt{\frac{R_o A}{4k_B T}} \tag{46}$$

where R_i is responsivity, R_oA is zero-bias resistance-area-product, k_B is Boltzmann constant, and T is operating temperature. If we combine the semi-empirical relation mentioned in equation (42) to *D*,* we will get:

$$D^* \propto \frac{1}{\sqrt{J_o}} \tag{47}$$

The above equation expresses an important relation that indicates the influence of J_o on specific detectivity. To investigate the experimental evidence about the effect of J_o on *D*,* we selected two ICIPs from OU and one QCD from Japan group [146] with cut-off wavelength near ~5.42μm at 300K. The J_o values are extracted by fitting the modified diode equation (44) for ICIPs and by semi-empirical relation for QCD. All the results are shown in Table 7-2.

Table 7-2: Summary of experimental and extracted parameters from ICIPs and a QCD.

300K	Type	λ	Material system	Substrate	R_i	*D**	R_oA	J_o (bulk)
#	#	(μm)	#	#	mA/W	Jones	Ωcm^2	mA/cm^2
2016-Japan[146]	QCD	5.40	InGaAs/InAlAs	InP	7	2.5x10^7	0.21	11,025
R126	ICIP	5.42	InAs/GaInSb	InAs	13	2.72x10^8	4.87	17.22
R083	ICIP	5.43	InAs/GaInSb	InAs	23	4.01x10^8	4.70	22.29

Table 7-2 shows that the extracted values of J_o from ICIPs are many orders of magnitude smaller than that of the QCD. As a result, the detectivities of ICIPs become

order of magnitude higher than that of the QCD as expected according to equation (47). As an example, we can see that the difference of *D** between *R126* and *Japan group* is ~one order of magnitude ($\frac{D^*_{ICIP}}{D^*_{QCD}} \approx 10$), and the difference between their J_o values is close to two orders of magnitude ($\frac{\sqrt{J_{o,QCD}}}{\sqrt{J_{o,ICIP}}} \approx 25$). Hence, it is evident that the differences in J_o values are indicative to the intrinsic parameters which explain their difference in *D** values (IB *vs.* ISB). Due to the unavailability of room temperature data from QCDs, we investigated few QCDs and ICIPs at different temperatures and found similar results.

7.6.3.3 Open-circuit voltage (V_{oc})

Another important figure-of-merit in photovoltaic community is open-circuit voltage. It is the maximum voltage that a photovoltaic cell can deliver to the output circuit and can be written as follows [147]:

$$V_{oc} = \frac{nN_c k_B T}{q} ln\left(\frac{J_{ph}}{J_o} + 1\right) \quad (48)$$

From this equation, it is obvious that the key and the critical parameter that determines the V_{oc} is J_o. This J_o is highly dependent on temperature and band-gap of the photovoltaic cell and proportional to $J_o \propto T^3 e^{-\frac{E_g}{k_B T}}$. To investigate the amount of V_{oc} a QCD can produce, we extracted J_o values by using the semi-empirical model and J_{ph} values by $R_i P_{inc}$, where R_i and P_{inc} are the responsivity and incident power, respectively. The incident power is calculated as 13.2mW/cm^2 [148] for all the calculations based on our experimental setup to keep the extracted value under similar operating condition. The results are summarized in Table 7-3.

Table 7-3: Summary of calculated and experimental values of V_{oc} from QCDs and ICIPs.

300K	Type	λ	Material system	Substrate	J_o	V_{OC}	Remarks
#	#	(μm)	#	#	mA/cm^2	V	#
2014-China[149]	QCD	4.3	InGaAs/InAlAs	InP	727	0.6×10^{-6}	V_{oc} (calc.)
2015-Austria[150]	QCD	4.84	InAs/AlAsSb	InAs	464	1.4×10^{-6}	V_{oc} (calc.)
2016-Japan[146]	QCD	5.4	InGaAs/InAlAs	InP	11025	0.22×10^{-6}	V_{oc} (calc.)
Sb0377	ICIP	3.73	InAs/GaInSb	GaSb	0.80	1.33	V_{oc} (exp.)
R126	ICIP	5.42	InAs/GaInSb	InAs	17.22	17.4×10^{-3}	V_{oc} (exp.)
V1050	ICIP (Type-I)	3.35	InAs/GaInAsSb	GaSb	2.6	1.5	V_{oc} (exp.)

From the data in Table 7-3, it is obvious that the QCDs exhibited extremely small V_{oc} (~μV, calculated value), whereas ICIPs demonstrated very high V_{oc} (1.5V, experimental value). Hence, the generation of extremely small open-circuit voltage makes the QC devices less suitable for some specific application, such as photovoltaic cell. In general, QCDs suffer from excessive dark current due to many reasons. One reason is the fast phonon assisted relaxation from the upper state to lower state in their active quantum well. In addition, the adjacent quantum wells are strongly coupled that increase the probability of tunneling of the electrons. Hence, in practical QCDs, the amount of dark current is very high as we can see in the published literatures [146, 151-153]. This high dark current will affect the power conversion efficiency if they are made as a photovoltaic cell. The V_{oc} along with other parameters for photovoltaic cell application, such as fill-factor should be degraded significantly by the shorter lifetime. This is because most of the photo-generated carriers will relax to the ground state of the QW before being collected. Based on the above discussion, the intrinsic high J_o and lower photocurrent (reduced by excessive dark current) affect the generation of open-circuit voltage; thus QCDs are not suitable for photovoltaic applications.

7.6.3.4 Indicative to material quality

The reverse saturation current density can be used as a measure to evaluate the intrinsic material quality of semiconductor materials. The trend of J_o values shown in Figure 7-7 can be used to evaluate the material quality of IC devices. In brief, the alignment of extracted J_o values from new grown devices with this trend line should reflect their material qualities. To investigate this idea, we used few newly grown LED structures based on ternary III-V material $Ga_{0.6}In_{0.4}Sb$ on GaSb substrate as sources of J_o. These LEDs were originally grown to investigate the material quality of $Ga_{0.6}In_{0.4}Sb$ layer prior to grow laser structure. The J_o values were extracted by fitting the equation (44) along with their bulk J_o values and summarized in Table 7-4.

Table 7-4: Summary of characterization results and J_o values obtained by fitting the J-V curve from different LED structures.

Wafer	Size	R_0A	90% cutoff λ	Response	D*	R_oA (bulk)	Surface resistivity	J_o
#	μm	$\Omega.cm^2$	μm	mA/W	Jones	Ωcm^2	Ωcm	mA/cm^2
Y041 *(slow growth rate)*	200	4.25	3.27	7.88	1.27×10^8	6.29	363	18.89
Y040 *(Fast growth rate)*	200	1.87	6.25	12.06	1.28×10^8	2.67	234	57.47
Y049 *(Repeat of Y041)*	200	10.28	3.10	9.54	1.30×10^8	11	1073	0.05
Y052 *(Revised of Y041)*	200	7.16	5.20	12.92	1.90×10^8	14	274	6.48
Y053 *(Revised of Y040 with 4 sec pause)*	100	0.74	7.20	0.65	2.65×10^6	4.52	3.4	409.8

The data summarized in Table 7-4 are based on 300K operating temperature. It is evident from this table that Y052 demonstrated the highest and Y053 demonstrated the lowest *D** among all the LEDs. As mentioned earlier, *D** is a measure of signal to noise ratio. So, it is reasonable to say that Y052 exhibited the lowest noise as it exhibited the highest detectivity considering the response of these LEDs are comparable

(except Y053D). In Figure 7-7, we already showed that the J_o values extracted from the IC devices followed a distinct trend line. We plotted the J_o values of all the LEDs in Figure 7-8 as a function of corresponding energy differences to see how they fit into this trend line.

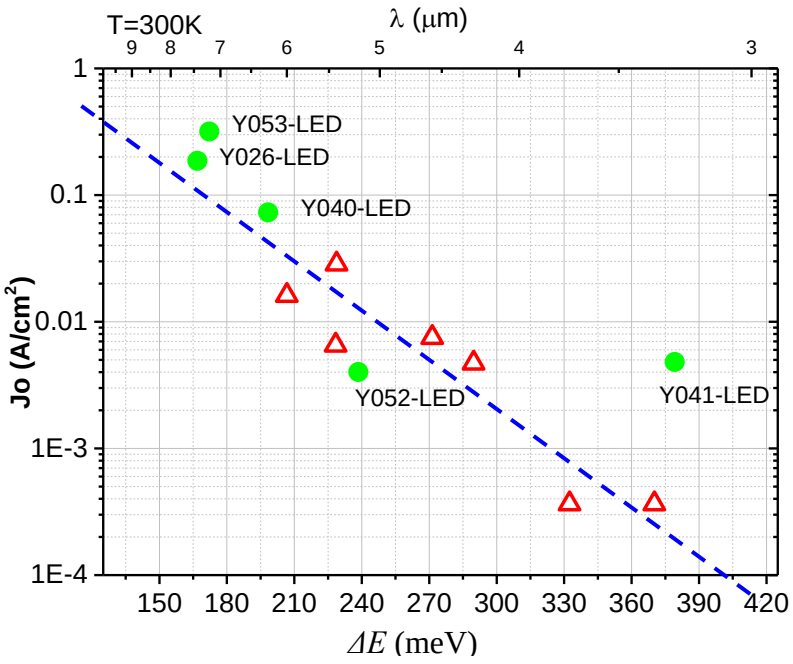

Figure 7-8: Reverse saturation current densities of LEDs are plotted as a function of their energy-band differences (band-gaps).

As expected, the bulk J_o of the best performing LED Y052 (performance is based on D*) lies below the trend line and the J_o from the worst performing LED Y053 lies much above the trend line indicating bad material quality as seen in Figure 7-8. The possible reason of higher J_o of Y053 is due to the presence of higher surface leakage current as the surface resistivity of this LED is only 3.4Ωcm; the lowest among all. Furthermore, this LED has comparatively order of magnitude higher defect density seen in differential interference contrast microscopy (DIC). The J_o value from the Y041_LED is deviated much from the trend line because it was grown with a faulty

aluminum shutter of the MBE machine and hence exhibited very high J_o. Overall, these results from LEDs and the corresponding experimental evidence further emphasize the validity of the trend line we have obtained in Figure 7-7.

7.7 Conclusion

In this chapter, we investigated the carrier transport mechanism in IC and QC based devices based on III-V materials. This study started with extracting J_o values from corresponding I-V data by fitting a modified photovoltaic cell equation. A semi-empirical model was developed that related the J_o to R_oA, and subsequently applied to QCDs. The extracted J_o values from all the devices were plotted as a function of energy difference in a single framework. Two distinct trend lines were observed; the line corresponding to IB-based devices stayed more than an order of magnitude below ISB-based devices when J_0 vs. ΔE (Energy separation) data were plotted for a large wavelength range. This plot has significant meaning from the perspective of device performance and underlying physics; it indicates the intrinsic advantages that IC devices possess over QC devices in terms of carrier lifetime. In addition, the consequence of this J_o on important figures-of-merit, such as specific detectivity, open-circuit voltage, material quality, etc. were also investigated for IC and QC based devices.

Chapter 8: Summary remarks and future directions

In this final chapter, I summarize each Chapters 2 through 7 and I discuss the future directions associated with the topics in each Chapter. This work contributed to different aspects of the IC device family and a brief summary is given below:

- Developed an ICL beyond 6μm emission with a record high performance in collaboration with the National Research Council (NRC), Canada.
- Studied the far-field laser beam profiles of ICLs.
- Designed and optimized a high-speed modulation measurement setup that demonstrated first GHz operation of ICIPs.
- Successfully implemented a one meter long mid-IR free space optical (FSO) link for data communication.
- Modeled, designed, and implemented a Cleaved-Coupled-Cavity (CCC) Laser, using Focused Ion Beam (FIB) etching, to obtain a single-mode emission.
- Investigated the carrier transport mechanism between interband (IB) and intersubband (ISB) based devices, the two major semiconductor technologies in the mid-IR region, by developing a semi-empirical model.

8.1 Summary

The interband cascade family of optoelectronic devices include interband cascade laser (ICL), interband cascade photodetector (ICIP) and interband cascade thermophotovoltaic (ICTPV) devices, which are able to cover the complete mid-IR spectral region. These devices take advantage of type-II broken bandgap alignment, cascade architecture and interband carrier transition mechanism to demonstrate high

performance and high temperature operation [16, 154-156]. ICLs have been investigated for the past 20 years, whereas the other two devices are in their early phase of research and development.

For lasers, the major part of this research is associated with the development of efficient ICLs to the longer wavelengths based on plasmon waveguide and the projected enhancement of performance, such as low threshold current density and room temperature operation, as well as single mode emission and laser beam optics for recently fabricated ICLs. This research also involved more fundamental issues, associated with the comparison of the carrier transport mechanism in interband vs. intersubband based optoelectronic devices. Another objective of this research is to extend the functionality of ICIPs in the field of high speed communication including the establishment of a one-meter long free-space optical communication link.

In this dissertation, the first two chapters provide an introduction, back ground and motivation, theory of ICLs, their operation principles, major challenges, and key figures-of-merit to evaluate the performance of ICLs, their beam optics, coupled-cavity laser, and high frequency operation of ICIPs.

The performance of plasmon waveguide ICLs (λ=4.6 to 6μm) on InAs substrate is analyzed and discussed in Chapter 3, which is one of the major parts of this dissertation. In this regard, few samples were designed based on the performance of previous lasers and grown at the National Research Council of Canada. These lasers are extensively characterized; their performance analyzed and compared with our previous results and state-of-the-art values. Notable performance improvements are achieved in terms of threshold current density and room temperature operation. At 300K, the lowest

threshold current density of 333A/cm^2 is achieved from a broad-area laser lasing at 6μm in pulsed mode. This is 50% lower than the current state-of-the-art value [16]. A narrow-ridge laser made from the same wafer also demonstrated continuous wave room temperature (293K) operation beyond 6μm with low input power consumption of 0.66W. This is a significant improvement for long wavelength emission in the mid-IR spectral region. Lasers with emission near 4.3 and 4.6μm were also investigated and their performances are found comparable to our previous results. The reason for this lack of improvement may be due to the unoptimized device design along with fabrication and packaging issues. There is still room for improvement in these ICLs in managing heat generated in the active region which is reflected in terms of their high thermal resistance, low characteristic temperature and thermal roll-over in *L-I* characteristics plot. These issues can be improved by employing epi-side down mounting, as well as further improvements in laser fabrication and packaging. Overall, the narrow-ridge lasers suffer from significant current leakage (50 to 150%) through their sidewalls, which is reflected in their high threshold current density in pulsed mode. The influence of the sidewall leakage current can be reduced by improving the existing passivation quality, or by introducing new passivation schemes. This analysis will help design InAs-based long-wavelength ICLs and achieve low threshold current and high temperature operation well beyond 6μm emission.

The study of laser beam optics is discussed in Chapter 4. It is very important to know the quality of the laser beam for many applications, especially with fiber coupling instrument in optical communication where poor laser beam may increase the bit error rate. As discussed in Chapter 3, our recent lasers demonstrated record low threshold

current density compared to the state-of-the-art values with room temperature operation beyond 6μm. Thus, there is a strong motivation to study and then improve their beam optics, especially in the far-field. Previous far-field profile studies were carried out by our group at cryogenic temperature (80K) at similar lasing wavelengths (5.6μm) [32]; however beam profiles at room temperature was not reported. This study evaluates the far-field beam profile of recent high performance ICLs operating at 300K. The far-field beam profiles are obtained both in growth and lateral directions and their shapes are in agreement with predictions based on our previous studies. The quality of the beam is estimated in terms of M^2 (beam-quality factor) and compared with our previous studies. Near diffraction-limited beam quality with single vertical mode emission is obtained from all of the lasers along growth direction with M^2 values ranging from 1.2 to 1.35 at 300K. Multimode lasing emission is obtained along the lateral direction, which is expected because the lateral length is much bigger than the lasing wavelength and the quality of the beam is not as good. This result is comparable to our previous studies at 80K [32].

Single mode lasing emission is obtained by fabricating a cleaved-coupled-cavity (CCC) ICL and discussed in Chapter 5. Single mode lasing emission with narrow line-width is very important for many applications especially in high resolution spectroscopy, where single mode with narrow line-width is essential. In our previous research, distributed feedback (DFB) ICL was used to generate single mode lasing emission at 4.5μm up to 180K with side mode suppression ratio (SMSR) of ~30dB [99]. The operation of this DFB laser is more complicated and required a mask for fabricating the top grating and involved dry etching or electron-beam lithography techniques. This

work used a focused ion beam (FIB) to fabricate a less complicated CCC laser [35, 100] allowing single mode emission at room temperature. In this regard, two FIB recipes (involving XeF_2 gas assist) were successfully developed for milling both the electroplated gold and the III-V semiconductor epilayer to form the CCC laser. From this fabricated CCC ICL, single mode emission at 3.11μm is obtained at room temperature with SMSR of ~24dB with output power of 2.5mW. This SMSR is good enough for many applications, where ~20dB is a typical requirement. The continuous tuning range obtained from this CCC ICL is less than 1 nm, which is fundamentally limited by mode hopping between adjacent modes in Fabry–Pérot cavity; however this result is encouraging considering its simple operation and low power consumption.

High speed operation of interband cascade photodetector (ICIP) is investigated and a one-meter long free space optical (FSO) link is established as discussed in Chapter 6. ICIPs have demonstrated high temperature operation with large device resistance and detectivity and short response time that is expected shorter than ns, but high frequency operation of ICIPs has not been explored until this work [157-161]. The availability of ICLs and ICIPs in mid-IR region and their room temperature operation is the motivation for this work. The author of this dissertation made major contributions in designing and establishing this high frequency experimental setup along with analysis and simulation of the measured data. There were significant challenges to reducing the background noise, associated with instrumentation and the surroundings, necessary to detect signals at high frequencies. A 3-dB bandwidth of ~850 MHz from this system under direct frequency modulation was obtained at room temperature. The high frequency characteristics were analyzed by developing a circuit model. The

extracted 3-dB bandwidth for an uncooled ICIP is found to be ~1.3 GHz, signifying the great potential of interband cascade structures for high-speed applications. The bandwidth of the ICIP was found to be limited by the external circuit parameters, especially the bonding pad capacitance. The quality of data transmission of this system was qualitatively evaluated by establishing a one-meter long free space optical (FSO) link. A strong signal was received by the ICIP and a clear eye-diagram demonstrated in response to a pseudo random bit sequence (PBRS) up to the frequency limit of the instrument used (48 Mbs). This result is encouraging considering it as a first demonstration of optical link at room temperature using a laser and detector from the interband cascade family.

The final part of this dissertation (Chapter 7) is of a fundamental nature. The objective of this work is to contrast the carrier transport mechanisms between interband (IB) and intersubband (ISB) based devices, the two major semiconductor device technologies that take the advantage of cascade connectivity. IB- and ISB-based devices are fundamentally different in terms of transition mechanism that reflected in their carrier lifetimes, with IB carrier transitions have order of magnitude longer lifetimes than ISB carrier transitions. There are a few models available to explain the carrier transport mechanism of each technology individually [135-137] , but no single model that can address both transport mechanism. This work starts with searching for a common figure-of-merit that reflects their fundamental key differences in a single framework. To this end, reverse saturation current density (J_o) is selected as a fundamental device property in common to both of the device groups and capable of addressing other fundamental properties. J_o values are extracted by fitting a modified

photovoltaic-cell equation to current-voltage (*I-V*) plots. A semi-empirical model is developed that can relate J_o to the device resistance allowing its value is calculated where *J-V* plots are not available. Finally, J_o is plotted as a function of bandgap for IB based devices, or the energy difference between the two transition subbands for ISB based devices for a wide energy range. Two distinct trend lines are observed, where the trend line that represents IB devices fall an order of magnitude below than that of ISB devices, which is due to their fundamental difference in carrier lifetime (ns *vs*. ps, respectively). This plot is a *new*, different perspective of viewing these two groups of devices, where their fundamental key difference of carrier lifetime is reflected in terms of a common figure-of-merit. The consequence of these J_o values on device performance is also discussed. It is found that this trend line is indicative of material quality by comparing our recently grown light emitting diode (LED) structures.

8.2 Future directions

Interband cascade lasers (ICLs) have demonstrated room temperature operation with record low threshold current density and low input power consumption [16]. In the discussion section of Chapter 4, a few issues are pointed out that need to be addressed to achieve further improvement on device performance. One issue is related to the substantial current leakage through the sidewall of the mesa, which becomes severe for the smaller devices. The amount of leakage in the narrow-ridge lasers is found to be in the range of 50 to 150% more than that in broad-area lasers. This leakage keeps the smaller lasers from outperforming the broad-area lasers at high temperature in pulsed mode. This issue can be addressed by: (1) improving the quality of the mesa sidewall by introducing dry etching techniques in place of the wet chemical etching currently used,

and (2) developing surface passivation techniques (prior to deposition of SiO_2/Si_3N_4 insulating layers) to satisfy the dangling bonds on the laser sidewall associated with the leakage current. Additionally, other aspects can be addressed by: (1) improving the heat transport from the laser's active region by using epi-side down mounting; and (2) optical gain of the laser resonator and power emitted from the laser facet can be enhanced by putting high reflective (HR) and anti-reflective (AR) coatings on the laser facets.

Estimating the laser's internal quantum efficiency, which tells about free-carrier absorption loss and is important in designing lasers for longer wavelengths, are not covered in this work. One method of estimating internal quantum efficiency involves studying the effect of different cavity lengths on laser properties [162]. Another important aspect of any laser is to obtain knowledge about the gain spectra which is important from a design perspective. The laser's gain spectra can be measured using the Hakki-Paoli method, [163] which involves the below threshold performance of the laser.

In the study of laser beam optics, far-field pattern is obtained in growth direction by rotating the detector around the laser to ensure the line-of-sight between the laser and the detector. In lateral direction, the detector cannot be moved around the laser because of the limitation of the experimental geometry; instead it is moved in a parallel plane. As a result, the limited field-of-view (FOV) of the detector put some constraints on obtaining the far-field data (though a correction can be applied). Our experimental setup can be improved to overcome this limitation of the FOV of the detector. In this study, only the beam quality factor (M^2) is obtained for the far-field beam profile, other

important parameters such as “brightness” and “spot size” are not characterized. These parameters are important for many applications, especially in fiber optics where high brightness laser along with small spot size is needed for efficient transmission. As well, this work to obtain the beam profile should be extended to elevated temperature to observe any degradation in beam shape and quality. The near-field pattern in this study was obtained only by simulation and partly avoided because of the complexity in setting up the experiment. The near-field pattern, which involves information regarding the quality of the waveguide, should be directly measured in the future.

In the cleaved-coupled-cavity (CCC) laser, the length of the long section (LS) and the short section (SS) laser is chosen as 1mm and 0.5mm, respectively based on the existing geometry of the laser for generating single mode emission. The continuous tuning range is found close to 1nm from this 2:1 length ratio of LS and SS, which is insufficient for most of the applications. Different length ratio (*e.g.*, 3:1 or 4:1) should be investigated to obtain better continuous tuning capability and side mode suppression ratio. Based on the simulation, the width of the air-gap between the LS and the SS should be a multiple of half lasing wavelength for maximum coupling. In this experiment, the width of the milled air-gap is measured as ~10μm which is not exactly a multiple of half wavelength. In future, this width should be made as narrow as possible and a precise multiple of the half wavelength to obtained maximum coupling efficiency. The capability of using an ICL and ICIP as a mini sensor was already demonstrated by monolithically integrating them in a single chip at room temperature [93] where the LS acts as an ICL and SS as an ICIP; however the lasing emission is not a single mode. This work can be further extended by employing three-section geometry where the first

two sections will act as a CCC laser for generating single mode emission and the third section will act as an ICIP for detection. This three-section combination can be used as a battery operated portable lab-on-a-chip mini sensor in mid-IR region for detecting target gases. The FIB recipe for milling III-V materials can be further applied to explore the material defects located deep into the epitaxial layer of MBE grown samples. The sidewall quality of the FIB milled facet can be further improved by employing simultaneous milling technique mentioned in [118]; however this technique has not been applied due to the licensing limitations associated with our Zeiss Neon dual-beam SEM.

Currently, the high frequency operation of ICIPs is limited by the external circuit parameters, especially by the bonding pad capacitance and bonding wire inductance. It is expected that better device packaging and replacing the bonding wires with transmission lines will further improve the device frequency response and leading to FSO applications with heterodyne detection. The measured 3-dB bandwidths of such improved ICIPs can be used to extract the device diffusion length at different temperatures. Studying the change in the frequency response of ICIPs with bias and temperature remains unexplored and is worth investigation. The low-loss transmission demonstrated in our one-meter long FSO link opens up the possibility of establishing longer distance (*e.g.*, building to building) links without the need for a signal booster. In the future, the room temperature operation of ICIPs and their high detectivities will allow this optical communication from mid- to long-wave IR. In this work, the FSO link is only qualitatively investigated in terms of an eye diagram, in the future must be investigated more quantitatively (*e.g.*, by estimating bit error rate).

In the study of carrier transport mechanism, the reverse saturation current density (J_o) is extracted by fitting a modified photovoltaic-cell equation, where the series resistance of the device is neglected. This series resistance, including the resistance from the device, contact resistance and wire resistance, plays a vital role when the device current is high. In the future, to get more accurate data, the series resistance should be included in extracting J_o. The extracted J_o can be further analyzed and a comprehensive model can be developed for extracting other important device parameters (*e.g.*, carrier lifetime). This work is based on devices where the carrier transport takes place in their quantum-well structures and should be extended to include devices where the carrier transport is mainly due to diffusion.

References

[1] H. K. Choi, H. K. Choi, J. Wiley, and Sons, *Long-Wavelength Infrared Semiconductor Lasers*: Wiley, 2004.

[2] *The HITRAN Database*. Available: https://www.cfa.harvard.edu/hitran/

[3] D. S. Bomse, D. C. Hovde, D. B. Oh, J. A. Silver, A. C. Stanton, H. Brittain, *et al.*, "Diode laser spectroscopy for on-line chemical analysis," vol. 1681, pp. 138-148, 1992.

[4] *The Infrared Region of the Electromagnetic Spectrum*. Available: http://www.irradianceglass.com/2016/08/09/irg-educational-series-infrared-the-light-we-cannot-see/

[5] I. Melngailis, "Maser action in InAs diodes," *Applied Physics Letters*, vol. 2, pp. 176-178, 1963.

[6] Y. Horikoshi: Semiconductor lasers with wavelengths > 2μm, in S*emiconductors and Semimetals* 22, W. T. Tsang (Ed.) (Academic Press, London 1985), pp. 93–151.

[7] E. P. O. Reilly and A. R. Adams, "Band-structure engineering in strained semiconductor lasers," *IEEE Journal of Quantum Electronics*, vol. 30, pp. 366-379, 1994.

[8] L. R. Ram-Mohan and J. R. Myer, "Multiband finite element modeling of wavefunction engineered electro-optical devices," *Journal of Nonlinear Optical Physics & Materials*, vol. 04, pp. 191-243, 1995.

[9] G. Bauer, M. Kriechbaum, Z. Shi, and M. Tacke, "IV–VI quantum wells for infrared lasers," *Journal of Nonlinear Optical Physics & Materials*, vol. 04, pp. 283-312, 1995.

[10] Z. Shi, M. Tacke, A. Lambrecht, and H. Böttner, "Midinfrared lead salt multi-quantum-well diode lasers with 282K operation," *Applied Physics Letters*, vol. 66, pp. 2537-2539, 1995.

[11] M. Tacke, "Lead–salt lasers," *Philosophical Transactions of the Royal Society of London. Series A: Mathematical, Physical and Engineering Sciences*, vol. 359, p. 547, 2001.

[12] M. Zandian, J. M. Arias, R. Zucca, R. V. Gil, and S. H. Shin, "HgCdTe double heterostructure injection laser grown by molecular beam epitaxy," *Applied Physics Letters*, vol. 59, pp. 1022-1024, 1991.

[13] J. M. Arias, M. Zandian, R. Zucca, and J. Singh, "HgCdTe infrared diode lasers grown by MBE," *Semiconductor Science and Technology*, vol. 8, p. S255, 1993.

[14] L. Li, H. Ye, Y. Jiang, R. Q. Yang, J. C. Keay, T. D. Mishima, *et al.*, "MBE-grown long-wavelength interband cascade lasers on InAs substrates," *Journal of Crystal Growth*, vol. 425, pp. 369–372, 2015.

[15] I. Vurgaftman, R. Weih, M. Kamp, J. R. Meyer, C. L. Canedy, C. S. Kim, *et al.*, "Interband cascade lasers," *Journal of Physics D: Applied Physics*, vol. 48, p. 123001, 2015.

[16] S. M. S. Rassel, L. Li, Y. Li, R. Q. Yang, J. A. Gupta, X. Wu, *et al.*, "High-temperature and low-threshold interband cascade lasers at wavelengths longer than 6 μm," *Optical Engineering*, vol. 57, p. 1, 2017.

[17] M. Beck, D. Hofstetter, T. Aellen, J. Faist, U. Oesterle, M. Ilegems, *et al.*, *Continuous Wave Operation of a Mid-Infrared Semiconductor Laser at Room Temperature* vol. 295, 2002.
[18] Y. Yao, A. J. Hoffman, and C. F. Gmachl, "Mid-infrared quantum cascade lasers," *Nature Photonics,* vol. 6, p. 432, 2012.
[19] G. Belenky, L. Shterengas, G. Kipshidze, and T. Hosoda, "Type-I Diode Lasers for Spectral Region Above 3 μm," *IEEE Journal of Selected Topics in Quantum Electronics,* vol. 17, pp. 1426-1434, 2011.
[20] L. Shterengas, G. Kipshidze, T. Hosoda, M. Wang, T. Feng, and G. Belenky, "Cascade Type-I Quantum Well GaSb-Based Diode Lasers," *Photonics,* vol. 3, p. 27, 2016.
[21] K. Ohtani, M. Beck, and J. Faist, "Double metal waveguide InGaAs/AlInAs quantum cascade lasers emitting at 24 μm," *Applied Physics Letters,* vol. 105, p. 121115, 2014.
[22] R. Q. Yang, C. J. Hill, K. Mansour, Y. Qiu, A. Soibel, R. E. Muller, *et al.*, "Distributed Feedback Mid-IR Interband Cascade Lasers at Thermoelectric Cooler Temperatures," *IEEE Journal of Selected Topics in Quantum Electronics,* vol. 13, pp. 1074-1078, 2007.
[23] W. W. Bewley, C. L. Canedy, C. S. Kim, M. Kim, J. R. Lindle, J. Abell, *et al.*, "Ridge-width dependence of midinfrared interband cascade laser characteristics," 2010.
[24] I. Vurgaftman, W. W. Bewley, C. L. Canedy, C. S. Kim, M. Kim, C. D. Merritt, *et al.*, "Rebalancing of internally generated carriers for mid-infrared interband cascade lasers with very low power consumption," *Nat Commun,* vol. 2, p. 585, 2011.
[25] R. Q. Yang, "Interband cascade (IC) lasers," Chapter 12 in Semiconductor Lasers: Fundamentals and Applications, A. Baranov and E. Tournie, Eds., Woodhead Publishing Limited, Cambridge, United Kingdom , 2013.
[26] R. Q. Yang, L. Li, Y. Jiang, "Interband cascade lasers: from original concept to practical devices," *Progress in Physics*, vol. 34, pp.169-190, 2014, (in Chinese).
[27] R. Weih, M. Kamp, and S. Höfling, "Interband cascade lasers with room temperature threshold current densities below 100 A/cm^2," *Applied Physics Letters,* vol. 102, p. 231123, 2013.
[28] C. L. Canedy, J. Abell, C. D. Merritt, W. W. Bewley, C. S. Kim, M. Kim, *et al.*, "Pulsed and CW performance of 7-stage interband cascade lasers," *Optics Express,* vol. 22, pp. 7702-7710, 2014.
[29] W. W. Bewley, C. L. Canedy, C. S. Kim, M. Kim, C. D. Merritt, J. Abell, *et al.*, "Continuous-wave interband cascade lasers operating above room temperature at $\lambda = 4.7$-5.6 μm," *Optics Express,* vol. 20, pp. 3235-3240, 2012.
[30] O. Keita and O. Hideo, "An InAs-Based Intersubband Quantum Cascade Laser," *Japanese Journal of Applied Physics*, vol. 41, p. L1279, 2002.
[31] R. Teissier et al., "Room temperature operation of InAs/AlSb quantum cascade lasers," *Applied Physics Letters*, 85, 167–169, 2004.
[32] Y. Zuowei, J. Yuchao, T. Zhaobing, R. Q. Yang, T. D. Mishima, M. B. Santos, *et al.*, "Far-Field Patterns of Plasmon Waveguide Interband Cascade Lasers," *IEEE Journal of Quantum Electronics,* vol. 47, pp. 1414-1419, 2011.

[33] L. B. Allen, H. G. Koenig, and R. R. Rice, "Single Frequency Injection Laser Diodes for Integrated Optics and Fiber Optics Applications," in *22nd Annual Technical Symposium*, 1978, p. 10.
[34] C. Henry and R. Kazarinov, "Stabilization of single frequency operation of coupled-cavity lasers," *IEEE Journal of Quantum Electronics,* vol. 20, pp. 733-744, 1984.
[35] R. J. Lang and A. Yariv, "An exact formulation of coupled-mode theory for coupled-cavity lasers," *IEEE Journal of Quantum Electronics,* vol. 24, pp. 66-72, 1988.
[36] R. Q. Yang, "Infrared laser based on intersubband transitions in quantum wells," *Superlattices Microstruct.,* vol. 17, p. 77, 1995.
[37] L. Chih-Hsiang, R. Q. Yang, D. Zhang, S. J. Murry, S. S. Pei, A. A. Allerman, *et al.*, "Type-II interband quantum cascade laser at 3.8 μm," *Electronics Letters,* vol. 33, pp. 598-599, 1997.
[38] B. H. Yang, D. Zhang, R. Q. Yang, C.-H. Lin, S. J. Murry, and S. S. Pei, "Mid-infrared interband cascade lasers with quantum efficiencies >200%," *Applied Physics Letters,* vol. 72, pp. 2220-2222, 1998.
[39] C. L. Felix, W. W. Bewley, E. H. Aifer, I. Vurgaftman, J. R. Meyer, C. H. Lin, *et al.*, "Low threshold 3 μm interband cascade "W" laser," *Journal of Electronic Materials,* vol. 27, pp. 77-80, 1998.
[40] J. D. Bruno, J. L. Bradshaw, R. Q. Yang, J. T. Pham, and D. E. Wortman, "Low-threshold interband cascade lasers with power efficiency exceeding 9%," *Applied Physics Letters,* vol. 76, pp. 3167-3169, 2000.
[41] L. J. Olafsen, E. H. Aifer, I. Vurgaftman, W. W. Bewley, C. L. Felix, J. R. Meyer, *et al.*, "Near-room-temperature mid-infrared interband cascade laser," *Applied Physics Letters,* vol. 72, pp. 2370-2372, 1998.
[42] R. Q. Yang, J. L. Bradshaw, J. D. Bruno, J. T. Pham, and D. E. Wortman, "Power, efficiency, and thermal characteristics of type-II interband cascade lasers," *IEEE Journal of Quantum Electronics,* vol. 37, pp. 282-289, 2001.
[43] C. R. Webster, P. R. Mahaffy, S. K. Atreya, G. J. Flesch, M. A. Mischna, P.-Y. Meslin, *et al.*, "Mars methane detection and variability at Gale crater," *Science,* vol. 347, pp. 415-417, 2015.
[44] R. Q. Yang et al., "Recent progress in interband cascade devices," in *Abstract Book of The Forth Int. Workshop on Opportunities and Challenges in Mid-Infrared Laser-Based Gas Sensing (MIRSENS 4)*, Wroclaw, Poland, p. 31 (2017).
[45] J. Faist, F. Capasso, D. L. Sivco, C. Sirtori, A. L. Hutchinson, and A. Y. Cho, "Quantum Cascade Laser," *Science,* vol. 264, pp. 553-556, 1994.
[46] Y. Bai, N. Bandyopadhyay, S. Tsao, S. Slivken, and M. Razeghi, "Room temperature quantum cascade lasers with 27% wall plug efficiency," *Applied Physics Letters,* vol. 98, p. 181102, 2011.
[47] M. S. Vitiello, G. Scalari, B. Williams, and P. De Natale, "Quantum cascade lasers: 20 years of challenges," *Optics Express,* vol. 23, pp. 5167-5182, 2015.
[48] D. Chastanet, A. Bousseksou, G. Lollia, M. Bahriz, F. H. Julien, A. N. Baranov, *et al.*, "High temperature, single mode, long infrared ($\lambda = 17.8$ μm) InAs-based quantum cascade lasers," *Applied Physics Letters,* vol. 105, p. 111118, 2014.

[49] A. A. Belyanin, M. T. Kelemen, P. M. Smowton, J. Gilly, M. Haag, J. Biesenbach, *et al.*, "Diode laser arrays for 1.8 to 2.3 μm wavelength range," vol. 7230, p. 72301K, 2009.
[50] D. Donetsky, G. Kipshidze, L. Shterengas, T. Hosoda, and G. Belenky, "2.3 μm type-I quantum well GaInAsSb/AlGaAsSb/GaSb laser diodes with quasi-CW output power of 1.4W," *Electronics Letters*, vol. 43, pp. 810-811, 2007.
[51] J. G. Kim, L. Shterengas, R. U. Martinelli, G. L. Belenky, D. Z. Garbuzov, and W. K. Chan, "Room-temperature 2.5 μm InGaAsSb/AlGaAsSb diode lasers emitting 1 W continuous waves," *Applied Physics Letters*, vol. 81, pp. 3146-3148, 2002.
[52] I. Vurgaftman, J. R. Meyer, and L. R. Ram-Mohan, "Band parameters for III–V compound semiconductors and their alloys," *Journal of Applied Physics*, vol. 89, pp. 5815-5875, 2001.
[53] T. Borca-Tasciuc, et al. "Thermal conductivity of InAs/AlSb superlattices", *Microscale Thermophys. Eng*. 5, 225, 2001.
[54] K. Ohtani, K. Fujita, and H. Ohno, "Mid-infrared InAs⁄AlGaSb superlattice quantum-cascade lasers," *Applied Physics Letters*, vol. 87, p. 211113, 2005.
[55] O. Keita and O. Hideo, "An InAs-Based Intersubband Quantum Cascade Laser," *Japanese Journal of Applied Physics*, vol. 41, p. L1279, 2002.
[56] C. Sirtori, J. Faist, F. Capasso, D. L. Sivco, A. L. Hutchinson, S. N. G. Chu, *et al.*, "Continuous wave operation of midinfrared (7.4–8.6 μm) quantum cascade lasers up to 110 K temperature," *Applied Physics Letters*, vol. 68, pp. 1745-1747, 1996.
[57] R. Teissier, D. Barate, A. Vicet, C. Alibert, A. N. Baranov, X. Marcadet, *et al.*, "Room temperature operation of InAs⁄AlSb quantum cascade lasers," *Applied Physics Letters*, vol. 85, pp. 167-169, 2004.
[58] L. Li, Y. Jiang, H. Ye, R. Q. Yang, T. D. Mishima, M. B. Santos, *et al.*, "Low-threshold InAs-based interband cascade lasers operating at high temperatures," *Applied Physics Letters*, vol. 106, 2015.
[59] C. D. Farmer, C. R. Stanley, C. N. Ironside, and M. Garcia, "Improved GaAs-based quantum cascade laser (∼11 μm) using high-reflectivity metal facet coating," *Electronics Letters*, vol. 38, p. 1443, 2002.
[60] W. W. Chow and S. W. Koch, *Semiconductor-Laser Fundamentals: Physics of the Gain Materials*: Springer Berlin Heidelberg, 2013.
[61] Y. Jiang, "High performance InAs based Interband Cascade Lasers," PhD Dissertation, ECE, University of Oklahoma, 2016.
[62] R. Q. Yang, "Infrared laser based on intersubband transitions in quantum wells," *Superlattices and Microstructures*, vol. 17, pp. 77-83, 1995.
[63] R. Q. Yang and J. M. Xu, "Population inversion through resonant interband tunneling," *Applied Physics Letters*, vol. 59, pp. 181-182, 1991.
[64] R. Q. Yang and J. M. Xu, "On far-infrared inter-subband lasing in quantum wells," in Int. Semiconductor Device Research Symp., Charlottesville, Virginia, pp. 189–192, 1991.
[65] R. Q. Yang and J. M. Xu, "Leaky quantum wells: A basic theory and applications," *Canadian Journal of Physics*, vol. 70, pp. 1153-1158, 1992.

[66] R. Q. Yang, "Phase time delay for interband tunneling in leaky quantum wells," *Physics Letters A,* vol. 186, pp. 339-344, 1994.
[67] R. Q. Yang and J. M. Xu, "Analysis of transmission in polytype interband tunneling heterostructures," *Journal of Applied Physics,* vol. 72, pp. 4714-4726, 1992.
[68] R. Q. Yang, "Type-II Interband Cascade Lasers: From Concept to Devices," *AIP Conference Proceedings,* vol. 772, pp. 1553-1554, 2005.
[69] R. Q. Yang, "20 years of interband cascade lasers and related devices," abstract and talk at 12th International Conference on Mid-Infrared Optoelectronics Materials and Devices, Montpellier, France, October 5-9, 2014.
[70] R. Q. Yang, "Invention of Interband Cascade Lasers – My Journey and Physics," *Physics Letters A,* vol. 45, pp. 46-51, 2016.
[71] J. R. Meyer, I. Vurgaftman, R. Q. Yang, and L. R. Ram-Mohan, "Type-II and type-I interband cascade lasers," *Electronics Letters,* vol. 32, pp. 45-46, 1996.
[72] R. Q. Yang and S. S. Pei, "Novel type-II quantum cascade lasers," *Journal of Applied Physics,* vol. 79, pp. 8197-8203, 1996 1996.
[73] L. Shterengas, G. Kipshidze, T. Hosoda, R. Liang, T. Feng, M. Wang, *et al.*, "Cascade Pumping of 1.9–3.3 μm Type-I Quantum Well GaSb-Based Diode Lasers," *IEEE Journal of Selected Topics in Quantum Electronics,* vol. 23, pp. 1-8, 2017.
[74] Z. Tian, R. Q. Yang, T. D. Mishima, M. B. Santos, R. T. Hinkey, M. E. Curtis, et al., "InAs-based interband cascade lasers near 6 μm," *Electronics Letters*, vol. 45, p. 48, 2009.
[75] R. Q. Yang et al., "Recent progress in development of InAs-based interband cascade lasers," *Proc. SPIE* 8640, 86400Q, 2013.
[76] M. Dallner, F. Hau, S. Höfling, and M. Kamp, "InAs-based interband-cascade-lasers emitting around 7 μm with threshold current densities below 1 kA/cm^2 at room temperature," *Applied Physics Letters*, vol. 106, p. 041108, 2015.
[77] C. L. Canedy, M. V. Warren, C. D. Merritt, W. W. Bewley, C. S. Kim, M. Kim, *et al.*, "Interband cascade lasers with longer wavelengths," in *SPIE OPTO*, 2017, p. 7.
[78] A. Schade and S. Höfling, "Long wavelength interband cascade lasers on GaSb substrates," in *SPIE Optical Engineering + Applications*, p. 6., 2017. .
[79] R. Q. Yang, "InAs-based quantum cascade lasers with enhanced confinement," *Semiconductor Science and Technology,* vol. 30, p. 105023, 2015.
[80] Z. Tian, R. Q. Yang, T. D. Mishima, M. B. Santos, R. T. Hinkey, M. E. Curtis, *et al.*, "InAs-based interband cascade lasers near 6 μm," *Electronics Letters,* vol. 45, p. 48, 2009.
[81] R. Q. Yang and J. M. Xu, "Bound and quasibound states in leaky quantum wells," *Physical Review B (Condensed Matter)* 46 (11), 6969–6974, 1992.
[82] Z. Tian, Y. Jiang, L. Li, R. T. Hinkey, Z. Yin, R. Q. Yang, *et al.*, "InAs-Based Mid-Infrared Interband Cascade Lasers Near 5.3μm," *IEEE Journal of Quantum Electronics,* vol. 48, pp. 915-921, 2012.
[83] R. T. Hinkey, Z. Tian, R. Q. Yang, T. D. Mishima, and M. B. Santos, "Reflectance spectrum of plasmon waveguide interband cascade lasers and

observation of the Berreman effect," *Journal of Applied Physics*, vol. 110, p. 043113, 2011.
[84] J. R. Meyer, Unpublished data of Naval Research Laboratory, private communications, 2017.
[85] A. E. Siegman, *Lasers*: University Science Books, 1986.
[86] H. Sun, *A Practical Guide to Handling Laser Diode Beams*: Springer Netherlands, 2015.
[87] W. contributors. (2017). *Beam parameter product* [Online]. Available: https://en.wikipedia.org/w/index.php?title=Beam_parameter_product&oldid=793282516
[88] D. Meschede, *Optics, Light and Lasers: The Practical Approach to Modern Aspects of Photonics and Laser Physics*: Wiley, 2007.
[89] R. Hunsperger, *Integrated Optics*, 6 ed.: Springer-Verlag New York, 2009.
[90] E. Kapon, *Semiconductor Lasers II: Materials and Structures*: Academic Press, 1999.
[91] J. E. Carroll, J. Whiteaway, and D. Plumb, *Distributed Feedback Semiconductor Lasers*: Institution of Electrical Engineers, 1998.
[92] T. Takeuchi, T. Detchprohm, M. Iwaya, N. Hayashi, K. Isomura, K. Kimura, *et al.*, "Improvement of far-field pattern in nitride laser diodes," *Applied Physics Letters*, vol. 75, pp. 2960-2962, 1999.
[93] H. Lotfi, L. Li, S. Rassel, R. Q. Yang, C. J. Corrége, M. Johnson, *et al.*, "Monolithically integrated mid-IR interband cascade laser and photodetector operating at room temperature," *Applied Physics Letters*, vol. 109, p. 151111, 2016.
[94] S. Hofling, J. P. Reithmaier, and A. Forchel, "Device performance and wavelength tuning behavior of ultra-short quantum-cascade microlasers with deeply etched Bragg-mirrors," *IEEE Journal of Selected Topics in Quantum Electronics*, vol. 11, pp. 1048-1054, 2005.
[95] P. Fuchs, J. Friedl, S. Höfling, J. Koeth, A. Forchel, L. Worschech, *et al.*, "Single mode quantum cascade lasers with shallow-etched distributed Bragg reflector," *Optics Express*, vol. 20, pp. 3890-3897, 2012.
[96] H. Andreas, M. Richard, and F. Jérôme, "External cavity quantum cascade laser," *Semiconductor Science and Technology*, vol. 25, p. 083001, 2010.
[97] G. Xu, V. Moreau, Y. Chassagneux, A. Bousseksou, R. Colombelli, G. Patriarche, *et al.*, "Surface-emitting quantum cascade lasers with metallic photonic-crystal resonators," *Applied Physics Letters*, vol. 94, p. 221101, 2009.
[98] M. Bo and W. Qi Jie, "Broadly tunable single-mode mid-infrared quantum cascade lasers," *Journal of Optics*, vol. 17, p. 023001, 2015.
[99] Y. Jiang, L. Li, H. Ye, R. Q. Yang, T. D. Mishima, M. B. Santos, *et al.*, "InAs-Based Single-Mode Distributed Feedback Interband Cascade Lasers," *IEEE Journal of Quantum Electronics*, vol. 51, pp. 1-7, 2015.
[100] L. Coldren and T. Koch, "Analysis and design of coupled-cavity lasers - Part I: Threshold gain analysis and design guidelines," *IEEE Journal of Quantum Electronics*, vol. 20, pp. 659-670, 1984.

[101] L. B. Allen, H. G. Koenig, and R. R. Rice, "Single Frequency Injection Laser Diodes for Integrated Optics and Fiber Optics Applications," in *22nd Annual Technical Symposium*, 1978, p. 10.
[102] K. J. Ebeling and L. A. Coldren, "Analysis of multielement semiconductor lasers," *Journal of Applied Physics*, vol. 54, pp. 2962-2969, 1983.
[103] J. Berger and D. Fekete, "Narrow single stabilized mode operation of coupled-stripe diode lasers," *Applied Physics Letters*, vol. 47, pp. 1029-1031, 1985.
[104] J. Jin, L. Wang, T. Yu, Y. Wang, and J.-J. He, "Widely wavelength switchable V-coupled-cavity semiconductor laser with ~40 dB side-mode suppression ratio," *Optics Letters*, vol. 36, pp. 4230-4232, 2011.
[105] W.-H. Guo, Q. Lu, M. Nawrocka, A. Abdullaev, J. O'Callaghan, and J. F. Donegan, "Nine-channel wavelength tunable single mode laser array based on slots," *Optics Express*, vol. 21, pp. 10215-10221, 2013.
[106] P. Fuchs, J. Seufert, J. Koeth, J. Semmel, S. Höfling, L. Worschech, *et al.*, "Widely tunable quantum cascade lasers with coupled cavities for gas detection," *Applied Physics Letters*, vol. 97, p. 181111, 2010.
[107] S. Höfling, J. Heinrich, J. P. Reithmaier, A. Forchel, J. Seufert, M. Fischer, *et al.*, "Widely tunable single-mode quantum cascade lasers with two monolithically coupled Fabry-Pérot cavities," *Applied Physics Letters*, vol. 89, p. 241126, 2006.
[108] J. Bengtsson, J. Gustavsson, Å. s. Haglund, A. Larsson, A. Bachmann, K. Kashani-Shirazi, *et al.*, "Diffraction loss in long-wavelength buried tunnel junction VCSELs analyzed with a hybrid coupled-cavity transfer-matrix model," *Optics Express*, vol. 16, pp. 20789-20802, 2008.
[109] B. Julia, H. Thomas, M. Matthias, S. Benedikt, R. Jakob, W. H. Theodor, *et al.*, "Transverse-mode coupling and diffraction loss in tunable Fabry–Pérot microcavities," *New Journal of Physics*, vol. 17, p. 053051, 2015.
[110] Y. Jiang, L. Li, R. Q. Yang, J. A. Gupta, G. C. Aers, E. Dupont, *et al.*, "Type-I interband cascade lasers near 3.2 μm," *Applied Physics Letters*, vol. 106, p. 041117, 2015.
[111] (2017, 03/23/2018). *Focused ion beam*. Available: https://en.wikipedia.org/wiki/Focused_ion_beam
[112] F. Incorporated. (2018). *Introduction: Focused Ion Beam Systems*. Available: http://www.fibics.com/fib/tutorials/introduction-focused-ion-beam-systems/4/
[113] F. K. Khan and D. T. Cassidy, "Widely tunable coupled-cavity semiconductor laser," *Applied Optics*, vol. 48, p. 3809, 2009.
[114] J. Puretz, R. K. DeFreez, R. A. Elliott, and J. Orloff, "Focused-ion-beam micromachined AlGaAs semiconductor laser mirrors," *Electronics Letters*, vol. 22, pp. 700-702, 1986.
[115] L. Hvozdara, A. Lugstein, S. Gianordoli, W. Schrenk, G. Strasser, K. Unterrainer, *et al.*, "Self-aligned coupled cavity GaAs/AlGaAs midinfrared quantum-cascade laser," *Applied Physics Letters*, vol. 77, pp. 1077-1079, 2000.
[116] K. Pierściński, D. Pierścińska, M. Pluska, P. Gutowski, I. Sankowska, P. Karbownik, *et al.*, "Room temperature, single mode emission from two-section coupled cavity InGaAs/AlGaAs/GaAs quantum cascade laser," *Journal of Applied Physics*, vol. 118, p. 133103, 2015.

[117] I. M. Ross, W. H. Ng, L. R. Wilson, I. J. Luxmoore, J. W. Cockburn, A. Krysa, *et al.*, "Fabrication of novel quantum cascade lasers using focused ion beam (FIB) processing," *Journal of Physics: Conference Series*, vol. 26, pp. 215-218, 2006.
[118] A. Czerwinski, M. Pluska, A. Łaszcz, J. Ratajczak, K. Pierściński, D. Pierścińska, *et al.*, "Formation of coupled-cavities in quantum cascade lasers using focused ion beam milling," *Microelectronics Reliability*, vol. 55, pp. 2142-2146, 2015.
[119] L. R. Harriott, "Micromachining of optical structures with focused ion beams," *Journal of Vacuum Science & Technology B: Microelectronics and Nanometer Structures*, vol. 5, p. 207, 1987.
[120] H. Li, J. M. Manceau, A. Andronico, V. Jagtap, C. Sirtori, L. H. Li, *et al.*, "Coupled-cavity terahertz quantum cascade lasers for single mode operation," *Applied Physics Letters*, vol. 104, p. 241102, 2014.
[121] M. Polyanskiy. *Refractive index database*. Available: https://refractiveindex.info/?shelf=main&book=GaSb&page=Adachi
[122] L. A. Coldren, S. W. Corzine, and M. L. Mashanovitch, *Diode Lasers and Photonic Integrated Circuits*: Wiley, 2012.
[123] S. Adachi, *Properties of Group-IV, III-V and II-VI Semiconductors*: Wiley, 2005.
[124] A. Soibel, M. W. Wright, W. Farr, S. Keo, C. Hill, R. Q. Yang, *et al.*, "High-speed operation of interband cascade lasers," *Electronics Letters*, vol. 45, p. 264, 2009.
[125] L. Lei, L. Li, H. Lotfi, H. Ye, R. Q. Yang, T. D. Mishima, *et al.*, "Midwavelength interband cascade infrared photodetectors with superlattice absorbers and gain," *Optical Engineering*, vol. 57, p. 1, 2017.
[126] D. Hofstetter, M. Graf, T. Aellen, J. Faist, L. Hvozdara, and S. Blaser, "23GHz operation of a room temperature photovoltaic quantum cascade detector at 5.35μm," *Applied Physics Letters*, vol. 89, p. 061119, 2006.
[127] G. Ghione, *Semiconductor Devices for High-Speed Optoelectronics*. Cambridge: Cambridge University Press, 2009, p.199.
[128] S. L. March, "Simple equations characterize bond wires," *Microwave & RF*, pp. 105-110, Nov. 1991.
[129] H. Lotfi, L. Li, L. Lei, H. Ye, S. M. Shazzad Rassel, Y. Jiang, *et al.*, "High-frequency operation of a mid-infrared interband cascade system at room temperature," *Applied Physics Letters*, vol. 108, p. 201101, 2016.
[130] A. Soibel, M. W. Wright, W. H. Farr, S. A. Keo, C. J. Hill, R. Q. Yang, *et al.*, "Midinfrared Interband Cascade Laser for Free Space Optical Communication," *IEEE Photonics Technology Letters*, vol. 22, pp. 121-123, 2010.
[131] A. Vardi, N. Kheirodin, L. Nevou, H. Machhadani, L. Vivien, P. Crozat, *et al.*, "High-speed operation of GaN/AlGaN quantum cascade detectors at λ≈1.55μm," *Applied Physics Letters*, vol. 93, p. 193509, 2008.
[132] Y. Zhou, S. Zhai, F. Wang, J. Liu, F. Liu, S. Liu, *et al.*, "High-speed, room-temperature quantum cascade detectors at 4.3 μm," *AIP Advances*, vol. 6, p. 035305, 2016.

[133] I. Kimukin, N. Biyikli, T. Kartaloglu, O. Aytur, and E. Ozbay, "High-Speed InSb Photodetectors on GaAs for Mid-IR Applications," *IEEE Journal of Selected Topics in Quantum Electronics*, vol. 10, pp. 766-770, 2004.
[134] M. Strojnik, P. D. Grant, H. C. Liu, M. Buchanan, and R. Dudek, "Ultrahigh frequency quantum well infrared photodetectors," vol. 6297, p. 629708, 2006.
[135] C. Koeniguer, G. Dubois, A. Gomez, and V. Berger, "Electronic transport in quantum cascade structures at equilibrium," *Physical Review B*, vol. 74, 2006.
[136] A. Buffaz, A. Gomez, M. Carras, L. Doyennette, and V. Berger, "Role of subband occupancy on electronic transport in quantum cascade detectors," *Physical Review B*, vol. 81, 2010.
[137] R. T. Hinkey and R. Q. Yang, "Theory of multiple-stage interband photovoltaic devices and ultimate performance limit comparison of multiple-stage and single-stage interband infrared detectors," *Journal of Applied Physics*, vol. 114, p. 104506, 2013.
[138] H. S. Rauschenbach, *Solar Cell Array Design Handbook: The Principles and Technology of Photovoltaic Energy Conversion*: Springer Netherlands, 2012.
[139] W. Huang, L. Li, J. A. Massengale, R. Q. Yang, T. D. Mishima, and M. B. Santos, "Minority carrier lifetime in mid-wavelength interband cascade infrared photodetectors," unpublished.
[140] L. Lei, L. Li, W. Huang, J. A. Massengale, H. Ye, H. Lotfi, *et al.*, "Resonant tunneling and multiple negative differential conductance features in long wavelength interband cascade infrared photodetectors," *Applied Physics Letters*, vol. 111, p. 113504, 2017.
[141] S. Kalchmair, "I-V data from QCL structure at room termperature," Perssonal communation through Email ed, Jul 2017.
[142] H. K. Chung, M. A. Rosenberg, and P. H. Zimmermann, "Origin of 1/f noise observed in Hg0.7Cd0.3Te variable area photodiode arrays," *Journal of Vacuum Science & Technology A: Vacuum, Surfaces, and Films*, vol. 3, pp. 189-191, 1985.
[143] B. Yves, "IV data from qunatum cascade laser," Personal communication through Email ed, Jul 2017.
[144] R. K. Garg, A. Dixit, and P. Yadav, *Basic Electronics*: Laxmi Publications Pvt Limited, 2008.
[145] A. Rogalski, *Infrared Detectors*: Taylor & Francis, 2000.
[146] T. Dougakiuchi, K. Fujita, T. Hirohata, A. Ito, M. Hitaka, and T. Edamura, "High photoresponse in room temperature quantum cascade detector based on coupled quantum well design," *Applied Physics Letters*, vol. 109, p. 261107, 2016.
[147] J. Nelson, *The Physics of Solar Cells*: Imperial College Press, 2003.
[148] R. T. Hinkey, Z. Tian, S. M. S. S. Rassel, R. Q. Yang, J. F. Klem, and M. B. Johnson, "Interband Cascade Photovoltaic Devices for Conversion of Mid-IR Radiation," *IEEE Journal of Photovoltaics*, vol. 3, pp. 745-752, 2013.
[149] X. Wang, J. Liu, S. Zhai, F. Liu, and Z. Wang, "Room temperature quantum cascade detector operating at 4.3 μm," *Journal of Semiconductors*, vol. 35, p. 104009, 2014.

[150] P. Reininger, T. Zederbauer, B. Schwarz, H. Detz, D. MacFarland, A. M. Andrews, *et al.*, "InAs/AlAsSb based quantum cascade detector," *Applied Physics Letters*, vol. 107, p. 081107, 2015.
[151] L. Li, X. H. Zhou, T. Lin, N. Li, Z. Q. Zhu, and F. Q. Liu, "Electronic transport in a long wavelength infrared quantum cascade detector under dark condition," *Infrared Physics & Technology*, vol. 78, pp. 72-76, 2016.
[152] A. Delga, L. Doyennette, V. Berger, M. Carras, V. Trinité, and A. Nedelcu, "Performances of quantum cascade detectors," *Infrared Physics & Technology*, vol. 59, pp. 100-107, 2013.
[153] F. R. Giorgetta, E. Baumann, M. Graf, Q. Yang, C. Manz, K. Kohler, *et al.*, "Quantum Cascade Detectors," *IEEE Journal of Quantum Electronics*, vol. 45, pp. 1039-1052, 2009.
[154] M. B. Johnson, M. B. Santos, T. D. Mishima, R. Q. Yang, H. Ye, H. Lotfi, *et al.*, "Midwavelength interband cascade infrared photodetectors with superlattice absorbers and gain," *Optical Engineering*, vol. 57, p. 1, 2017.
[155] H. Lotfi, L. Li, L. Lei, R. Q. Yang, J. F. Klem, and M. B. Johnson, "Narrow-Bandgap Interband Cascade Thermophotovoltaic Cells," *IEEE Journal of Photovoltaics*, vol. 7, pp. 1462-1468, 2017.
[156] W. Huang, L. Li, L. Lei, J. A. Massengale, R. Q. Yang, T. D. Mishima, *et al.*, "Electrical gain in interband cascade infrared photodetectors," *Journal of Applied Physics*, vol. 123, p. 113104, 2018.
[157] Z. Tian, R. T. Hinkey, R. Q. Yang, D. Lubyshev, Y. Qiu, J. M. Fastenau, *et al.*, "Interband cascade infrared photodetectors with enhanced electron barriers and p-type superlattice absorbers," *Journal of Applied Physics*, vol. 111, p. 024510, 2012.
[158] N. Gautam, S. Myers, A. V. Barve, B. Klein, E. P. Smith, D. R. Rhiger, *et al.*, "High operating temperature interband cascade midwave infrared detector based on type-II InAs/GaSb strained layer superlattice," *Applied Physics Letters*, vol. 101, p. 021106, 2012.
[159] H. Lotfi, L. Lei, L. Li, R. Q. Yang, J. C. Keay, M. B. Johnson, *et al.*, "High-temperature operation of interband cascade infrared photodetectors with cutoff wavelengths near 8 μm," 2015, p. 9.
[160] H. Lotfi, L. Li, L. Lei, Y. Jiang, R. Q. Yang, J. F. Klem, *et al.*, "Short-wavelength interband cascade infrared photodetectors operating above room temperature," *Journal of Applied Physics*, vol. 119, p. 023105, 2016.
[161] W. Pusz, A. Kowalewski, P. Martyniuk, W. Gawron, E. Plis, S. Krishna, *et al.*, "Mid-wavelength infrared type-II InAs/GaSb superlattice interband cascade photodetectors," 2014, p. 9.
[162] J. Piprek, P. Abraham, and J. E. Bowers, "Cavity length effects on internal loss and quantum efficiency of multiquantum-well lasers," *IEEE Journal of Selected Topics in Quantum Electronics*, vol. 5, pp. 643-647, 1999.
[163] A. Soibel, K. Mansour, Y. Qiu, C. J. Hill, and R. Q. Yang, "Optical gain, loss, and transparency current in high performance mid-infrared interband cascade lasers," *Journal of Applied Physics*, vol. 101, p. 093104, 2007.